Intraseasonal Precipitation Variability Over Tropical Africa

by
Fisseha Berhane

A dissertation submitted to Johns Hopkins University in conformity with the requirements for the degree of Doctor of Philosophy

Baltimore, Maryland
February, 2016

ABSTRACT

Intraseasonal spatiotemporal precipitation variability over tropical Africa has significant impacts on rainfed agriculture, human health, and food and water security, affecting the lives of tens of millions of people. However, there is a paucity of studies that focus on precipitation variability over the region on this time-scale, which is essential for more accurate forecasts and precipitation projections in a changing climate. The dissertation research tries to contribute to a better understanding of the dynamics of sub-seasonal precipitation variability over selected regions of tropical Africa. The work includes: (1) analysis of the drivers and mechanisms associated with summer (June-September) precipitation variability in the Blue Nile river basin, (2) assessment of intra-seasonal influences of the Madden-Julian Oscillation (MJO) on the East African long (March-May) and short (October-December) rains, and (3) examination of sub-seasonal impacts of the MJO on Equatorial West Africa's springtime (March-June) precipitation.

In the Blue Nile river basin, Atlantic Ocean influences dominate precipitation variability in the basin in the early rainy season. In the late rainy season, however, connections with the tropical Pacific Ocean and Indian Monsoon region are more prominent. The mid rainy season experiences influences from both the east and the west. Incorporating the intra-seasonal variability of drivers and mechanisms of precipitation variability in the basin is vital for accurate seasonal and sub-seasonal forecasts and for climate projections under a changing climate since the various drivers and mechanisms may respond differently to climate change.

The Madden-Julian Oscillation (MJO) influences precipitation over East Africa through a combination of various mechanisms. Further, the impacts of the MJO on precipitation in East

Africa shows intra-seasonal and intra-regional variability. Moreover, the MJO shows significant correlations, at reasonable lead times, with precipitation over the region. These results have implications for understanding mechanisms of precipitation variability, and for weather and short-term climate forecasting tools development.

Equatorial West African spring rainy season rainfall is modulated significantly by the MJO. The MJO influences rainfall over the region though the direct propagation of the MJO to the region and though equatorial waves triggered by the MJO in the Indo-Pacific region. About three weeks after the start of the suppressed phase of the MJO in the Indian Ocean, the MJO results in enhanced convection and precipitation over Equatorial West Africa. This association between the MJO and precipitation over Equatorial West Africa can be used to improve the accuracy of forecasts over the region.

DEDICATION

I would like to dedicate this dissertation to my beloved wife Fre Abreha, my sons John, Jacob and Philip and my daughter Bethel.

ACKNOWLEDGEMENTS

I am deeply indebted to my primary advisor, Professor Benjamin Zaitchik who allowed me to pursue my own research interests and who guided me in the right direction. Most of all, his support, patience, encouragement and approachable personality made my PhD study enjoyable and fruitful. Not only did I learn science from him, but also humility, respecting others, hard work and patience. My sincere thanks go to my Ph.D. Committee Members Professors Anand Gnanadesikan and Darryn Waugh for their support and encouragement.

I would also like to extend my gratitude to other faculty members and staffs in the Department of Earth and Planetary Sciences for all their help and motivation. I am grateful to all of my fellow labmates, especially Amin, Hamada, Saleh and Jose. I learned much from our discussions with them.

Most importantly, I am sincerely and greatly indebted to my beloved wife, Fre Abreha. This work was difficult, if not impossible, without her endless love, support, motivation and warmth. I have never felt more supported, cared about, loved and cherished than what my wife has shown me.

Last but not least, I thank Almighty God for His limitless blessings, love and care.

CONTENTS

LIST OF TABLES

LIST OF FIGURES

Chapter 1: Introduction

The livelihood and socioeconomic condition of millions of people in tropical Africa is strongly linked to the spatiotemporal variability of precipitation in the region (e.g., Sultan and Janicot 2003; Segele and Lamb 2005; Sultan et al. 2005). It has been witnessed that a single extreme event over the region can reverse national economic growth made over a period of several years (Gitau 2011). Crop yield over the region is highly affected by the frequency and intensity of dry/wet spells. The region experiences remarkable intraseasonal precipitation variability (e.g., Janicot and Sultan 2001; Matthews 2004; Segele and Lamb 2005), which has significant impacts on agriculture (Verdin et al. 2005), natural-resources (Conway et al. 2005) and public health (Epstein 1999).

Therefore, understanding the dynamics of sub-seasonal precipitation variability over tropical Africa, which is caused by a diverse array of forcings (Nicholson and Kim 1997b; Herrmann and Mohr 2011), is essential for improved subseasonal and seasonal precipitation forecasts to develop agricultural production and to cope with the impacts of extreme departures from normal rainfall such as large-scale droughts and floods, which cause devastating human and economic loss (Conway et al. 2005; Hastenrath et al. 2007). Moreover, investigation of mechanisms of sub-seasonal variability might help to explain why Global Climate Models (GCMs) project increased rainfall patterns over the region, particularly East African March-May rains, while observations show the opposite (Williams and Funk 2011).

However, there are only a limited number of studies that focus on intraseasonal precipitation variability over tropical Africa, due in part to data limitations and in part to the challenges of

characterizing complex precipitation seasonality. Detailed study of sub-seasonal rainfall variability can help to advance our understanding on the dynamics of intraseasonal precipitation over the region, providing an opportunity to analyze the evolution of teleconnection patterns and mechanisms through the course of the rainy seasons, and to understand the contribution of the interaction of forcings on intraseasonal precipitation variability.

1.1. Tropical Africa

Tropical Africa has complex rainfall seasonality. While the main rainy season in the Ethiopian portion of the Blue Nile River basin (1 in Figure 1.1) is from June to September. Equatorial East Africa (2 in Figure 1.1) has bimodal rainfall seasonality: the long rains, which take place from March-May, and the short rains, which occur from October-December. As these seasons are transitions between the summer and winter monsoon, they exhibit complex characteristics and evolve as the intertropical convergence zone moves northwards and southwards over the region. Even if Equatorial West Africa (3 in Figure 1.1) gets remarkable rainfall in the spring rainy season, the drivers and mechanism of rainfall variability in the region are different from those that influence Equatorial East Africa. Regions 1, 2 and 3 in Figure 1.1 exhibit strong intraseasonal variability in precipitation. This variability has significant impacts on rain-fed agriculture, food and water security, and human health affecting the lives of millions of people.

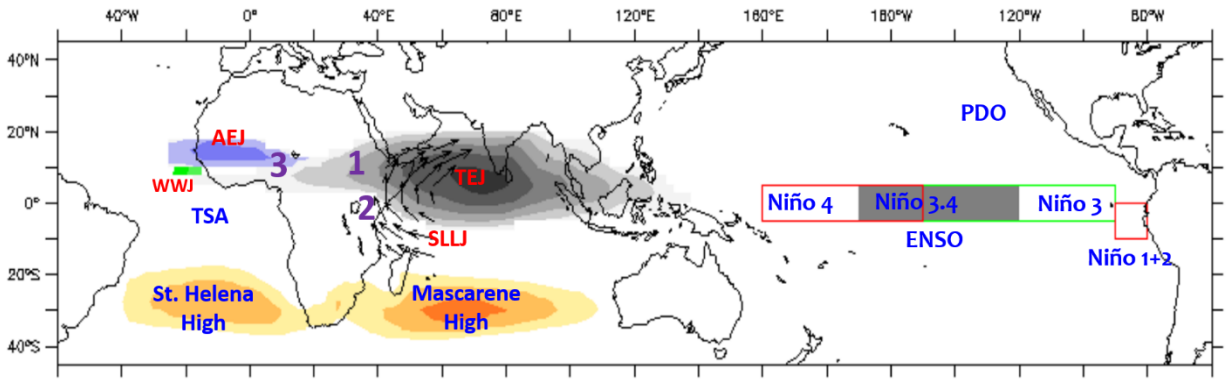

Figure 1.1. Study regions, (1) Blue Nile River basin [34^0 to 40^0 E and 8^0 to 13^0 N] (2) East Africa [30^0 to 42^0 E and 12^0S to 8^0 N] (3) West Africa [17^0W to 25^0 E and 10^0S to 13^0 N], and the main mechanisms and drivers of precipitation variability: Pacific Decadal Oscillation (PDO), Tropical Easterly Jet (TEJ, 200-150 hPa), African Easterly Jet (AEJ, 600-700 hPa), West African Westerly Jet (WWJ, 925 hPa), Somali Low Level Jet (SLLJ, 850 hPa) and St. Helena and Mascarene High pressure systems. The sea surface temperature (SST) regions used to calculate ENSO index and the Tropical Southern Atlantic (TSA) index are also shown.

The Blue Nile River basin is influenced by multiple systems including El Niño–Southern Oscillation (ENSO), Indian Summer Monsoon, Pacific Decadal Oscillation (PDO), St. Helena High and Mascarene High pressure systems and a couple of wind maxima systems such as the Tropical Easterly Jet (TEJ), African Easterly Jet (AEJ), Somali Low Level Jet (SLLJ) and West African Westerly Jet (WAWJ). In Figure 1.1, Niño4, Niño3.4, Niño3 and Niño1+2 are ENSO indicators based on sea surface temperature of the rectangular areas shown.

Equatorial East Africa experiences pronounced regional variations and a complicated seasonal cycle (Cook and Vizy 2013). Meteorologically speaking, it is one of the most complex regions of

the African continent (Spinage 2012; Cook and Vizy 2013), and it experiences profound negative social impacts from seasonal shifts in precipitation patterns and extreme rainfall events (Anyah and Qiu 2012). The region has dramatic topographic contrasts including large lakes, the Rift Valley and snow-capped mountains (Gitau 2011) that result in complex climatic patterns (Spinage 2012) which change rapidly over short distances (Nicholson 1996).

The large scale modes of climate variability that affect rainfall over Equatorial East Africa include the El Niño/Southern Oscillation (ENSO) (Nicholson and Kim 1997a; Mutai and Ward 2000), Indian Ocean Dipole (IOD), mainly in the short rains, (Black 2005a; Owiti 2005; Owiti et al. 2008, among many others), Quasi- Biennial Oscillation (QBO) (Indeje and Semazzi 2000) in the long rains, Madden-Julian Oscillation (Pohl and Camberlin 2006c; Pohl and Camberlin 2006b), in both the short and long rains, and sea surface temperature (SST) variations in the Indian and Pacific Oceans (e.g., Funk et al. 2008; Hastenrath 2007; Ummenhofer et al. 2009).

The spring rains in West Africa are also influenced by SST anomalies in the Pacific and Indian Oceans (Mohino et al. 2011). Further, various systems in the Atlantic Ocean, including SST anomalies in the Gulf of Guinea and St. Helena High, a high pressure system in the Southern Atlantic Ocean, have significant impacts on rainfall over the region. Moreover, the position and strength of the African Easterly Jet, which is caused by the temperature difference between the Sahara and the Gulf of Guinea, MJO and the African easterly waves impact spring season rainfall over West Africa in various ways.

1.2. Dissertation Outline

The first chapter serves as an introduction to why study of sub-seasonal rainfall variability over tropical Africa matters and to the various drivers and mechanisms that influence rainfall over the Blue Nile river basin, East Africa and West Africa. The second (Berhane et al. 2013), third (Berhane and Zaitchik 2014) and fourth (Berhane et al. 2015) chapters represent published papers. Chapter 2 presents the associations of monthly precipitation in the Blue Nile with large-scale patterns of SST, sea level pressure (SLP), and winds, and with a range of climate indices that have been examined at seasonal scale in previous studies. The remaining chapters focus on the Madden-Julian's influence on East Africa and West Africa. The MJO, which is the major mode of weather variability in the tropics, is a naturally occurring component of the coupled ocean-atmosphere system that propagates eastwards (Figure 1.2) in the global tropics (Madden and Julian 1971b, 1972a). As it propagates eastwards, it influences different oceanic and atmospheric variables including winds at different levels, sea level pressure, sea surface temperature, rainfall and velocity potential (Madden and Julian 1971b, 1972a). Chapters 3 and 4 investigate the dynamics and thermodynamics though which MJO influences rainfall variability over East Africa and West Africa, respectively. Chapter 5 presents diagnostic analyses that build on the East Africa MJO analysis presented in Chapter 3. Specifically, interactions between the MJO and ENSO are explored in order to identify mechanisms through which these processes interact to influence precipitation variability in the East African short rains. Finally, the sixth chapter presents general conclusions from the dissertation work.

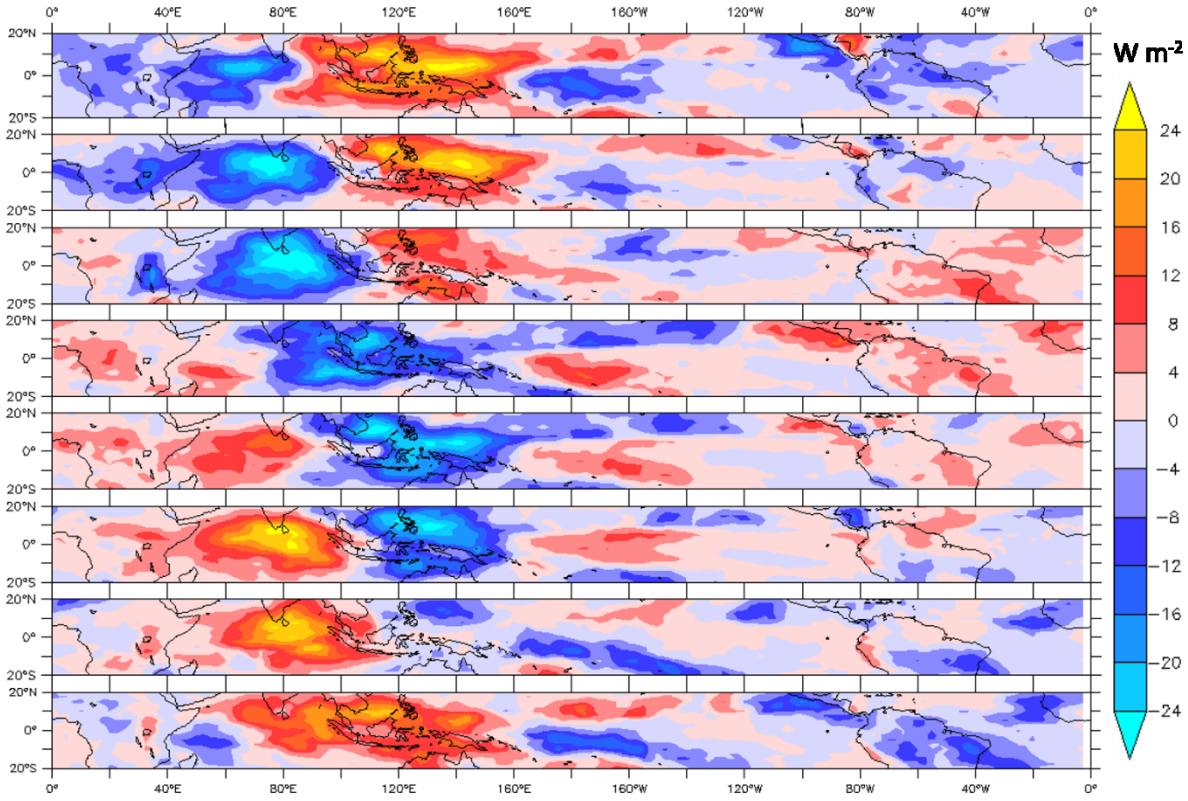

Figure 1. 1. Composites of outgoing longwave radiation (OLR) depicting the eastward propagation of the MJO. Time is downwards at roughly 6 day intervals.

2. Chapter 2: Sub-seasonal analysis of precipitation variability in the Blue Nile River basin[1]

Abstract

The Ethiopian portion of the Blue Nile River basin is subject to significant interannual variability in precipitation. As this variability has implications for local food security and transboundary water resources, numerous studies have been directed at improved understanding and, potentially, predictability of Blue Nile rainy season (June-September) precipitation. Taken collectively, these studies present a wide range of large scale drivers associated with precipitation variability in the Blue Nile: the El Niño-Southern Oscillation (ENSO), the Indian summer monsoon, sea level pressure (SLP) anomalies over the Arabian Peninsula and the Gulf of Guinea, the Quasi-Biennial Oscillation (QBO), and dynamics of the Tropical Easterly Jet (TEJ) and African Easterly Jet (AEJ) have all been emphasized to varying degrees. This study aims to reconcile these diverse analyses by evaluating teleconnection patterns and potential mechanisms of association on sub-seasonal scale. It is found that associations with the TEJ, Pacific modes of variability, and the Indian monsoon are strongest in the late rainy season. Mid-rainy season precipitation (July and August) shows mixed associations with Pacific/Indian Ocean variability and Atlantic Ocean indices, along with connections to regional pressure patterns and the AEJ. June precipitation is negatively correlated with SLP over the Equatorial Atlantic and upper tropospheric geopotential height. June and July precipitation show little significant correlation with the sea surface temperature over the

[1] Berhane, F., B. Zaitchik, and A. Dezfuli, 2013: Sub-seasonal analysis of precipitation variability in the Blue Nile River basin. *Journal of climate*, **27,** 325-344.

Equatorial Pacific Ocean. The observed intraseasonal evolution of teleconnections across the rainy season indicates that sub-seasonal analysis is required to advance understanding and prediction of Blue Nile precipitation variability.

2.1 Introduction

The Blue Nile River is critical to the energy, water, and food security aspirations of Ethiopia, Sudan, and Egypt. In the Ethiopian portion of the Blue Nile basin, a largely subsistence agriculture population depends on seasonal rains for crops and pastures, while at a national level the river is viewed as an opportunity for large-scale hydropower development. In Sudan, waters of the Blue Nile drive hydroelectric power generation and feed major irrigation schemes. In Egypt, water from the Blue Nile accounts for approximately 60% of the annual average 84 Gm^3 of the Nile River at Aswan High Dam (Mohamed et al. 2005).

Flows in the Blue Nile, however, are far from consistent. The river is fed almost exclusively by precipitation in the Ethiopian Highlands (Conway 1997, Conway 2000; Beyene et al. 2010), which is concentrated in a four month rainy season (June – September) (Conway 2000; Beyene et al. 2010) and is subject to significant intraseasonal, interannual and interdecadal variability (e.g., Conway and Hulme 1993; Camberlin 1995; Seleshi and Demaree 1995; Conway 1997, Conway 2000; Segele and Lamb 2005; Abtew et al. 2009; Jury 2010; among many others). Improved understanding of the drivers of precipitation variability is required in order to enhance sub-seasonal and seasonal precipitation forecasts under current climate conditions and to provide a sound basis for projecting potential shifts in precipitation under climate change.

2.1.a. Precipitation in the Blue Nile Headwaters

The proximal driver of rainfall in the headwaters of the Blue Nile is the northward and southward movement of the Intertropical Convergence Zone (ITCZ). The ITCZ's migration to the north in summer months brings convective activity to the basin, with moist air masses from the south and the west (Conway 2000), and potentially the north and the east as well (Viste and Sorteberg 2011) fueling rainfall events (Figure 2.1). In this paper, we use the term ITCZ to refer to the zone where the trade winds from both hemispheres converge.

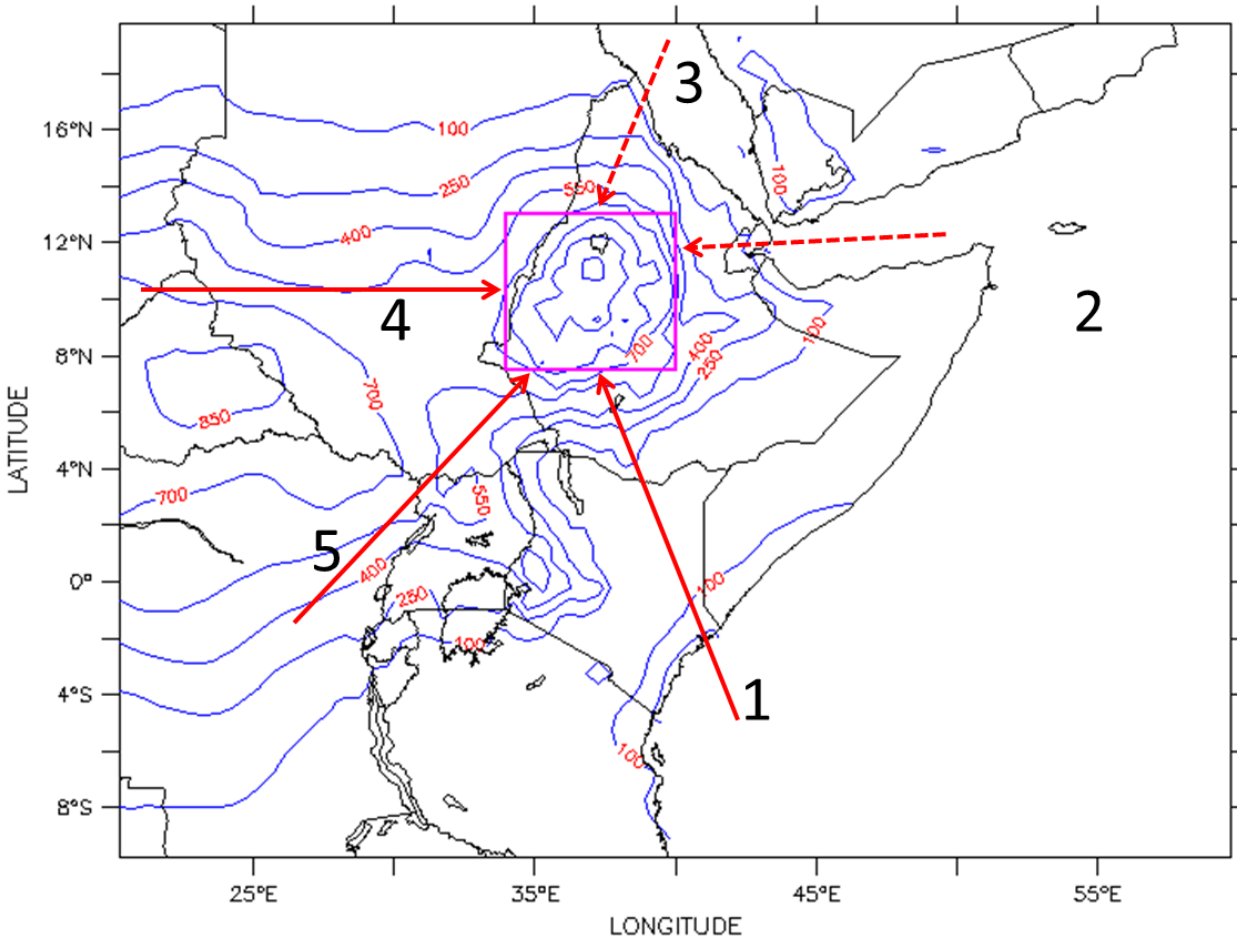

Figure 2.1. Air masses fueling rainfall in the Blue Nile basin. The box shows the approximate geographic location of the Blue Nile basin [34.25^0 to 39.75^0 E and 8.25^0 to 12.75^0 N]. The contours show average summer precipitation (mm) from the Climatic Research Unit (CRU). Arrows

represent the approximate direction of air inflow from (1) the Indian Ocean, (2) the Arabian Sea, (3) the Mediterranean and Red Sea, (4) the Sahel region, and (5) the Congo and Gulf of Guinea.

To the east and southeast, southwest monsoon winds over the Arabian Sea, a strong cross-equatorial flow along the East African coast and over the adjacent ocean, and southeasterly trade winds in the Southern Hemisphere dominate lower atmosphere circulations (Gissila et al. 2004), while to the west and southwest, moist air from the Equatorial Atlantic Ocean and the Gulf of Guinea is advected across the Sahel and the Congo into the Blue Nile basin by low level westerly winds (Segele et al. 2009; Diro et al. 2011). From October through May the ITCZ shifts southward and dry conditions prevail.

Notably, though precipitation generally peaks in July and August, its interannual variability is greatest at the beginning and end of the rainy season, in June and September (Figure 2.2), reflecting variations in the onset and cessation of summer rains. Variability early and late in the rainy season is particularly important to rainfed agriculture in the region, as delayed onset and/or early cessation can result in crop failure (Segele and Lamb 2005).

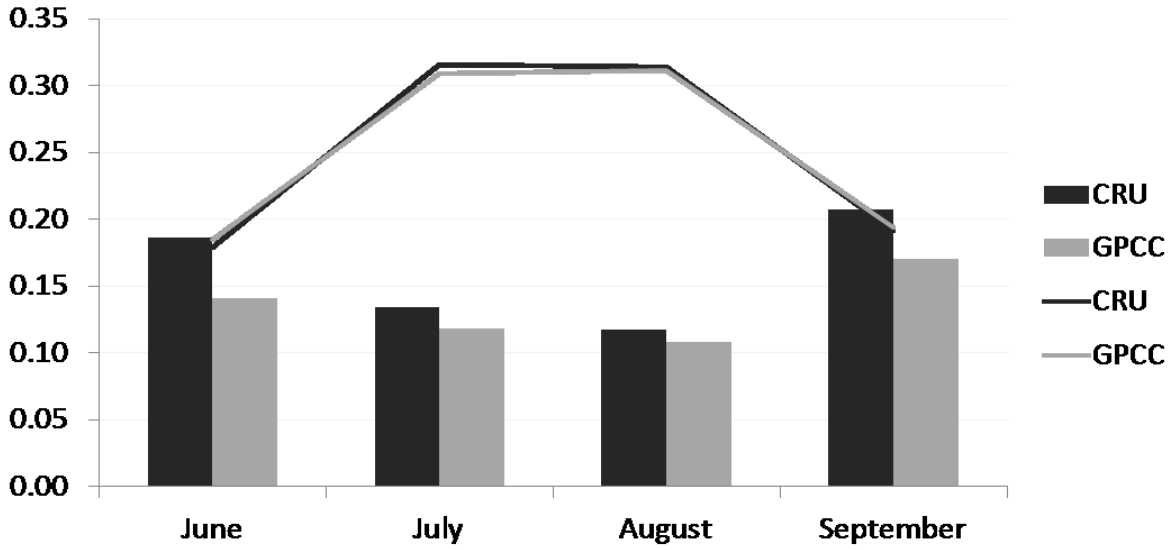

Figure 2. 2. The fraction of the summer season precipitation contributed by each month (lines) and the coefficient of variation of precipitation in each month (bars) in the Ethiopian Blue Nile from 1951-1997 using CRU and Global Precipitation Climatology Centre (GPCC) data.

Spatial variability in precipitation within the Blue Nile headwaters region is also a topic of considerable interest. There is a general pattern of humid conditions in the southern highlands of the basin grading to drier conditions in the north and west, but the dissected topography of the highlands also leads to strong local climate contrasts that include diverse patterns of total rainfall and rainfall variability (Block and Rajagopalan 2007; Krauer 1988). In the present study we focus on basin-wide precipitation, which is the variable of greatest relevance to transboundary water resources and to regional agriculture on the whole, but results obtained at basin scale will not necessarily hold at all locations within the basin.

2.1.b. Drivers of Climate Variability

Due to the magnitude and importance of precipitation variability in the Blue Nile, there have been a number of studies of the statistics, mechanisms, physical drivers, and predictability of annual precipitation in the region. In almost all cases these studies have treated the rainy season (JJAS) precipitation as a single variable and have examined interannual variability in the JJAS precipitation total (e.g., Gissila et al. 2004; Korecha and Barnston 2007; Diro et al. 2011). In this context, authors have long noted the association between annual variability in Blue Nile flows and precipitation and the Indian monsoon. This association was first noted by Sir Gilbert Walker (Walker 1910; Walker and Bliss 1932), who identified positive correlations between Indian precipitation and the Nile flood level in Egypt—which is driven largely by the magnitude of the annual Blue Nile flood. This connection has been explored in more detail by Camberlin and Wairoto (1997), who noted that strong Indian monsoon conditions lead to a pressure gradient, caused by pressure intensification in the west and lowering of pressure in the east, near the equator, which gives rise to abnormally strong westerly winds that advect moisture from the Congo Basin to Ethiopia. The importance of these westerly winds has been noted by other authors as well, though without reference to the Indian monsoon circulation.

Segele et al. (2009), for example, found that high JJAS rainfall in the Horn of Africa is associated with enhanced westerly advection of water vapor from the Atlantic Ocean and Gulf of Guinea into the Ethiopian Highlands. However, they stressed the role of a sea level pressure gradient between the Arabian Peninsula and the Gulf of Guinea, caused by intensification of sea level pressure over the Gulf of Guinea and deepening of the monsoon trough across the Arabian Peninsula—defined as the region of lowest sea level pressure over the Arabian Peninsula—in driving these winds and

associated rainfall. The importance of low-level westerly winds to precipitation in the Blue Nile and the East African Highlands more generally has also been noted in other studies (Flohn 1987; Seleshi and Demaree 1995 ; Vizy and Cook 2003; Seleshi and Zanke 2004; Mohamed et al. 2005; Korecha and Barnston 2007; Levin et al. 2009; Diro et al. 2011), though not always with reference to a driving mechanism.

The intensity and spatial extent of the St. Helena High, which is centered over the subtropical southern Atlantic Ocean, and Mascarene High, centered in the southwest Indian Ocean, are associated with variability in Ethiopian summer rainfall (Conway 2000; Gissila et al. 2004; Seleshi and Zanke 2004; Korecha and Barnston 2007; Segele et al. 2009). The St. Helena High modulates the strength of the westerlies through West Africa and southwesterlies that advect moisture to the Blue Nile from the Gulf of Guinea and the Congo basin, while the Mascarene High affects the strength of the Somali Low Level Jet (SLLJ), which influences precipitation in the second half of the rainy season.

Perhaps the most widely analyzed driver of Blue Nile precipitation variability is the El Niño-Southern Oscillation (ENSO) and its associated indices. The link between ENSO variability and annual precipitation in the Blue Nile—El Niño is associated with dry conditions and La Niña with high rainfall—has been noted in many studies (e.g., Tadesse 1994; Conway 1997, Conway 2000; Gissila et al. 2004; Segele and Lamb, 2005; Block and Rajagopalan, 2007; Segele et al., 2009). A number of mechanisms have been invoked to explain this relationship, including ENSO influence on the strength of the southeasterly flow from the Indian Ocean, which feeds precipitation events in Ethiopia from the southeast; the intensity of westerlies from the Atlantic Ocean, which bring

moisture into Ethiopia from the west; the position of the AEJ, which has dynamical effects that influence convection; the intensity of the Mascarene High, which can also affect moisture transport from the Indian Ocean; and anomalies in the North African – Asian Jet, which affects the strength of the Tibetan upper level anticyclone and can, therefore, potentially influence African precipitation through upper level Rossby waves that may weaken divergence at the exit of the TEJ (Diro et al., 2011; Segele et al., 2009; Shaman and Tziperman 2007).

In addition, the northward migration of the ITCZ in Asia is proportional to the magnitude of the easterly vertical shear of the zonal winds over the Indian monsoon region (Jiang et al., 2004), which is modulated by the tropospheric temperature gradient between Asia and equatorial Indian Ocean (Goswami and Xavier, 2005). During summertime El Niño events, cold tropospheric temperature anomalies are experienced over much of Asia, and warm anomalies occur over the Indian Ocean (Goswami and Xavier, 2005). This meridional temperature gradient anomaly decreases the easterly vertical shear of the zonal winds by altering the thermal wind balance, and as a result slows the northward migration of the ITCZ (Shaman and Tziperman, 2007). The influence that this ENSO-related influence on the ITCZ has on Indian Monsoon precipitation has been noted in previous studies (Goswami and Xavier, 2005), and the mechanism could potentially affect ITCZ migration in East Africa as well. None of these hypothesized ENSO-related mechanisms are mutually exclusive, but given the fact that such a diversity of independent mechanisms has been proposed—and the fact that most have been studied at seasonal time scales—ENSO influences in this region require further study.

2.1.c. Application to seasonal forecast

The range of perspectives on drivers of precipitation in the Blue Nile, as described above, have given rise to a range of proposals on the most effective way to predict Blue Nile precipitation at seasonal scale. The Ethiopian National Meteorological Agency (NMA) supports the leading operational seasonal forecast system, which predicts Ethiopia-wide precipitation using SST as a predictor (Diro et al., 2011).

This general approach—predicting total rainy season precipitation as a function of global sea surface temperature anomalies—has been the focus of numerous research studies by the NMA and other research groups. Researchers have differed, however, in which predictors they identify as most promising. Camberlin (1997), for example, documented that Ethiopian precipitation is more strongly teleconnected with Indian Monsoon precipitation than with ENSO, and he suggested that predictors of the Indian Monsoon precipitation can be used as predictors for summer precipitation in East Africa. Gissila et al. (2004) divided Ethiopia into clusters on the basis of gauged precipitation patterns and then constructed multivariate regression forecast models for each region. These models made use of SST anomalies of the western Indian Ocean, the tropical eastern Indian Ocean and the Niño 3.4 region. Korecha and Barnston (2007) found that the most important governing factor for Ethiopian summer rainfall, excluding the southern/southeastern lowlands, is ENSO. Block and Rajagopalan (2007) implemented a nonparametric local polynomial regression technique to predict upper Blue Nile summertime precipitation as a function of multiple large-scale predictor variables, including SST, sea level pressure, air temperature, 500 hPa geopotential height anomalies, and the Palmer Drought Severity Index. Diro et al. (2011) regionalized the

country into zones of homogeneous summer rainfall, and then generated multivariate regression model forecasts that made use of different oceanic regions and lead times for different regions.

Importantly, virtually all analyses of Blue Nile precipitation have focused on seasonally averaged precipitation (June –September) as the primary predictand of interest, though Block and Rajagopalan (2007) did describe a probability-based method to disaggregate seasonal forecasts to monthly predictions on the basis of historical correlations between total seasonal precipitation and precipitation in each month. Given the range of large-scale drivers invoked to explain and predict precipitation in this region, a more detailed temporal analysis is warranted.

Here, we consider teleconnections and potential drivers of precipitation variability for each month—June, July, August, and September—in order to characterize the general evolution of teleconnections over the course of the rainy season. In this context calendar months are used as a convenience, though it is recognized that teleconnections evolve continuously over the season. We present these analyses in order to explore reasons for the seemingly contradictory seasonal scale findings of previous studies, to describe the general mechanisms through which diverse large scale patterns of variability influence Blue Nile precipitation, and to motivate further work on prediction systems that take into account systematic differences in precipitation drivers between early, mid, and late rainy season. In addition, we include multiple precipitation and atmospheric reanalysis datasets in the analysis to assess the robustness of identified drivers and proposed mechanisms. The paper is organized as follows: Section 2.2 describes data and methods, followed by results and discussion in Section 2.3. Finally, summary and conclusions are offered in Section 2.4.

2.2. Data and methods

For all gridded analyses in this study we treat the Blue Nile basin (34.25^0 to 39.75^0 E and 8.25^0 to 12.75^0 N) as a single region. This is roughly consistent with many regional-scale analyses of East African precipitation (e.g., Camberlin, 1995 and 1997; Abitew et al., 2009; Segele et al., 2009; Jury 2010), but we note that a number of researchers have attempted more detailed regionalizations of Ethiopian precipitation that divide the Blue Nile headwaters region into several distinct sub-regions. This is the case for regionalizations by Gissila et al. (2004), who divided Ethiopia into clusters on the basis of 42 gauged precipitation patterns, and by Diro et al. (2011), who regionalized the country into zones of homogeneous summer rainfall climate using 45 gauged precipitation but presented different regions from that of Gissila et al. (2004). Our study area spans four regions in both the Gissila et al. (2004) and Diro et al. (2011) regionalizations, suggesting that further regionalization of the basin—supported with a sufficient number of station records—could offer more detailed understanding of intraseasonal and interannual precipitation variability.

2.2.a. Precipitation and Climate Data

1) Precipitation: Gridded monthly precipitation data were drawn from the Climatic Research Unit (CRU) and Global Precipitation Climatology Centre (GPCC) precipitation analyses. The GPCC data set, operated by the National Meteorological Service of Germany, is gridded at 0.5^0 latitude/longitude resolution for the earth's land surface and is generated using meteorological station data (Schneider et al., 2011). The CRU data set, which was developed at the University of East Anglia using data from meteorological stations all over the globe, contains historical monthly precipitation values for global land areas, also, gridded at 0.5^0 latitude/longitude

resolution (Harris et al., 2013). This project uses CRU TS 3.10.01 analysis (Harris et al., 2013). In the construction of this dataset, monthly station observations are converted to anomalies by subtracting the 1961-1990 normal and values more than 4.0 standard deviations from the normal are deemed outliers and excluded (Harris et al., 2013). Following that, the monthly station anomalies are gridded using triangulated linear interpolation (Harris et al., 2013). We consider the period from 1951 to 1997 because after 1997 the number of stations in the basin CRU TS 3.10.01 uses for interpolation drastically falls (Figure 2.3).

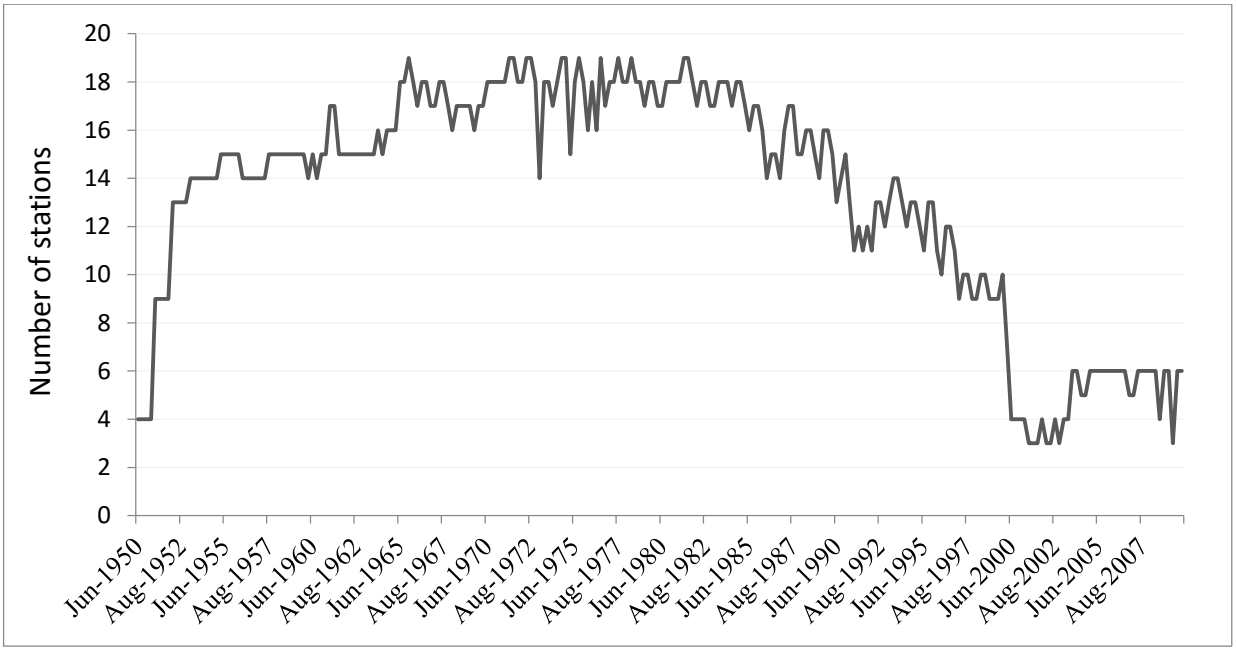

Figure 2. 3. Number of stations CRU TS 3.10.01 uses for interpolation in each month from 1950-2009 in the Blue Nile basin.

For our study area, the number of observation stations used for interpolation ranges from nine to nineteen over the period of analysis; moreover, more than 88% of the months in the study period have thirteen or more observation stations, forty-one months have eighteen observations stations and thirteen months have nineteen observation stations, while only six months have nine

observation stations. In spite of the paucity of station records employed in CRU TS 3.10.01 in the period since 1997, we did repeat all analyses for the entire 1950-2009 period and results were broadly consistent with the 1951-1997 analysis. Consistencies and discrepancies between the 1951-1997 and 1950-2009 analyses are noted as appropriate in the results section. For detailed information about CRU TS 3.10.01 product, the reader is referred to Harris et al. (2013). While analyses presented in this paper focus on these gridded precipitation datasets, monthly point precipitation records were also extracted for four in situ meteorological stations in Gonder, Bahrdar, Nekemt and Mehal Meda maintained by NMA. These stations have data records ranging from 29-44 years in length and are distributed across the Blue Nile.

2) Wind speed, sea level pressure (SLP) and sea surface temperature (SST): The monthly zonal and meridional wind speed and SLP data were drawn from the National Center for Environmental Prediction (NCEP) Reanalysis I and the European Center for Medium-Range Weather Forecasts (ECMWF) Re-Analysis (ERA-40). NCEP–NCAR reanalysis data were obtained from the NOAA Cooperative Institute for Research in Environmental Sciences (CIRES) Climate Diagnostics Center (Boulder, Colorado). It is gridded at 2.5^0 x 2.5^0 latitude/longitude resolution and spans the period from 1948 to the present. ERA-40 is a reanalysis of meteorological observations from September 1957 to August 2002 produced by the European Centre for Medium-Range Weather Forecasts using different data sources (Uppala et al., 20005). It is gridded at 2.5^0 by 2.5^0 latitude/longitude resolution. Sea surface temperature (SST) fields were drawn from the U.K. Meteorological Office's Hadley Centre global SST dataset (Rayner et al., 2003).

2.2.b. Climate indices

A wide range of climate indices and atmospheric fields was considered in this study. Our selection of indices was guided by previous studies of precipitation variability in the East African highlands and was refined through the application of multivariate regression analysis, as described below. For ENSO we include multiple indices, as this climate feature has received extensive attention in previous studies, and it is possible that correlations with Blue Nile precipitation are different for different ENSO indices. Indices considered in the analysis include:

1) Multivariate ENSO index (MEI): calculated as the first unrotated principal component (PC) of the following observations combined after normalization: surface air temperature, sea-level pressure, SST, zonal and meridional components of the surface wind, and total cloudiness fraction of the sky over the tropical pacific. The MEI values are computed separately for each of the twelve sliding bi-monthly seasons and are standardized with respect to each season and to the 1950-1993 reference period (Wolter and Timlin, 1993). The MEI is derived from long-term marine records from the Comprehensive Ocean-Atmosphere data set.

2) Niño-3.4:: defined as the SST in the east central tropical Pacific from 5^0 S- 5^0 N and 120- 170^0 W. It is calculated using NOAA Optimum Interpolation (OI) SST V2.

3) Southern Oscillation index (SOI): an index defined by a standardized monthly mean sea level pressure difference between Tahiti and Darwin.

4) Bombay monthly SLP: An indicator of monsoon activity. It is defined as the SLP anomaly at 72.8^0 E, 19^0 N, located on the western coast of India.

5) Arabian Peninsula SLP: Area average SLP over the Arabian-Peninsula over the region 40^0 -57^0 E and 15^0 – 28^0 N.

6) Equatorial Atlantic SLP: Area average SLP in the Equatorial Atlantic Ocean over the region 38^0-20^0W, 3-20^0N.

7) Pacific decadal oscillation (PDO) index: represents low-frequency changes in the SST patterns of the Pacific Ocean with centers-of-action in the northwest Pacific and eastern equatorial Pacific (Mantua *et al*., 1997). PDO index is the leading PC of monthly SST anomalies in the North Pacific Ocean poleward of 20^0 N. The index is calculated employing three different datasets: UKMO Historical SST data set for the period from 1900-1981, Reynold's Optimally Interpolated SST (V1) from January 1982-December 2001 and OISSTV2 since January 2002.

8) The Atlantic meridional mode (AMM): represented as the leading Maximum Covariance Analysis (MCA) mode in the tropical Atlantic basin (Chiang and Vimont, 2004) is used to characterize anomalous meridional gradient of SST between the tropical North and South Atlantic.

9) Tropical Southern Atlantic index (TSA): anomaly of the average of the monthly SST from the equator -20^0S and 10^0E-30^0 W. It is created using GISST and NOAA Optimum Interpolation SST.

10) St. Helena high SLP: Area average SLP over the South Atlantic High covering from 25^0 - 10^0 W and 27^0 - 20^0 S.

11) Tropical easterly jet index: Area average of the zonal wind greater than 25 m s^{-1} (Ugt25 in Table 2.2) in the TEJ region and longitude of the TEJ maximum (longmax in Table 2.2) are used.

12) African easterly jet index: calculated as the zonal wind averaged from 700-600 hPa from 5-15^0 N and 10^0 W -20^0 E.

13) West African westerly jet (WWJ) index: the area average of the 925-hPa zonal wind speed for 8.4^0–10.6^0N, 15^0-25^0W. This averaging region captures the maximum westerly wind (Pu and Cook, 2011).

14) Indian summer monsoon index (ISMI): the difference of zonal wind at 850 hPa over the region 40^0-80^0E, 5^0 -15^0N and 70^0-90^0E, 20-30^0N (Wang and Fan, 1999).

Indices 3-6 and 10-14 are calculated using NCEP-R1 data.

15) Sahel rainfall index (SRI): standardized rainfall in the region 20^0 – 8^0N and 20^0W – 10^0E and calculated using station data obtained from the National Center for Atmospheric Research World Monthly Surface Station Climatology (WMSSC). The averaging region is based on rotated principal component analysis of average June through September African rainfall presented in Janowiak (1998). The index record was obtained from the University of Washington (http://jisao.washington.edu/data/sahel/).

16) Madden–Julian Oscillation (MJO) indices: Calculated by applying an extended Empirical Orthogonal Function (EEOF) analysis to pentad velocity potential at 200-hPa for ENSO-neutral and weak ENSO winters (November-April) during 1979-2000, then constructing ten MJO indices by regressing the daily data onto the ten patterns of the first EEOF. Ten centers of enhanced convection (20°E, 70°E, 80°E, 100°E, 120°E, 140°E, 160°E, 120°W, 40°W and 10°W) for the ten indices are determined from the ten time-lagged patterns of the first EEOF of the 200-hPa velocity potential.

17) Quasi-biennial oscillation (QBO) index: zonal average of the 30 mb wind speed at the equator from NCEP/NCAR reanalysis.

MEI, SOI, Niño 3.4, PDO, MJO, AMM, QBO and TSA indices were obtained from the NOAA/Climate Prediction Center.

18) Equatorial planetary wave index (EPWI): calculated by projecting the anomalous eddy zonal wind field at 150 hPa onto the seasonally varying climatological-mean 150-hPa eddy component

of the zonal wind field over the domain 20^0N – 20^0S. This index is available since 1979 (see Grise and Thompson, (2011), for details).

2.2.c. Data analysis

In order to explore the range of regional and global variability indices listed above, and also to include the possibility of lagged effects on precipitation in each of the four months of the rainy season, it is necessary to perform some form of variable selection. Here, we employ a Generalized Linear Model (GLM) to identify significant explanatory variables in each month. In a GLM a linear predictor relates, by a link function, the linear predictor to a function of the predictor variables specifying the conditional mean (Cameron and Trivedi, 1998). The link function transforms the expectation of the linear predictor. A normal identity link function $\mu = \beta X$ is used in building the model.

Of the indices listed in Section 2.2B, only those that represent potential large scale drivers were considered as predictors: Arabian Peninsula SLP, Bombay SLP, Equatorial Atlantic SLP, Niño 3.4, SOI, MEI and PDO. Monthly averages of each predictor were introduced to the GLM, both for the concurrent month and for each leading month from April onwards. Both CRU and GPCC precipitation were used as predictands. Collinearity of predictors in each GLM was checked using a Variance Inflation Factor (VIF) measure, and covariates with VIF values greater than 10 were removed. Two different methods were used to compare fitted models for the data set: the Akaike information criteria (AIC) and a likelihood ratio test, which is used when the covariates in one model are a subset of the covariates in another model.

In this application, GLM analysis was used to focus our study on variables of demonstrated relevance to Blue Nile precipitation. The goal was not to eliminate non-significant variables from consideration in a definitive way, nor was it to develop a formal statistical predictive model; the models simply serve as a guide for further examination of mechanisms, which was performed using a combination of composites, linear correlations, and principal component analysis. For all analyses, interannual autocorrelation is found to be insignificant in all months. For analyses that involve wind speed or distributed sea level pressure fields NCEP-R1 and ERA-40 were both employed to confirm the robustness of findings. Unless otherwise noted, both datasets provided similar results, and NCEP-R1 is used in tables and figures.

2.3. Results and Discussion

The rationale for applying a sub-seasonal approach to study Blue Nile precipitation variability is clear from both qualitative and quantitative analysis. Qualitatively, patterns of correlation between Blue Nile precipitation and concurrent monthly-averaged SST anomalies differ distinctly between early and late months of the rainy season. For example, monthly composites of precipitation in the basin based on the difference between strong El Niño years and the climatological average (El Niño – climatology) and the difference between strong La Niña years and the climatological average (La Niña – climatology) show significant differences only in September (Figure 2.4D and 2.4H). We also found that June precipitation is negatively associated with specific humidity in the lower middle troposphere (700-600 hPa) averaged over the study area, while September precipitation is positively associated with specific humidity at that level. These associations are significant at 85% level—as evaluated using composite analysis statistics described by Terray *et*

al. (2003)—suggesting that regional scale processes associated with high or low precipitation also differ between the beginning and end of the rainy season.

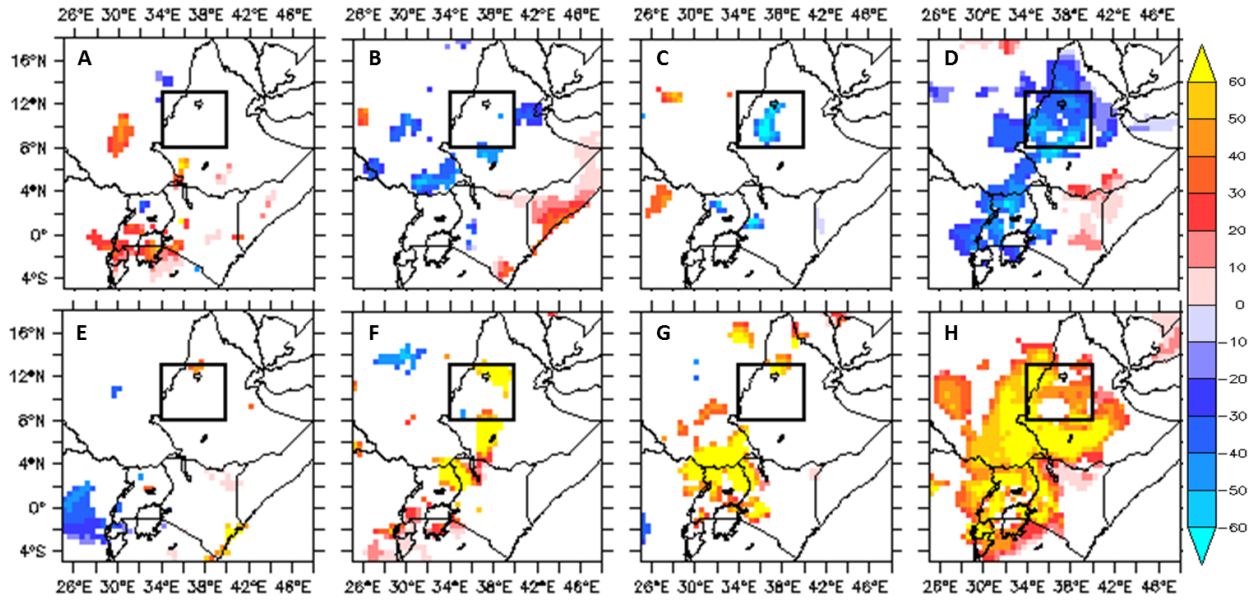

Figure 2. 4. Composites of precipitation (mm/month) based on: (A to D) strong El Niño years – climatology, and (E to H) strong La Niña years – climatology in (A,E) June, (B,F) July, (C,G) August, and (D,H) September. Shading shows results significant at the 90% confidence level. Strong El Niño years were 1957, 1965, 1972, 1982, 1991 and 1997 and strong La Niño years were 1955, 1973, 1975, 1988.

While the seasonally averaged (June to September) pattern of correlation reflects the frequently noted connection between ENSO-like SST variability and Blue Nile precipitation (Figure 2.5A), early season precipitation shows extremely weak correlations with Tropical Pacific SST (Figure 2.5B, 2.5C). The seasonally averaged pattern is almost exclusively the result of correlations found in the second half of the rainy season, particularly in September (Figure 2.5D and 2.5E). The correlation of detrended SST with Blue Nile precipitation gives similar results (not shown) indicating that the correlation pattern is not caused by SST trend. Moreover, composites of SST

based on wet-dry Blue Nile conditions give significant results in the eastern equatorial Pacific Ocean only in September and when the rainy season is considered as a single variable (not shown). We also considered impacts of outliers by removing values greater than or less than two standard deviations. As shown in Table 2.3, the correlations after removing extremes have similar pattern to the correlations shown in Table 2.2, which shows that the intraseasonal correlation of the basin precipitation with ENSO indices is stable. These correlation results are similar when the period 1950-2009 is considered.

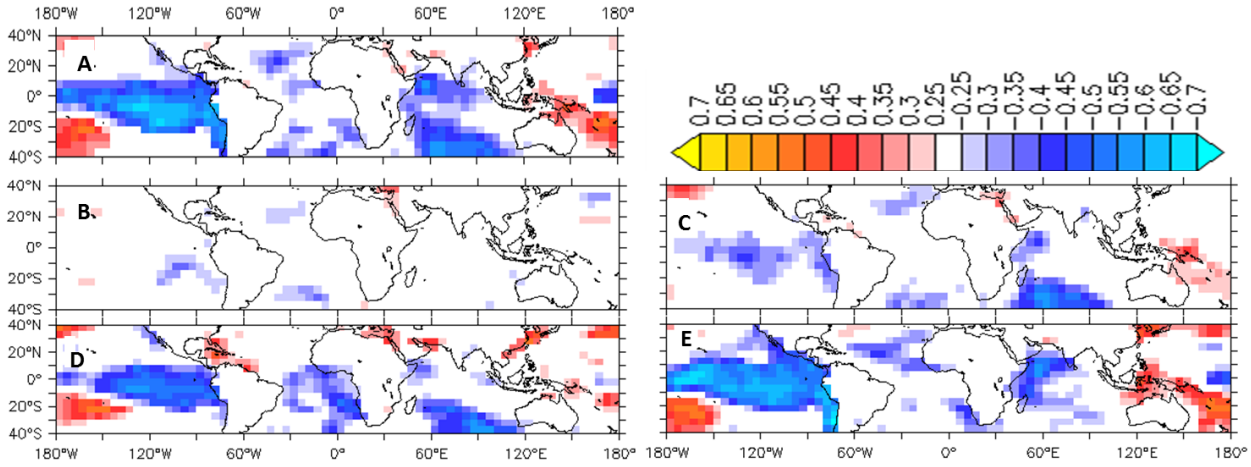

Figure 2. 5. Correlation of Blue Nile CRU precipitation with concurrent SST from 1951-1997 for. (A) the full rainy season, June-September, and (B to E)each month within the rainy season: (B) June, (C) July, (D) August, (E) September. Only correlation coefficients exceeding the 90% confidence levels are shown.

Correlations between Blue Nile precipitation and global SLP fields show a similar pattern (Figure 2.6). The seasonal correlation between Blue Nile precipitation and high pressure (La Nina-like conditions) over the equatorial and southeast Pacific Ocean and low pressure centered over the Indian Ocean (indicative of strong Indian Monsoon conditions) derives almost entirely from

correlations in August and September. In composite analysis, the ENSO-like SLP signal is significant only in September.

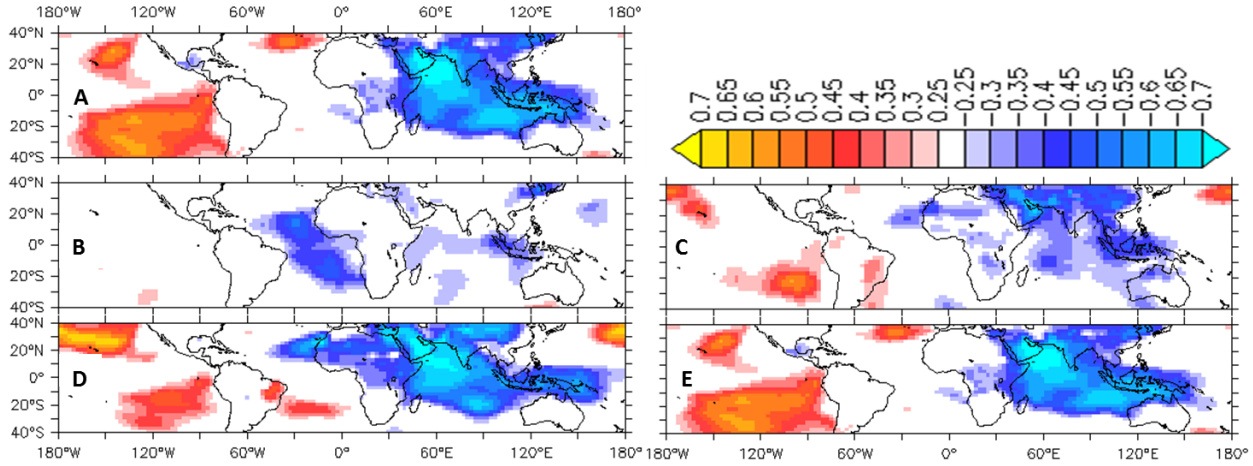

Figure 2.6. Correlation of Blue Nile CRU precipitation with NCEP-R1 SLP from 1951-1997. (A) Summer precipitation with summer SLP, and (B to E) monthly correlation of precipitation with concurrent SLP: (B) June, (C) July, (D) August, and (E) September. Only correlation coefficients exceeding the 90% confidence levels are shown.

Correlations between precipitation in the Blue Nile and concurrent SLP anomalies over the Arabian Peninsula are pronounced in July, August and September (Figure 2.6C, 2.6D and 2.6E). There is some significant correlation in June as well (Figure 2.6B), however, the center of correlation in this month is in the eastern Mediterranean Sea and surrounding areas. Arabian Peninsula SLP can influence Blue Nile precipitation through at least two mechanisms. First, Arabian Peninsula SLP shows significant negative correlation with water vapor transport at 850 hPa through West Africa in all months (June through September), with a maximum in July and August (Figure 2.7). This suggests that low SLP in the Arabian Peninsula is associated with enhanced transport of wet air into the Ethiopian Highlands from the West. Second, Arabian

Peninsula SLP is significantly negatively correlated with 850 hPa water vapor transport from the western Indian Ocean and East African coast, with maximum correlation found in September (Figure 2.7D). This water vapor convergence over the Arabian Peninsula—caused by the deepening of the monsoon trough over the Arabian peninsula which strengthens the south-to-north pressure gradient—promotes development of more intense convective systems over the Yemen highlands, which propagate westward and produce wetter conditions over Ethiopia (Segele et al., 2009).

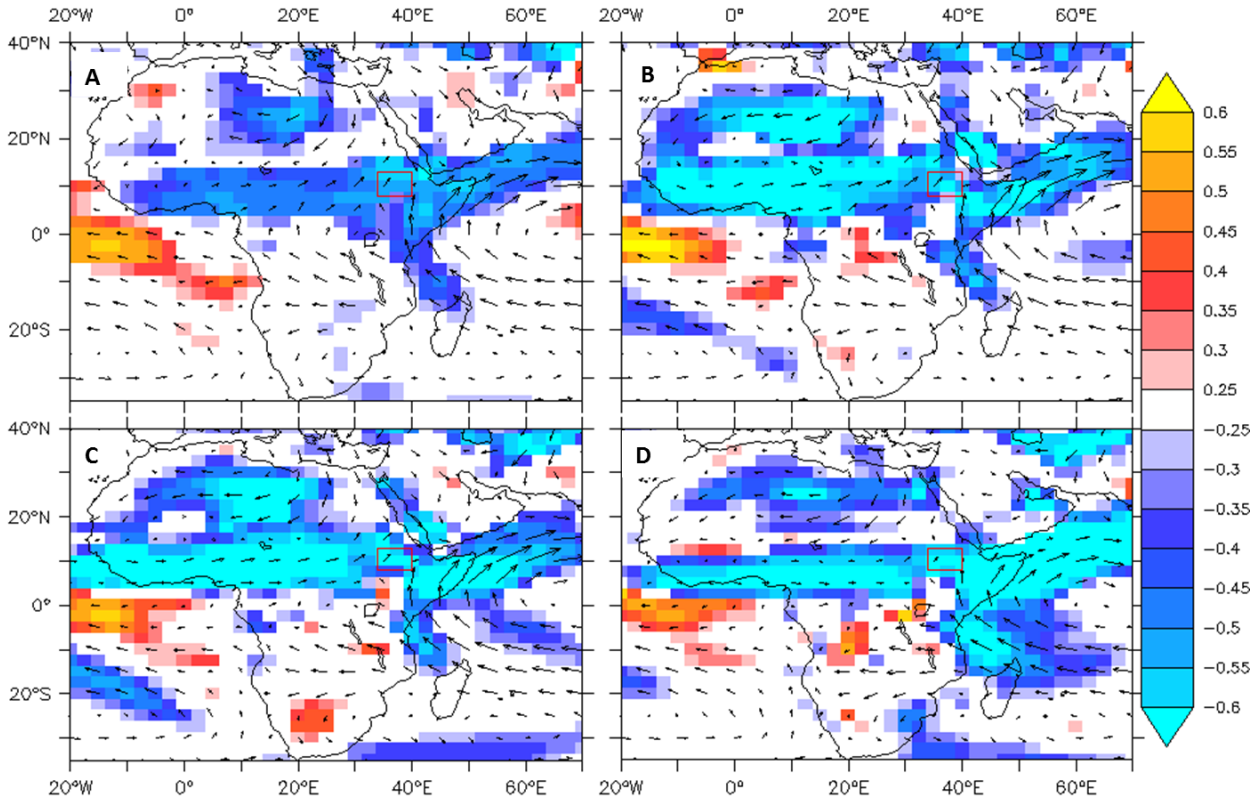

Figure 2. 7. Correlation of Arabian Peninsula SLP with concurrent water vapor transport (Horizontal wind speed x specific humidity) at 850 hPa, for the period 1951-1997: (A) June, (B) July, (C) August, (D) September. Only correlation coefficients exceeding the 90% confidence levels are shown. The box indicates the approximate geographic location of the Blue Nile basin. The arrows are mean climatology of wind.

In June, there is significant correlation with SLP in the tropical Atlantic Ocean, where low pressure is associated with wet conditions in the Blue Nile (Figure 2.6B). Correlations of Blue Nile precipitation with SLP, and Arabian Peninsula SLP with water vapor transport at 850 hPa are broadly consistent in the periods 1950-2009 (not shown) and 1951-1997.

This general sub-seasonal pattern of varying influences is captured by multivariate regression analysis as well: predictors associated with ENSO, as well as with variability in the Indian Monsoon zone, are most significant in August and September (Table 2.1). In June and July, the only significant predictors are concurrent Equatorial Atlantic Ocean and Arabian Peninsula pressure anomalies, respectively. While this analysis was not optimized for predictions—it is likely that regionalization of the Blue Nile and an exclusive focus on leading, rather than concurrent indicators would provide improved predictive skill—the clear implication is that ENSO and Indian Monsoon derived prediction models draw their skill from late season variability, and that prediction of early season precipitation requires a different approach. Indeed, time-lagged correlations between MEI and Blue Nile precipitation, for example, indicate that the predictive potential is weak at the beginning of the rainy season and progressively strengthens toward the end of the season (Figure 2.8, Table 2.2), while concurrent correlations with Indian precipitation are similarly limited to September (Figure 2.9, Table 2.2).

Significant correlations between Blue Nile precipitation and indices of the Madden-Julian Oscillation (MJO) are found in all months of the rainy season, but as monthly scale analysis of MJO indices is subject to temporal aliasing, we defer analysis of this correlation for a future study

at sub-monthly time scales. The Quasi-Biennial Oscillation (QBO) Indices show no significant correlations with Blue Nile basin precipitation in this study. Results are similar for CRU and GPCC precipitation datasets. Correlations with NMA meteorological station precipitation records were, on average, consistent with the gridded products, though the stations reveal intra-basin spatial variability.

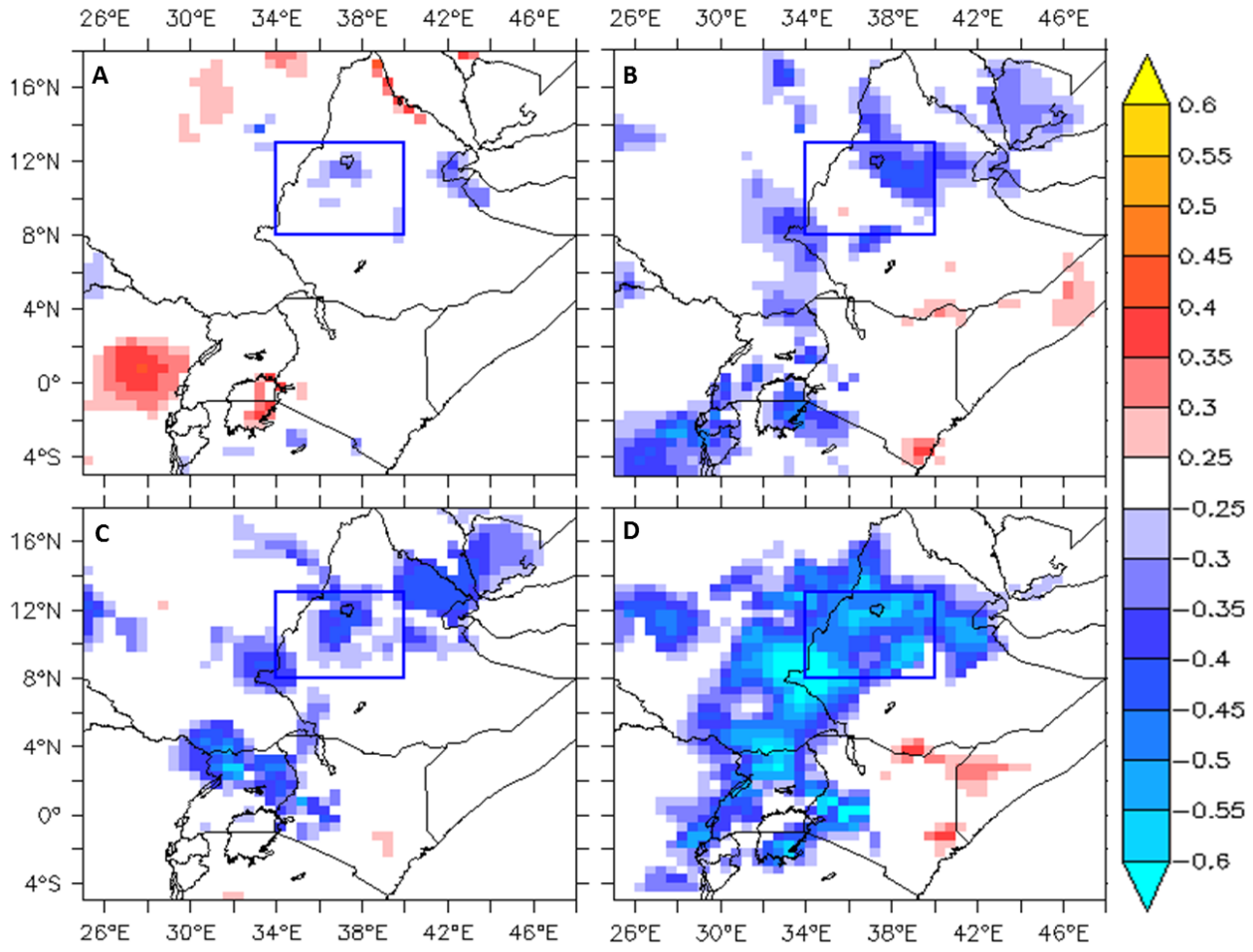

Figure 2.8. Correlations between monthly CRU precipitation and MEI, for the period 1951-1997. For each month, correlations are shown for CRU in that month and MEI in the leading month that provides the highest average correlation in the Blue Nile analysis region. (A) June precipitation with March-April MEI, (B) July precipitation with May-June MEI, (C) August precipitation with June-July MEI, (D) September precipitation with June-July MEI. Only correlation coefficients

exceeding the 90% confidence levels are shown. The box indicates the approximate geographic location of the Blue Nile basin.

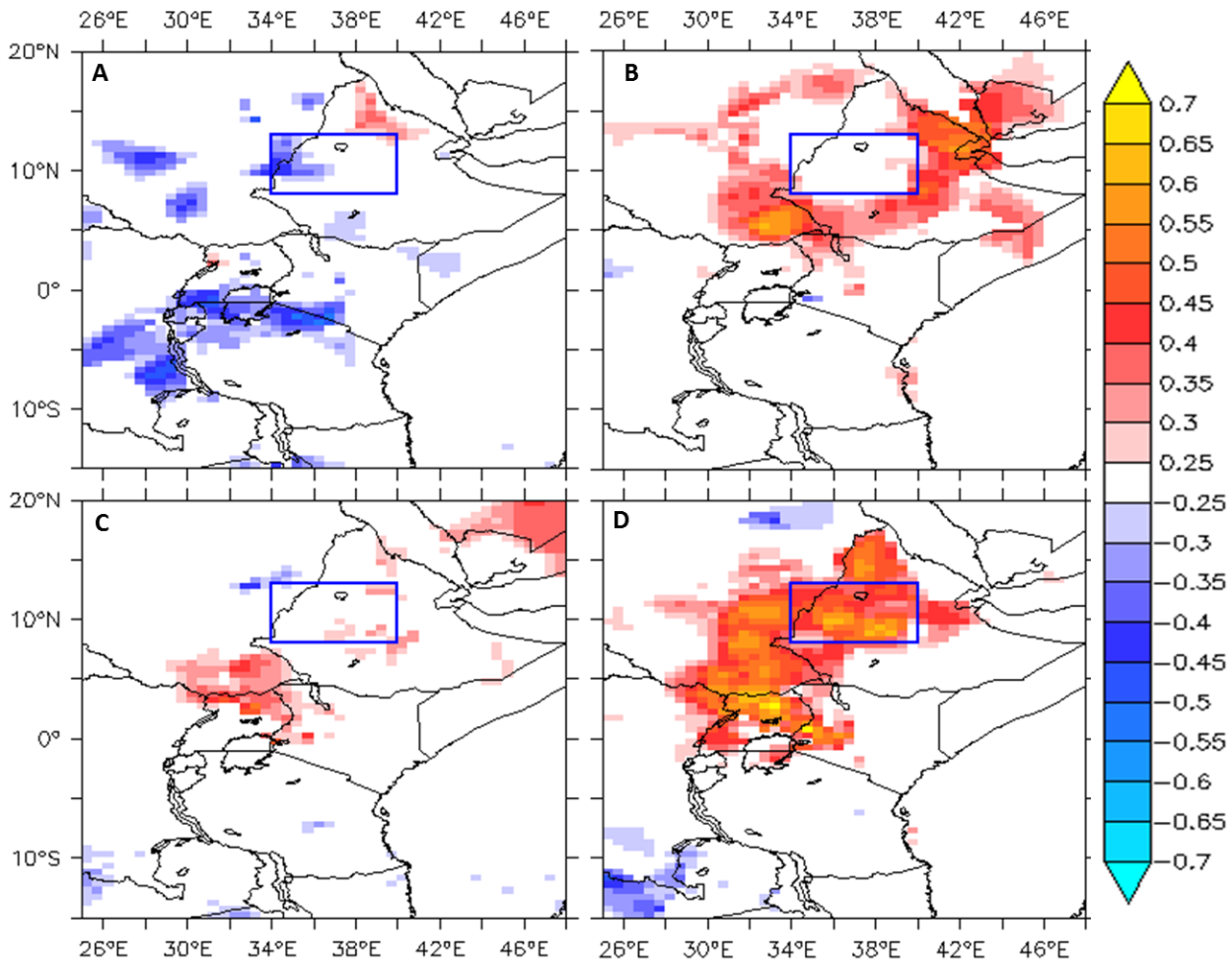

Figure 2.9. Correlation of precipitation with the concurrent southwest Indian monsoon rainfall using CRU, for the period 1951-1997 in (A) June, (B) July, (C) August, and(D) September. Only correlation coefficients exceeding the 90% confidence levels are shown. The box indicates the approximate geographic location of the Blue Nile basin.

Table 2.1. Major drivers of precipitation in the Blue Nile basin in each month as found from GLMs

June	June Equatorial Atlantic SLP**
July	July Arabian Peninsula SLP**
August	August Arabian Peninsula SLP** + July* and August* Bombay SLP + June** and August** Niño 3.4 + April PDO**
September	July Niño 3.4** + May** and September** Arabian Peninsula SLP

P-value codes[1]: ** < 0.01, * < 0.0

Table 2.2 offers a summary of all correlations found to have predictive or explanatory potential in this study, in the form of univariate linear correlations. Lead time correlations are shown only for statistically significant associations. The monthly evolution of teleconnection patterns found here strongly suggests that seasonally-averaged analyses fail to capture the full character of remote drivers of Blue Nile precipitation variability. To further explore this observation, we now consider teleconnections and proposed mechanisms in detail for each month of the rainy season, beginning with September—the month that most closely matches mechanisms emphasized by the majority of previously published studies of Blue Nile precipitation variability—and working back through August, July, and June.

2.3.a. September

September precipitation variability is strongly correlated with climate indices of the tropical Pacific and Indian Oceans. The often noted ENSO connection with Blue Nile precipitation is strongest in this month, as evident in correlations with MEI, Niño 3.4, and SOI at lead times of up to five months, and correlations with PDO with a lead of up to two months (Table 2.1). Both CRU and GPCC September precipitation show statistically significant correlations at the 99% confidence level with MEI, NIÑO 3.4, PDO and SOI. For example, CRU and GPCC reveal, respectively, correlations of -0.68 and -0.80 with July Niño 3.4. Both precipitation datasets show

significant correlations, at the 99% confidence level, with MEI starting from April-May, with Niño 3.4 starting from April, and with SOI starting from May.

A range of mechanisms have been proposed to explain the link between ENSO and East African precipitation, including ENSO-modulated variability in the SLLJ, TEJ, and westerlies and southwesterlies from the Atlantic Ocean. Correlation analysis reveals that there is significant correlation between ENSO indices and these atmospheric features, which exhibit marked.

Table 2.2. Monthly correlation of Blue Nile precipitation from 1951-1997 with different climatic indicators. Correlations in **bold** are statistically significant at the 99% confidence level. Correlation values of 0.29 and above are significant at the 95% confidence level. The indices 1-10 are potential drivers, 11-14 are mechanisms, and 15 and 16 are precipitation indices. <c> = concurrent month.

			June		July		August		September	
			CRU	GPCC	CRU	GPCC	CRU	GPCC	CRU	GPCC
1	MEI	April-May	-0.28	**-0.39**	-0.29	-0.35	-0.33	-0.30	**-0.51**	**-0.56**
		May-June	-0.25	**-0.39**	-0.31	**-0.40**	**-0.44**	**-0.39**	**-0.62**	**-0.74**
		June-July			**-0.37**	**-0.45**	**-0.50**	**-0.44**	**-0.68**	**-0.80**
		July-August					**-0.53**	**-0.48**	**-0.68**	**-0.80**
		August-September							**-0.64**	**-0.75**
2	Niño 3.4	April	-0.25	-0.35	-0.16	-0.24	-0.10	-0.10	**-0.49**	**-0.54**
		May	-0.26	**-0.39**	-0.27	-0.32	-0.20	-0.19	**-0.58**	**-0.66**
		June	-0.17	-0.29	-0.29	-0.33	-0.28	-0.28	**-0.64**	**-0.75**
		July			-0.28	**-0.37**	**-0.41**	**-0.41**	**-0.68**	**-0.80**
		August					**-0.51**	**-0.48**	**-0.67**	**-0.79**
		September							**-0.67**	**-0.76**
3	SOI	May	0.01	0.06	0.20	0.32	0.21	0.28	**0.53**	**0.63**
		June	0.20	0.23	0.32	**0.39**	0.34	0.30	**0.42**	**0.58**
		July			0.33	**0.42**	0.27	0.33	**0.51**	**0.68**
		August					**0.38**	**0.40**	**0.54**	**0.65**
		September							**0.60**	**0.68**
4	Bombay SLP	July			-0.36	-0.36	**-0.55**	**-0.41**	-0.31	-0.19
		August					**-0.56**	**-0.61**	**-0.41**	**-0.44**
		September							**-0.56**	**-0.56**
5	Arabian Peninsula SLP	May	0.02	-0.01	-0.36	-0.34	**-0.50**	**-0.51**	**-0.40**	**-0.44**
		June	-0.27	-0.33	-0.32	-0.30	**-0.43**	-0.35	**-0.39**	**-0.38**
		July			**-0.47**	**-0.46**	**-0.58**	**-0.47**	-0.33	-0.35
		August					**-0.68**	**-0.67**	**-0.39**	**-0.38**

		September							**-0.60**	**-0.58**
6	Equatorial Atlantic SLP <c>		**-0.43**	**-0.39**	-0.25	-0.23	-0.29	-0.34	-0.19	-0.21
7	PDO	July			-0.26	-0.25	-0.32	-0.24	-0.29	-0.33
		August					**-0.40**	**-0.37**	-0.35	**-0.42**
		September							**-0.52**	**-0.58**
8	AMM <c>		-0.22	-0.18	0.18	0.22	**0.51**	**0.57**	0.06	0.11
9	TSA <c>		0.13	0.14	-0.08	-0.16	**-0.40**	**-0.37**	-0.09	-0.08
10	St. Helena High SLP<c>		-0.26	-0.28	-0.02	0.02	**0.37**	0.35	0.13	0.08
11	TEJ	Ugt25	0.06	0.30	**0.45**	**0.61**	**0.47**	**0.50**	**0.53**	**0.65**
		longma	-0.12	-0.10	0.05	-0.06	-0.24	-0.26	**-0.63**	**-0.69**
12	AEJ <c>		0.02	-0.01	**0.47**	**0.47**	**0.51**	**0.57**	-0.07	-0.12
13	WWJ <c>		0.02	0.07	**0.39**	**0.57**	**0.61**	**0.60**	0.17	0.15
14	ISMI <c>		-0.09	-0.01	0.16	0.22	**0.37**	0.35	**0.62**	**0.63**
15	SRI <c>		0.25	0.23	**0.44**	**0.55**	**0.57**	**0.62**	0.11	0.14

weakening during El Niño and strengthening during La Niña (Table 2.2). In addition, Goswami and Xavier (2005) have suggested that ENSO influence on the tropospheric meridional temperature gradient between Asia and the Indian Ocean modulates the northward migration of the ITCZ, with significant influence on Asian Monsoon precipitation. Such an influence on the ITCZ might be expected to influence rainfall in East Africa as well, and we do find that there is a significant correlation between Blue Nile (CRU/GPCC) precipitation and the meridional temperature gradient between boxes 10^0-35^0 N and 15^0S – 10^0 N averaged from 30^0 -110^0 E and 700 – 200 hPa in September (0.53 CRU / 0.60 GPCC). This correlation is found in July (0.43/0.50) and August (0.42/0.47) as well.

Some researchers have documented that the TEJ is one of the phenomena most likely to control Ethiopian Highland precipitation in JJAS (Camberlin, 1997; Grist and Nicholson, 2001; Nicholson and Grist, 2003, Segele and Lamb, 2005; Segele *et al*., 2009; Diro et al., 2011). Two indices for TEJ are presented in Table 2.2. The east-west location of the jet core (longmax) shows significant correlations with Blue Nile precipitation in September only (-0.63 and -0.69 with CRU and GPCC data, respectively). As shown in Table 2.3, the correlation values are -0.68 and -0.76, for CRU and GPCC data, respectively, when values greater and less than two standard deviations are removed.

Table 2.3. Monthly correlation with Blue Nile precipitation, from 1951-1997, after removing values greater than and less than two standard deviations. Correlations in **bold** are statistically significant at the 99% confidence level. <c> = concurrent month.

			June		July		August		September	
			CRU	GPCC	CRU	GPCC	CRU	GPCC	CRU	GPCC
1	MEI	April-May	-0.15	-0.20	-0.06	-0.17	-0.36	-0.30	-0.28	**-0.40**
		May-June	-0.27	-0.36	-0.13	-0.30	**-0.49**	**-0.38**	**-0.54**	**-0.67**
		June-July			-0.22	**-0.40**	**-0.54**	**-0.39**	**-0.67**	**-0.77**
		July-August					**-0.58**	**-0.47**	**-0.66**	**-0.76**
		August-September							**-0.63**	**-0.70**
2	Niño 3.4	April	-0.20	-0.30	0.06	-0.04	-0.19	-0.17	-0.30	**-0.44**
		May	-0.21	-0.36	-0.06	-0.17	-0.35	-0.28	**-0.45**	**-0.60**
		June	-0.18	-0.32	-0.09	-0.18	**-0.37**	-0.33	**-0.55**	**-0.67**
		July			-0.10	-0.19	**-0.53**	**-0.43**	**-0.65**	**-0.75**
		August					**-0.50**	-0.36	**-0.63**	**-0.73**
		September							**-0.64**	**-0.69**
3	SOI	May	0.09	0.14	0.04	0.22	0.35	0.32	**0.50**	**0.66**
		June	0.32	0.41	0.12	0.22	0.31	0.14	**0.49**	**0.60**
		July			0.16	**0.40**	**0.42**	0.28	**0.45**	**0.69**
		August					**0.50**	**0.48**	**0.42**	**0.58**
		September							**0.59**	**0.66**
4	AEJ <c>		0.14	0.16	0.35	0.32	**0.40**	**0.45**	0.09	-0.02
5	TEJ longmax		-0.24	-0.15	-0.05	-0.11	-0.09	-0.11	**-0.68**	**-0.76**
6	WWJ <c>		-0.16	-0.06	0.32	**0.54**	**0.54**	**0.56**	0.27	0.20
7	ISMI <c>		0.00	0.01	-0.05	0.14	0.38	0.33	**0.66**	**0.61**
8	SRI <c>		0.20	0.19	0.36	**0.54**	**0.44**	**0.46**	0.22	0.20

Our analysis shows that when the jet is stronger, its core tends towards the Arabian Sea and the east African coast and is associated with more precipitation in the Blue Nile, and when it is weaker its core is located in the Bay of Bengal and Blue Nile precipitation decreases. When the TEJ weakens, divergence at the jet exit, and hence upward vertical motion, decrease, which results in reduced convection in Ethiopia (Nicholson and Grist, 2003; Segele *et al*., 2009, Diro *et al*., 2011). The other index is area-average of TEJ wind speed (Ugt25), which is taken as zonal wind speed in the TEJ region greater than 25 m s^{-1}. This index shows strong associations with Blue Nile precipitation in the second half of the rainy season and is strongest in September. Composites of

vertical motion based on strong – weak TEJ employing the TEJ indices (longmax and Ugt25) are shown in Figure 2.10; for both indices the composites of vertical motion are strongest in September (Figure 2.10D and 2.10H). The correlations between the two TEJ indices and Blue Nile precipitation are similar in the 1950-2009 and 1951-1997 time periods. For example, in September, correlations between CRU/GPCC precipitation and concurrent longmax are -0.63/-0.69 and -0.59/-0.65 for the 1950-2009 and 1951-1997 time periods, respectively.

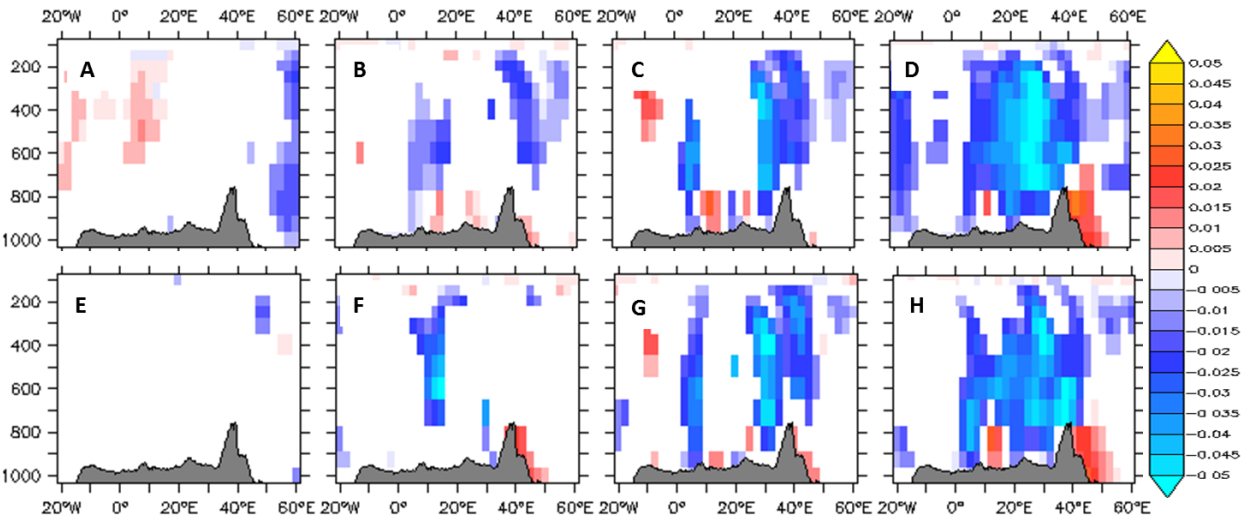

Figure 2.10. Composites of vertical velocity (Pa s^{-1}), averaged from 8.25^0 to 12.75^0 N, based on: (A to D) strong – weak TEJ longmax, and (E to H) strong – weak TEJ Ugt25. (A,E) June, (B,F) July, (C,G) August, (D,H) September. Shading shows results significant at the 90% confidence level.

Camberlin (1997) suggested that the major trigger for East African precipitation variability is monsoon activity over India, and that predictors of Indian monsoon precipitation could potentially be used as precipitation predictors for East Africa. The correlation between Indian and Blue Nile precipitation is clear in September (Figure 2.9) but not in any other month. We note that even this

very strong correlation between Blue Nile and Indian Monsoon precipitation in September can be explained in large part by the fact that precipitation in both regions is modulated by ENSO variability in this month. This can be demonstrated by partial correlation analysis: in September, partial correlation of Blue Nile and Indian precipitation when the Niño 3.4 index is kept fixed results in a significant decrease in the calculated correlation between Blue Nile and Indian Monsoon precipitation. In this month, the correlation values with Indian Summer Monsoon Index are 0.62 and 0.63 for CRU and GPCC, respectively (Table 2.2). If Niño 3.4 is held fixed, the partial correlation values drop to 0.33 and 0.29 for CRU and GPCC, respectively. These values are still significant at the 95% confidence level, suggesting that the linkage between the monsoon and East Africa is not solely due to a common response to ENSO, but the drop does suggest that ENSO variability plays a large role in observed correlations. The fact that the Indian monsoon is weaker during summertime El Niño events has been known for some time (Shaman and Tziperman, 2007). In September, correlations of Blue Nile precipitation with Indian precipitation and Indian Summer Monsoon Index over the period 1950-2009 show similar correlation and partial correlation values to those over the 1951-1997 time period shown in Figure 2.9 and Table 2.2.

As September is the month of Indian Monsoon cessation and of the last month of the rainy season in the Blue Nile, it may be more useful to explore processes that link the cessation of rainfall in these two regions than to apply Indian Monsoon predictors to East Africa in a general fashion. No significant time-lagged correlations between the two regions were found for CRU or GPCC.

Figure 2.11 shows one potential mechanism linking Indian and Blue Nile precipitation: in September (and, to a lesser extent, August as well), wet conditions in the Blue Nile—and in India

(e.g., Joseph and Srinivasan, 1999; Pai et al., 2011)—are associated with strengthened low-level flow in the western Indian Ocean. This strengthening originates in the southern hemisphere, as the southern trade winds are strengthened when low pressure in the northern Indian Ocean enhances the pressure gradient between the Mascarene High and the Monsoon Low over the Indian subcontinent. These wind anomalies manifest as stronger southeasterlies in the Horn of Africa, bringing wet air into the Blue Nile highlands from the Indian Ocean. The same wind anomoly is evident in strengthened westerlies across the Arabian Sea, bringing moisture into the Indian Monsoon zone (Figure 2.11D). Figure 2.11D also shows that Blue Nile precipitation is strongly associated with the Pacific Walker Circulation. When this circulation cell is strong, precipitation in the basin increases. Figure 2.11 was generated using CRU precipitation and NCEP-R1 wind fields, but the same patterns are evident when GPCC precipitation data and ERA-40 wind fields are used.

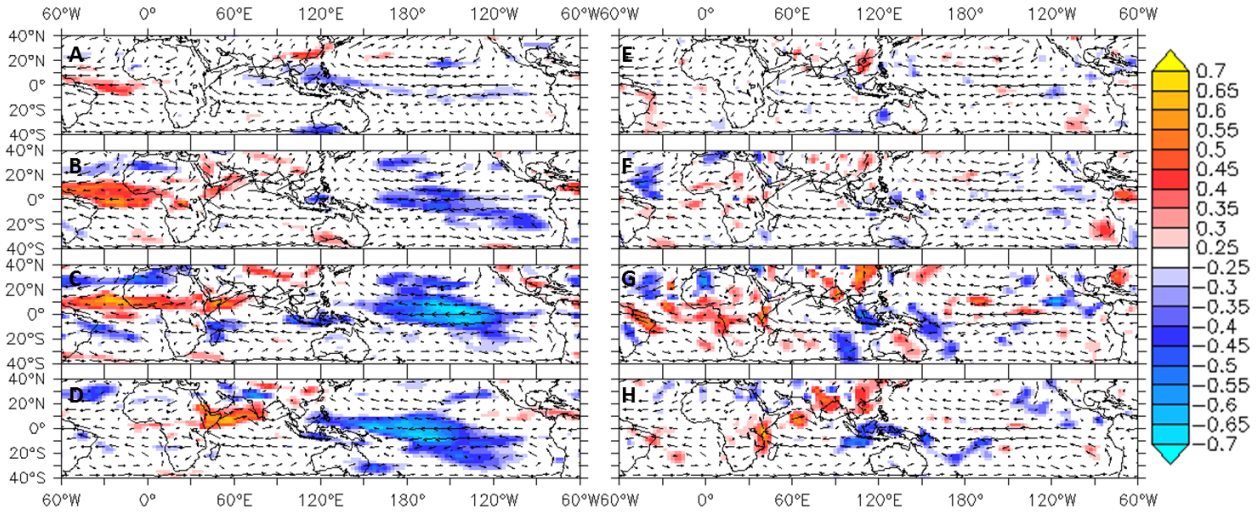

Figure 2.11. Correlation of Blue Nile precipitation with the concurrent zonal (A to D) and meridional (E to H) wind speed at 850 hPa, for the period 1951-1997. (A,E) June, (B,F) July, (C,G) August, (D,H) September. Only correlation coefficients exceeding the 90% confidence levels are shown. The arrows are mean climatology of wind.

Vizy and Cook (2003) used a regional climate model to investigate links between summer precipitation anomalies in East Africa and India by perturbing SST in the Arabian Sea and found that rainfall increases over the Blue Nile basin when the monsoon trough deepens. They associated this increase with moisture laden cross-equatorial flow penetration into southern Ethiopia through the Turkana Jet increasing moisture convergence and rainfall rates in the basin. Figure 2.5E shows that in September SST in the Arabian Sea has a negative correlation with precipitation in the Blue Nile basin, which is in agreement with the summer-scale model results by Vizy and Cook (2003). But this association is evident only in September, which again indicates that mechanisms of precipitation variability evolve over the course of the summer season.

2.3.b. August

Examining the mechanisms that are responsible for precipitation development in the basin in August, we see that some are common with September, some are common with July, and others are found exclusively in August. Commonalities with September include correlations with ENSO indices, winds of the Pacfic Walker Circulation (Figure 2.11C) and, to some extent, strength of the TEJ and phase of the PDO (Table 2.2), though all of these correlations are weaker in August than in September. As shown in Table 2.2, in August, the correlations between Indian Summer Monsoon Index and the concurrent CRU/GPCC Blue Nile precipitation are present, but they are much weaker than the correlation values in September. The result is still statistically significant at the 95% confidence level (Table 2.2), but if we include the entire 1950-2009 period in the analysis the correlation drops to below 95% significance. Composites of zonal wind speed based on wet-dry Blue Nile precipitation reveal an enhanced Pacific Walker cell in August and September only

(not shown). In August and September, concurrent partial correlations of Blue Nile precipitation and PDO keeping Niño 3.4 fixed are insignificant. For example, in September the correlation values are -0.52 and -0.58 (Table 2.2); while the partial correlation values are -0.19 and -0.2, for CRU and GPCC respectively. This suggests that the associations of Blue Nile precipitation and PDO are mainly caused by the PDO component associated with ENSO.

There is no significant association with the SST anomalies in the western Indian Ocean (Figure 2.5D) that provide a hypothesized link between the Indian Monsoon and Blue Nile precipitation, though Bombay SLP is one of the covariates of August GLM (Table 2.1), suggesting that there is some link between the regions. In contrast to September, when the most evident correlations and proposed mechanisms for precipitation variability all came from eastern influence—primarily the Indian and Pacific Oceans—August Blue Nile precipitation exhibits strong correlations with processes to the west as well. Western influences include SLP anomalies across West Africa (Figure 2.6D), low-level winds across the Sahel region (Figure 2.11C), and the West African westerly jet (WWJ; Table 2.2), which brings Atlantic Ocean moisture to the Sahel. A strong cross-equatorial pressure gradient intensifies the low-level westerlies via an inertial instability mechanism, which in turn is associated with wet conditions over the Sahel (Nicholson, 2009). All of these anomalies have the effect of enhancing moisture transport into the African continent from the west. In August—and only in August—there is also a strong correlation between Blue Nile precipitation and the anti-cyclonic surface winds in the Southern Atlantic associated with SLP in the region of the St. Helena High (Table 2.2). This result holds for both NCEP-R1 and ERA40 (not shown). Mechanistically, a strong St. Helena High pressure center is associated with strengthened anti-cyclonic winds in the South Atlantic, leading to intensified westerlies through

the Sahel and southerly winds entering the Gulf of Guinea that feed into the low level Congo Air Stream. An anomalous meridional gradient of SST between the tropical North and South Atlantic Ocean is also correlated with Blue Nile precipitation in August only, as revealed by strong correlations with AMM (Table 2.2). An anomalously cold Tropical South Atlantic Ocean SST (TSA) favors more precipitation in the Blue Nile basin (Table 2.2), though this association is not significant for the Tropical North Atlantic Ocean SST anomaly.

Finally, there is a significant correlation between August precipitation and the AEJ (Table 2.2). Yeshanew and Jury (2007) showed that a strong AEJ suppresses vertical upward motion in the Sahel regions and as far east as the Blue Nile basin. The connection between Blue Nile and western Africa precipitation processes in August is evident in the strong correlation between Blue Nile and Sahel rainfall in August, which is significant for both CRU and GPCC data (Table 2.2). The correlations between Blue Nile precipitation and Sahel rainfall, AEJ and WWJ hold up at the 99% confidence level when extremes are removed from the dataset (Table 2.3) and are generally the same when the analysis is extended to the full 1950-2009 period.

2.3.c. July

The contrast between early and late rainy season teleconnections affecting Blue Nile precipitation is quite striking (e.g., Figures 2.4-2.6, 2.9). Where August and September show clear, significant correlations with SST, SLP, and wind features associated with major modes of climate variability (ENSO, PDO, the Indian Monsoon), it is much more difficult to identify significant teleconnections affecting precipitation variability in July or in June. Nevertheless, these months account for approximately 50% of total interannual precipitation variability in the Blue Nile, so it

is well worth exploring any remote drivers that can be identified in order to understand the nature of this variability and, potentially, enhance prediction systems.

In July, precipitation variability correlates most strongly with activity of the AEJ and WWJ. Correlations with the TEJ are significant with Ugt25 but not the longmax index (Table 2.2). As noted for August, above, correlations between precipitation and the AEJ may be a function of the jet's suppression of vertical upward motion across the Sahel and Blue Nile regions (Yeshanew and Jury 2007). However, the dynamical mechanisms linking the AEJ and Blue Nile precipitation require further study. Variability in July Blue Nile precipitation is also similar to August precipitation variability in that it significantly correlates with Sahel rainfall, with correlation values of 0.44 and 0.55 for CRU and GPCC, respectively, and is similar to August and September rainfall in its significant correlation with Arabian Peninsula SLP: low Arabian SLP is associated with wet conditions in the Blue Nile. This association was also found for NCEP-R1 with GPCC, but it is weaker for ERA40 for both CRU and GPCC (not shown). The significance level of the correlations of Blue Nile precipitation in this month with concurrent Sahel rainfall and WWJ decreases from 99% to 95% from the period 1951-1997 to 1950-2009. GPCC shows correlations significant at the 99% confidence level with both indices over both time periods.

ERA40 does indicate that there is some correlation with eastern Pacific Ocean SST in July, which is not seen in Figure 2.5, but the strength of this association is much weaker in July than in August and September. There is some evidence as well for correlation with SLP in the Maritime Continent and parts of the southern Pacific as well—for both CRU and GPCC with ERA40 and NCEP-R1

— reflecting the development of ENSO-like correlation patterns that emerge in August and September (Figure 2.6).

The relationship between low pressure over the Arabian Peninsula and wet conditions in the Blue Nile in July is consistent with a mechanism of enhanced low-level westerlies across Africa that bring moist air into the East African highlands. At monthly scale we find a statistically significant relationship between the observed Arabian SLP anomaly and the strength of westerly winds affecting vapor transport to the Blue Nile basin (Figure 2.7B). The relatively weak association between ENSO and July Blue Nile precipitation compared to the stronger relationship with the AEJ and WWJ suggests that predictive models that take into account AEJ and WWJ predictors have the potential to provide more skill than ENSO-based models in this month.

July precipitation also shows significant correlation—+0.65 with CRU and +0.50 with GPCC—with the concurrent equatorial planetary wave index. Though the EPWI used in this analysis covers 19 years only, as the index is restricted to the period since the satellite era, the correlation values are significant at the 99% and 97% confidence levels for CRU and GPCC, respectively. When the data over the period 1979-2009 is considered, July EPWI gives significant correlations, at the 99% confidence level, with both concurrent CRU and GPCC (not shown). Correlations with this relatively new index are intriguing and may warrant further investigation.

2.3.d. June

Of the four months of the rainy season, June shows the least evidence of correlation with traditionally used predictors (Table 2.2) and very limited association with large scale SST and SLP

anomalies in general (Figure 2.5B, Figure 2.6B). This month does show correlations with SLP in the Equatorial Atlantic Ocean within about 20^0S – 20^0N (Figure 2.6B). This pattern is observed for ERA40 as well.

While SLP in the Equatorial Atlantic has been noted in earlier studies of East African precipitation, the proposed mechanism of association—that SLP anomalies over the Equatorial Atlantic lead to enhanced westerlies across western and central Africa (Segele et al., 2009)—requires a positive correlation between SLP in this region and Blue Nile precipitation, since it is high pressure over the Eastern Atlantic that would lead to an intensified SLP gradient between the Gulf of Guinea and the Arabian Peninsula monsoon trough. Here, we find that it is reduced SLP in the Equatorial Atlantic Ocean that strengthens precipitation in the basin (Figure 2.6B). This association was also found for GPCC precipitation (Table 2.2). The negative correlation is evident in all datasets considered in this study. It is somewhat stronger than shown in Figure 2.6B when CRU or GPCC precipitation data are used with ERA40 SLP and it is weaker when GPCC data are used with NCEP-R1 SLP (not shown). One potential mechanism that is consistent with this correlation pattern is via Equatorial Atlantic SLP associations with easterly and northeasterly winds and water vapor transport across North Africa and the Mediterranean and Red Seas. These associations are statistically significant in June, with low SLP in the Equatorial Atlantic Ocean associated with strengthened easterly and northeasterly winds and water vapor transport. This circulation pattern includes northerly to northeasterly flow that enters northeast Africa from the eastern Mediterranean Sea and Red Sea. These winds may provide significant vapor flux into the Blue Nile Basin (Viste and Soleberg, 2011) or simply contribute to enhanced convergence in the region. We note that differences between our results and those of Segele et al. (2009) might be attributed

to different timescales of analysis—they considered the entire summer season in pentad composites, while we look at monthly scale—different extent of study region, and differences in data sources and time period of analysis.

The paucity of large scale associations for precipitation in June relative to other months suggests that precipitation variability in this critical planting month could be particularly difficult to predict seasonally or to project for future climate conditions using statistical methods that employ standard SLP and SST indices. Interestingly, however, June precipitation shows very strong correlations with geopotential height anomalies across the tropical troposphere and lower stratosphere (Figure 2.12). This correlation pattern is observed for both ERA40 and NCEP-R1 when CRU precipitation data are used. The pattern is not as clear between NCEP-R1 and GPCC precipitation, though it is robust for ERA40 and GPCC. The fact that the upper level geopotential height anomalies also correlate with tropical Atlantic SLP and SST anomalies suggest that there is a connection between the pan-tropical geopotential height correlations and the tropical Atlantic influence on Blue Nile precipitation. This could be an instance of an atmospheric bridge teleconnection linking the Atlantic to the ENSO development zone, but the full mechanisms of the association require further investigation. The connection may be particularly relevant to predictions of early season Blue Nile precipitation, as correlations between upper troposphere geopotential height anomalies and June precipitation are highly significant with up to a three month lead time (March geopotential height and June precipitation).

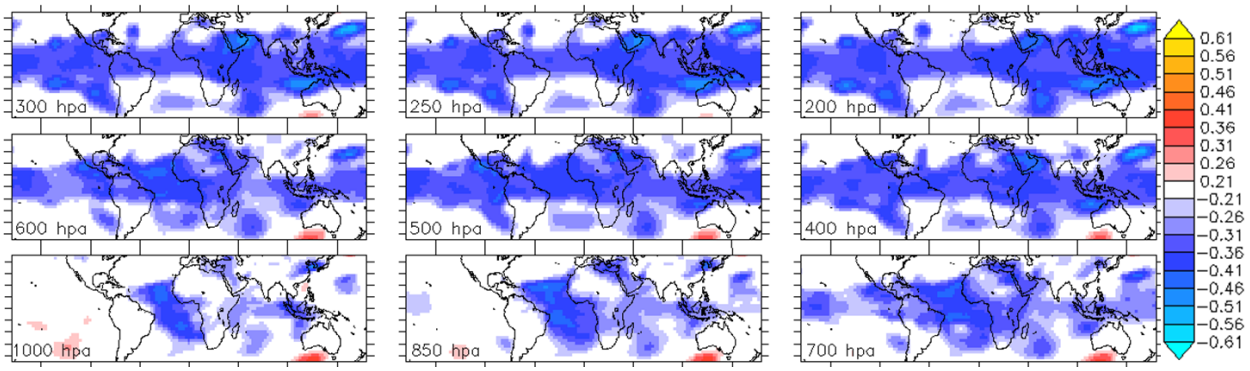

Figure 2.12. Correlations of Blue Nile CRU June precipitation with NCEP-R1 geopotential height at various pressure levels, for the period 1951-1997. Only correlation coefficients exceeding the 90% confidence levels are shown.

2.3.e. Nonstationarity

In 1976 the tropical climate system experienced a shift that included significant changes in the structure and evolution of ENSO (Graham, 1994; Wang, 1995) and climate regime changes in the Indian Ocean (Clark et al., 2000). After 1976, more El Niño and fewer La Niña events occurred than in previous years (Trenberth and Hoar, 1996). The connection between Blue Nile precipitation and ENSO appears to be similarly nonstationary. As Figure 2.13 shows, the link between Tropical Pacific SST and Blue Nile precipitation diminished after 1976. This is also true for the link with Indian Monsoon precipitation (Torrence and Webster, 1999). The waxing and waning of the associations of the basin's precipitation with different climatic indicators indicate that care must be taken in statistical analysis and prediction of rainfall in the basin. The correlations with detrended SST give similar results (Figure 2.13B and 2.13D), which shows that the correlation shift is not an artifact of the secular warming trend. When data from 1977-2009 are employed, the correlation results are generally similar to Figure 2.13C and 2.13D. In addition to the shifts in ENSO and Indian Monsoon influence, we found differences between the 1951-1975 period and

the 1977-1997 period in a number of the correlations identified in this paper. Associations between Equatorial Atlantic SLP and June precipitation, for example, appear to strengthen in the later period, as did correlations between August precipitation and St. Helena SLP, the AMM, and the WWJ. Some differences are also observed in the significance of correlation patterns with Arabian SLP, the AEJ, and the EPWI between 1951-1975 and 1977-1997, though these differences are not as dramatic. The 1976 shift also has clear implications for statistical predictability of precipitation. While ENSO associations have weakened, other correlations with significant lead-time appear to have strengthened: for example, August precipitation shows significant correlation with the preceding September-November SST in the tropical Atlantic and northwestern Indian Ocean from 1977-1997, but not in 1951-1975.

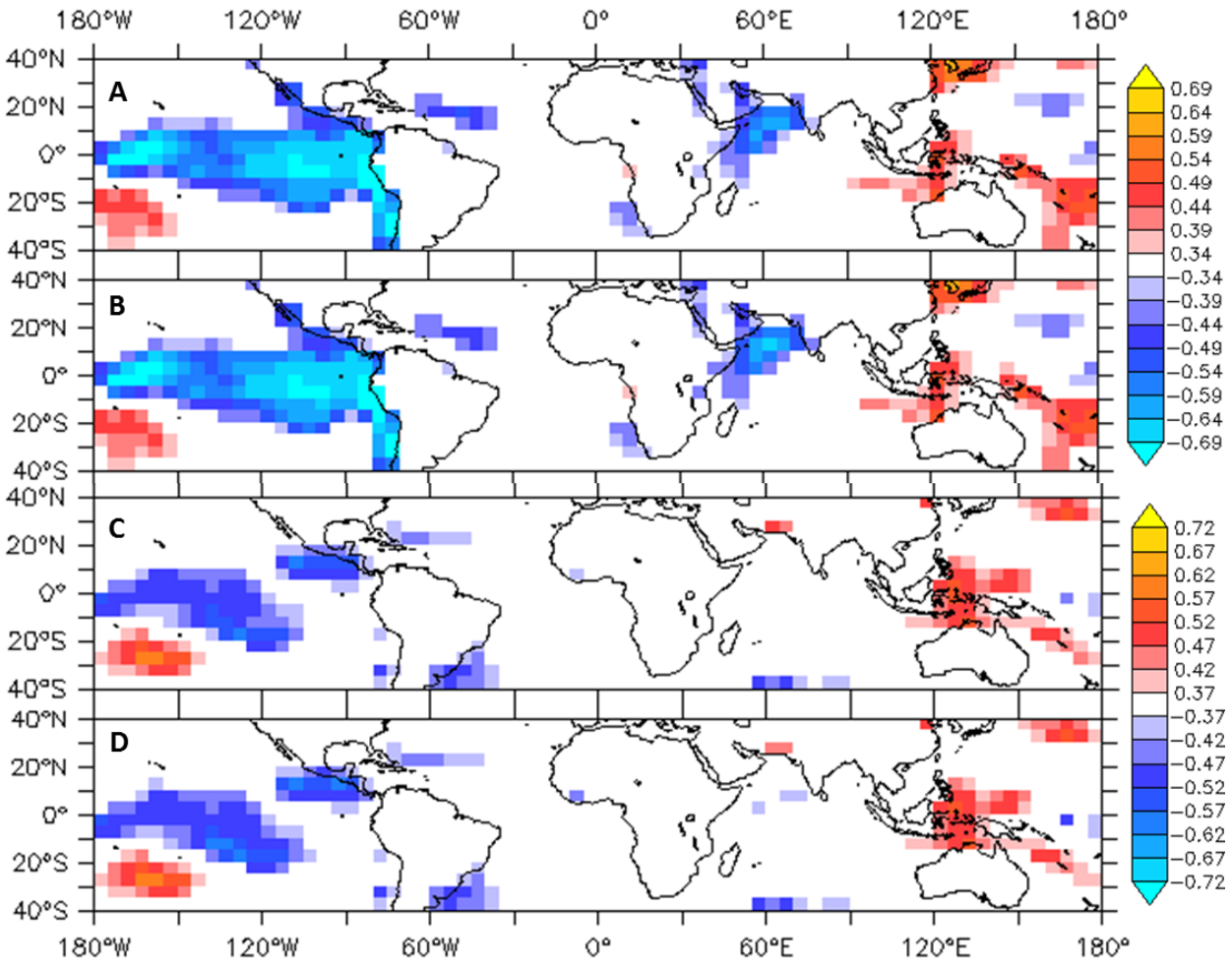

Figure 2.13. Correlation of September Blue Nile CRU precipitation with concurrent SST, (A) and (B) from 1951-1975, (C) and (D) from 1977-1997. (A) and (C) with original SST; (B) and (D) with detrended SST. Only correlation coefficients exceeding the 90% confidence levels are shown.

The 1976 transition does present a challenge for the analyses presented in this paper and for any study that employs statistical analysis of the historical observational record as a basis for exploring predictability and mechanisms of variability in tropical precipitation. On the one hand, use of the 1951-1997 baseline results in a statistical analysis that is informed by both pre-1976 and post-1976 conditions and that may not be fully representative of present, post-1976 conditions. On the other,

analyses limited to 1977-present are often too short to capture multiannual to decadal scale variability patterns. Also, insomuch as the 1976 shift may be a product of a multidecadal oscillation, an analysis that ignores the pre-1976 period is an incomplete representation of tropical variability. It is clear, however, that studies of past precipitation variability in the Blue Nile, and probably in surrounding regions as well, must consider the 1976 shift when interpreting results and applying statistical correlations to seasonal prediction or climate projection.

2.4. Conclusions

Many studies have documented that Ethiopian Highland boreal summer precipitation is associated with ENSO, while others have noted significant correlations with the Indian summer Monsoon. Still other studies have emphasized the role of the TEJ and AEJ, or have focused on correlations with the sea level pressure gradient between the Arabian Peninsula and the Gulf of Guinea and associated westerlies and south westerlies that advect moisture to the Ethiopian Highlands from the Atlantic Ocean and the Congo basin.

This study examined the associations of monthly precipitation in the Blue Nile with large-scale patterns of SST, SLP, and winds, and with a range of climate indices that have been examined at seasonal scale in previous studies. We found that associations between large-scale atmospheric and SST fields and precipitation in the Blue Nile are different in each month of the rainy season. The frequently reported correlations with ENSO are most prominent in the second half of the rainy season, and associations with the Indian Monsoon are significant at the cessation of rains. While September shows strongest associations with eastern influences—ENSO and the Indian Monsoon—in August there is evidence of an Atlantic influence as well, including strong

associations with the St. Helena High and low-level westerlies and south westerlies from the Atlantic Ocean. July precipitation, in contrast, shows limited Pacific and Indian Ocean influence, and instead correlates most strongly with the AEJ, WWJ and SLP over the Arabian Peninsula. June precipitation also exhibits only weak association with ENSO. Instead, there is evidence of strong correlation with SLP patterns in the tropical Atlantic Ocean and pan-tropical geopotential height anomalies in the upper troposphere.

June and September contribute about 20% each of the summer rainfall in the Blue Nile basin while August and July account for about 30% each, but June and September have higher coefficients of variation than July and August. Droughts in the basin are usually caused by delayed onset and/or early cessation of rainfall. Analyses described in this paper indicate that the mechanisms that govern precipitation variability in the months of precipitation onset (June) and cessation (September) are largely distinct from each other. This strongly suggests that sub-seasonal and seasonal precipitation forecasts for the beginning, middle, and end of the summer rainy season in the Blue Nile require different model structure. The results also suggest that projections of Blue Nile precipitation in a changing climate need to consider multiple mechanisms associated with Pacific, Indian, and Atlantic Ocean variability and change. Efforts to apply this information to forecasts and future climate projections will be of value for agricultural outlooks as well as for basin-scale hydrologic analysis in support of projects such as the Ethiopian Grand Renaissance Dam.

3. Chapter 3: Modulation of daily precipitation over East Africa by the Madden-Julian Oscillation[2]

Abstract

Spatiotemporal variability in East African precipitation affects the livelihood of tens of millions of people. From the perspective of floods, flash droughts, and agriculture, variability on intraseasonal timescales is a critical component of total variability. The principal objective of this study is to explore sub-seasonal impacts of the Madden-Julian oscillation (MJO) on tropospheric circulations affecting East Africa (EA) during the long (March–May) and short (October–December) rains and associated variability in precipitation. Analyses are performed for 1979-2012 for dynamics and 1998-2012 for precipitation. Consistent with previous studies, we find significant MJO influence on wet and dry spells during the long and short rains. This influence, however, is found to vary within each season. Specifically, indices of MJO convection at 70°/80°E and 120°W are strongly associated with precipitation variability across much of EA in the early (March) and late (May) long rainy season and in the middle and late (November-December) short rainy season. In the early short rains (October) a different pattern emerges, in which MJO strength at 120°E (10°W) is associated with dry (wet) spells in coastal EA but not the interior. In April the MJO influence on precipitation is obscured but can be diagnosed in lead time associations. This diversity

[2] Berhane, F., and B. Zaitchik, 2014: Modulation of Daily Precipitation over East Africa by the Madden–Julian Oscillation. *Journal of Climate*, **27,** 6016-6034.

of influences reflects a diversity of mechanisms of MJO influence, including dynamic and thermodynamic mechanisms tied to large-scale atmospheric circulations and localized dynamics associated with MJO modulation of the Somali Low Level Jet. These differences are relevant to problems of subseasonal weather forecasts and climate projections for EA.

3.1. Introduction

The Madden-Julian oscillation (MJO), which is a 30-60 day oscillation centered around the equator, is responsible for the majority of weather variability in the tropics (Madden and Julian 1994). The MJO appears as an eastward propagating large-scale system in convection, zonal winds, and upper level velocity potential (Hendon and Salby 1994). The system usually develops in the western Indian Ocean, and precipitation anomalies are recognizable as it propagates eastward to the western Pacific Ocean. When it reaches the cold waters in the eastern Pacific, it becomes nondescript. However, precipitation usually reappears as it reaches the tropical Atlantic Ocean and Africa (Madden and Julian 1971a; Madden and Julian 1972b).

The MJO is strongest in winter and weakest in summer (Wang and Rui 1990; Hendon and Salby 1994). Notably, however, no matter whether it is winter or summer, the MJO influences rainfall in a number of regions in the tropics and extratropics (Jones 2000; Paegle et al. 2000; Higgins and Shi 2001; Carvalho et al. 2004; Jones et al. 2004; Barlow et al. 2005; Donald et al. 2006; Lorenz and Hartmann 2006; Jeong et al. 2008; Wheeler et al. 2009; Zhang et al. 2009; Pai et al. 2011, among many others). Pohl and Camberlin (2006a and 2006d; hereafter PC06a and PC06b) identify Equatorial East Africa (EA) as a region in which MJO can influence intraseasonal precipitation. They diagnose an MJO influence on precipitation in both the long rains (March-May) and the short

rains (October-December) for selected regions in Kenya and Northern Tanzania, with an observed contrast of influence between highland and coastal areas. They attribute the MJO influence and the intraregional contrast to a suite of mechanisms related to deep convection, moisture advection, and stratiform precipitation.

The identification of an MJO influence in EA is both intriguing and potentially quite valuable. EA is a topographically diverse region and one of the most meteorologically complex regions on the African continent (Spinage 2012; Cook and Vizy 2013). Precipitation variability on interannual, interseasonal, and intraseasonal timescales has profound and extensively documented impacts on rainfed agriculture, pastoralism, food and water security, and human health (Epstein 1999; Funk et al. 2005; Verdin et al. 2005; Bowden and Semazzi 2007; Funk et al. 2008; Ummenhofer et al. 2009; Anyah and Qiu 2012; Lyon and DeWitt 2012; Cook and Vizy 2013). While many studies have addressed challenges of explaining and predicting climate variability on seasonal and interannual timescales (Nicholson and Kim 1997b; Indeje et al. 2000 ; Mutai and Ward 2000; Black 2005b; Owiti 2005; Hastenrath 2007; Owiti et al. 2008; Funk et al. 2008; Ummenhofer et al. 2009), relatively few have addressed intraseasonal variability on timescales that are potentially explainable, and perhaps predictable, based on MJO.

It is well known that the long rains and short rains differ in their sensitivity to large-scale climate drivers and in the characteristics of precipitation (e.g., Camberlin et al. 2009). In addition, each season exhibits systematic differences in rainfall patterns between the early, middle, and late season (Figure 3.1). These seasons are transitions between winter and summer monsoons (Hastenrath 2007) and correspond to the period when the Intertropical Convergence Zone (ITCZ)

crosses the equator in its south to north, then north to south migrations, respectively (Mutai and Ward 2000; Camberlin and Philippon 2002). The ITCZ modulates the North-East Trades blowing during the southern summer and the South-East Trades during the northern summer (Asnani 1993, Asnani 2005). Variability in the characteristics of the ITCZ is closely associated with variability in rainfall of the region (Gitau 2011).

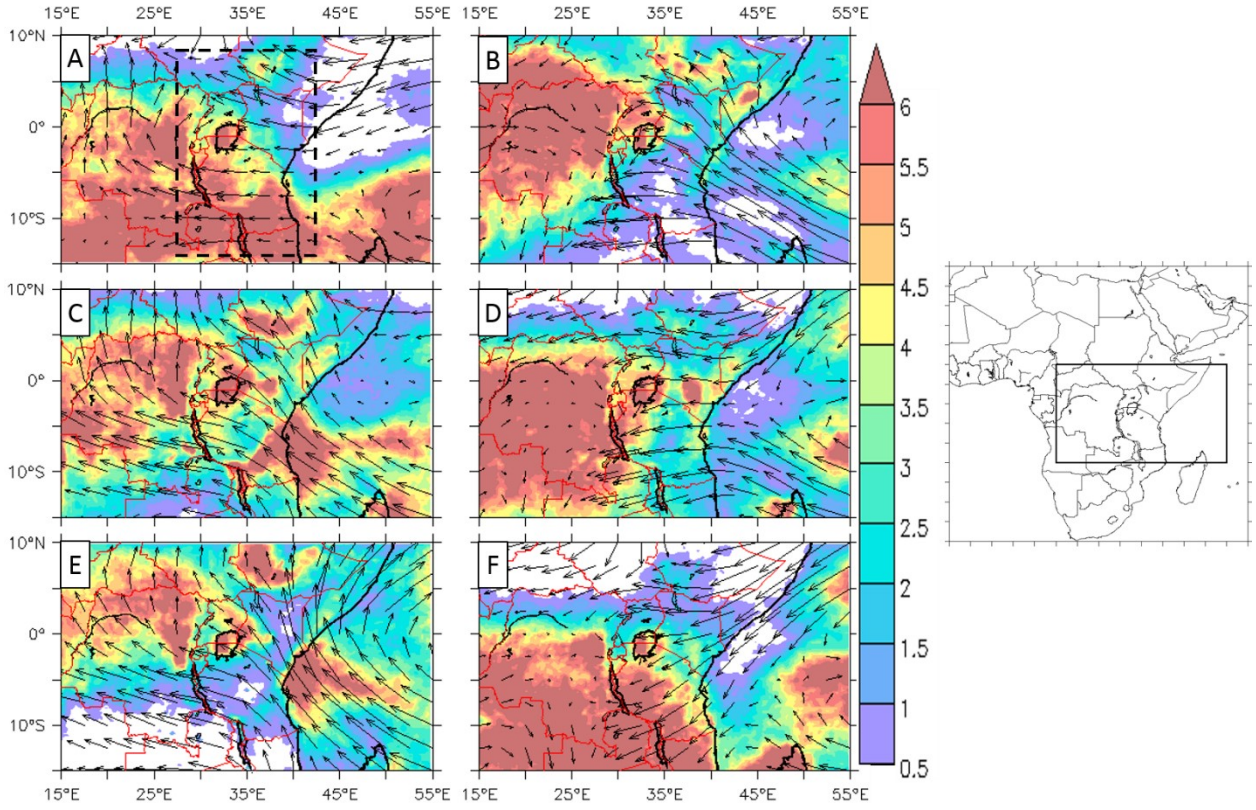

Figure 3.1. Climatology of TRMM precipitation (mm day^{-1}) and wind vectors at 850 hPa (m s^{-1}) from NCEP-R1. Precipitation values less than 0.5 mm day^{-1} are suppressed. Long rains are in the left column—(A) March, (C) April, (E) May—and short rains in the right column—(B) October, (D) November, and (F) December. The box in the top left figure shows the study region.

For the long rains, several studies have indicated that the teleconnections linked to variability also differ across the season (Camberlin and Philippon 2002; Zorita and Tilya 2002), suggesting that

atmospheric processes associated with precipitation at the beginning and end of the season are not the same (Camberlin and Okoola 2003). For this reason, authors of previous studies have recommended that studies of interannual variability consider each month of the long rainy season separately (Camberlin and Philippon 2002).

Here, we apply this reasoning to an analysis of the MJO influence on EA, using the Climate Prediction Centre (CPC)'s operational MJO index and the All-season Real-time Multivariate (RMM) MJO Index from the Centre for Australian Weather and Climate Research. The overarching objective of the study is to explore impacts of the MJO on tropospheric circulations affecting EA during the long and short rains and associated changes in precipitation on intraseasonal time scales. In this respect our analysis builds on the work presented in PC06a and PC06b, but for a larger geographic extent, more recent period, and with the analysis carried out on a month-by-month basis for both rainy seasons. These differences allow for detailed exploration of intraregional and intraseasonal variability in the MJO influence on EA. In addition, we employ multiple datasets in the analysis and explore a number of mechanisms not specifically identified by PC06a and PC06b. The paper is organized as follows: Section 3.2 describes data and methods, followed by results and discussion in Section 3.3. Finally, summary and conclusions are offered in Section 3.4.

3.2. Data and Methods

3.2.a. Data

We use multiple datasets to study associations of MJO with precipitation and tropospheric circulation. The precipitation dataset used in this study is the Tropical Rainfall Measuring Mission

(TRMM) 3B42 Multisensor Precipitation Analysis (TMPA), Version 7. The dataset has a horizontal resolution of 0.25° × 0.25° latitude/longitude (Huffman et al. 2010). Previous studies have shown that TMPA captures variability of precipitation in East Africa reasonably well, though some versions of the data have exhibited a bias in the magnitude of estimated precipitation rates (e.g., Dinku et al. 2007; Li et al. 2009; Habib et al. 2012). The version 7 multisensor product used in this study has not been evaluated in peer reviewed publication, but its behavior is similar to earlier products, with some evidence that biases in highland regions have been reduced.

Interpolated outgoing longwave radiation (OLR) estimates derived from the Advanced Very High Resolution Radiometers (AVHRR) aboard National Oceanic and Atmospheric Administration (NOAA) polar orbiting satellites (Liebmann and Smith 1996) were employed to examine MJO associated changes in patterns of deep convection. Negative OLR anomalies tend to correspond to positive precipitation anomalies, while positive OLR anomalies tend to correspond to negative precipitation anomalies.

Atmospheric fields (i.e., wind vector data, pressure velocity (omega), temperature, humidity and precipitable water) and sea level pressure (SLP) were drawn from the National Centers for Environmental Prediction (NCEP) Reanalysis I (Kalnay et al. 1996). The wind vectors and temperature are considered as "most reliable" as they strongly depend on instrumental measurements, while omega and relative humidity are considered to be "quite reliable" since they rely more on general circulation model parameterization (Pohl and Camberlin 2006b). Both the wind vector and OLR datasets are available at 2.5° x 2.5° latitude-longitude resolution and were obtained from the website of Climate Diagnostics Center (http://www.cdc.noaa.gov/). For

purposes of comparison, we repeat our analyses using SLP and atmospheric fields drawn from the ERA-Interim reanalysis, which is the latest global atmospheric reanalysis produced by the European Centre for Medium-Range Weather Forecasts (ECMWF) (Dee et al. 2011). The dataset replaces ERA-40 and addresses several difficult data assimilation problems encountered during the production of ERA-40 (Dee et al. 2011). For detailed information about ERA-Interim reanalysis products, the reader is referred to Dee et al. (2011). Sea surface temperature (SST) data were drawn from the *NOAA-Oceanic and Atmospheric Research (OAR) Earth System Research Laboratory (ESRL) Physical Science Division (PSD) high resolution (0.25°) analysis product (*http://www.esrl.noaa.gov/psd/). For *more details about this dataset, the reader is referred to* Reynolds et al. (2007).

The MJO indices used in this study are the Climate Prediction Center (CPC, Chen and Del Genio 2009) MJO index and the Real-Time Multivariate MJO Index (RMM, Wheeler and Hendon 2004). The CPC MJO index is generated by first applying an extended Empirical Orthogonal Function (EEOF) analysis to pentad velocity potential at 200-hPa for ENSO-neutral and weak ENSO winters (November-April) during 1979-2000 (Xue et al. 2002; Barrett and Leslie 2009). The first EEOF consists of ten time-lagged patterns. Then, ten MJO indices, centered at 20°E, 70°E, 80°E, 100°E, 120°E, 140°E, 160°E, 120°W, 40°W and 10°W, are constructed by regressing the daily data onto the ten patterns of the first EEOF. Positive (negative) values represent suppressed (enhanced) convection. Each index is normalized by dividing by its standard deviation (Barrett and Leslie 2009). Several previous studies have used the CPC MJO index for analyses of MJO process and impacts (e.g., Chen and Del Genio 2009; Ridout and Flatau 2011; Del Genio et al. 2012; Straub 2013, among others). The indices and their details are available on the Climate

Prediction Center (CPC) website at http://www.cpc.ncep.noaa.gov/products/precip/CWlink/daily_mjo_index/mjo_index.shtml.

The daily Real-time Multivariate MJO indices (RMM1 and RMM2) of Wheeler and Hendon (2004, hereafter WH04) are calculated as the principal component (PC) time series of the two leading empirical orthogonal functions (EOFs) of combined daily mean fields of 850-hPa and 200-hPa zonal winds and OLR averaged over the tropics (15^0 N – 15^0 S). WH04 categorized the eastward propagation of the MJO into eight phases, each corresponding to the geographical position of its active convective center (see their Figure 7). These phases constitute a full MJO cycle that is strong in the Indian Ocean and decays over the central pacific. On average, each phase lasts for about 6 days. WH04 developed a two-dimensional phase-space diagram, with RMM1 and RMM2 as the horizontal and vertical Cartesian axes, which is used for viewing the spatial and temporal evolution of the MJO. In this phase-space representation, strong MJO events move in a large counter-clockwise direction around the origin, while weak MJO variability usually appears as random movement near the origin.

Phase 1 denotes the period when the center of convective activity is over Africa. In phases 2 and 3, the convective envelope of the MJO is in the equatorial Indian Ocean; phases 4 and 5 correspond to the period when the MJO's convective envelope is in the maritime continent, and Phases 6 and 7 correspond to the period when it is in the equatorial Pacific Ocean. The square root of the sum of the squares of RMM1 and RMM2 represents amplitude of the MJO. When the amplitude of the MJO is greater than 1, the eight Phases are categorized as "strong" MJO Phases, otherwise the

MJO is categorized as “weak” irrespective of the phase of the MJO. RMM indices are available at http://cawcr.gov.au/staff/mwheeler/maproom/RMM/index.htm.

Analyses that involve precipitation are constrained by the availability of TRMM satellite data, which starts in 1998. As a result, precipitation analyses cover the period 1998-2012. OLR and dynamical analyses are presented for the modern satellite record 1979-2012, while the SST data cover the period from 1982-2012. To test the stability of MJO associations over time we repeated all 1979-2012 analyses using data only for 1979-1997 and data only for 1998-2012. Results for these two time periods are consistent at seasonal scale and for most months. Small differences between the 1979-1997 and 1998-2012 periods are noted in the results section where they are relevant.

3.2.b Data analysis

Combinations of linear correlations and composites are employed to explore associations between MJO and precipitation in EA and corresponding changes in tropospheric circulation. Composite and correlation analyses are performed at pentad scale for each calendar month of both rainy seasons in order to capture sub-seasonal variability. Pentads from March 2-March 31, April 1-April 30, May 1-May 30, October 3-November 1, November 2-December 1 and December 2-December 31 are considered for the months of March, April, May, October, November and December, respectively. MJO composites for the CPC indices are constructed using all pentads with CPC index amplitude equal to or greater than one and above, a threshold that has been used in previous studies (e.g., Chen and Del Genio 2009; Barrett and Leslie 2009). This results in between 25 and 43 composite pentads per month for the TRMM period (1998-2012). A total of 90

(204) pentads were available for each month (six per year) for 1998-2012 (1979-2012). In addition, wind and vertical velocity are analyzed at daily resolution for CPC pentads with strong MJO convection or subsidence to investigate whether the anomalies are change of strength of the prevailing motion or actual reversals. Composite figures in this paper show the difference between enhanced MJO convection and suppressed MJO convection, i.e. in each month the composites are the mean of pentads with MJO index less than or equal to negative one minus pentads with MJO index greater than or equal to one.

All analyses were repeated using daily RMM indices to verify the robustness of the results obtained employing the CPC MJO index. When using the RMM index, in each month, days with MJO index of amplitude one and above are used. Results for CPC and RMM indices are overwhelmingly similar.

To calculate composites, we first compute the long-term monthly mean for a given variable for each month as the average of all the values in each month. Composites of all variables considered are computed for each calendar month based on the MJO indices as:

$$F'(x,y,t) \quad = \quad F(x,y,t) - \overline{F}(x,y), \qquad (1)$$

where the left hand term is the pentad anomaly (daily for RMM), the first term on the right is the value of a variable on a given pentad (day) employing the CPC (RMM) index, and the last term on the right is the monthly mean of the variable considered.

Composites of OLR, SLP, vertical motion and wind vector anomalies at different levels are calculated for each MJO index. These anomalies are examined to elucidate the physical mechanisms by which the MJO impacts rainfall on monthly timescales.

To investigate changes in components of the thermodynamic balance, we employ the hydrostatic thermodynamic energy equation given by:

$$\frac{\partial T}{\partial t} = -V.\nabla T + S_p\omega + \frac{J}{C_p} \qquad (2)$$

where T is temperature, V is horizontal wind vector, *Sp* is the static stability parameter, C_p is the specific heat of dry air, and *J* denotes diabatic heating. In equation (2), the left term is tendency, while the first term on the right is horizontal temperature advection. Static stability is proportional to the vertical gradient of temperature, so $S_p\omega$ is the adiabatic term that represents the vertical advection of temperature and the effect of adiabatic warming and cooling with vertical motion. The diabatic heating term J/C_p is calculated as a residual.

Moist static energy (H) composites are also calculated at each grid point. H is found using:

$$H = c_pT + gZ + l_vq, \qquad (3)$$

where c_p is the specific heat of air at constant pressure, T is air temperature, g is gravitational acceleration, Z is geopotential height, l_v is latent heat of vaporization and q is specific humidity. Lower-tropospheric buoyancy is quantified using moist static instability which is calculated as moist static energy at 1000 hPa minus saturation moist static energy at 700 hPa (Seager et al. 2003). Saturation moist static energy (H_s) is calculated in the same manner as H (Eq. 3), but saturated specific humidity is used in place of specific humidity. Throughout much of the study region the surface lies above 1000 hPa, but anomalies of T, Z, and q at 1000 hPa and at the surface

exhibit very similar patterns, so the metric can still be used to diagnose the stability of the lower troposphere (McHugh 2004).

Composites of moisture flux divergence are calculated using:

$$MFD = q\left(\frac{\partial u}{\partial x} + \frac{\partial v}{\partial y}\right) + u\frac{\partial q}{\partial x} + v\frac{\partial q}{\partial y} \qquad (4)$$

where *MFD* is moisture flux divergence, q is specific humidity, and u and v are zonal and meridional wind vectors, respectively. $u\frac{\partial q}{\partial x} + v\frac{\partial q}{\partial y}$ represents horizontal advection of specific humidity and $q\left(\frac{\partial u}{\partial x} + \frac{\partial v}{\partial y}\right)$ denotes the product of specific humidity and horizontal mass divergence. In all analyses that involve calculations of gradients, centered difference techniques are used.

For analyses that involve wind speed, vertical motion, temperature or sea level pressure fields, NCEP-R1 and ERA-Interim are both employed to confirm the robustness of findings. The datasets provided similar results in all cases, and NCEP-R1 is used in the figures because it has been used in many previous studies in the region (e.g., Mutai and Ward 2000; Camberlin and Okoola 2003; Mchugh 2004; Hastenrath 2007; Hastenrath et al. 2007; Lyon and Dewitt 2012). To test the significance of correlation coefficients, a two-tailed t test is used. In the composite analysis, a procedure outlined by Terray et al. (2003) is used. This procedure is useful to overcome drawbacks associated with the normality assumption of the Student's t-test.

3.3. Results and discussion

3.3.a. MJO-related anomalies

The region and magnitude of MJO influence in EA varies from month to month as shown in Figures 3.2-3.5. The region of significant association in each month follows the northward and southward migration of the ITCZ as depicted in Figures 3.3 and 3.4. For this reason, we calculate correlations between the CPC MJO indices and pentad precipitation for geographic boxes centered on the area of greatest correlation in each month (Figure 3.2). Correlations vary smoothly with MJO phase: enhanced rainfall is experienced when the MJO convective center is between 20°-140°E and dry anomalies prevail when the MJO is located in the region from 140°E–10°W. The strength of these correlations is greatest for MJO indices at 70° to 80°E and 120°W. We focus primarily on 80°E and 120°W MJO indices for the subsequent analyses.

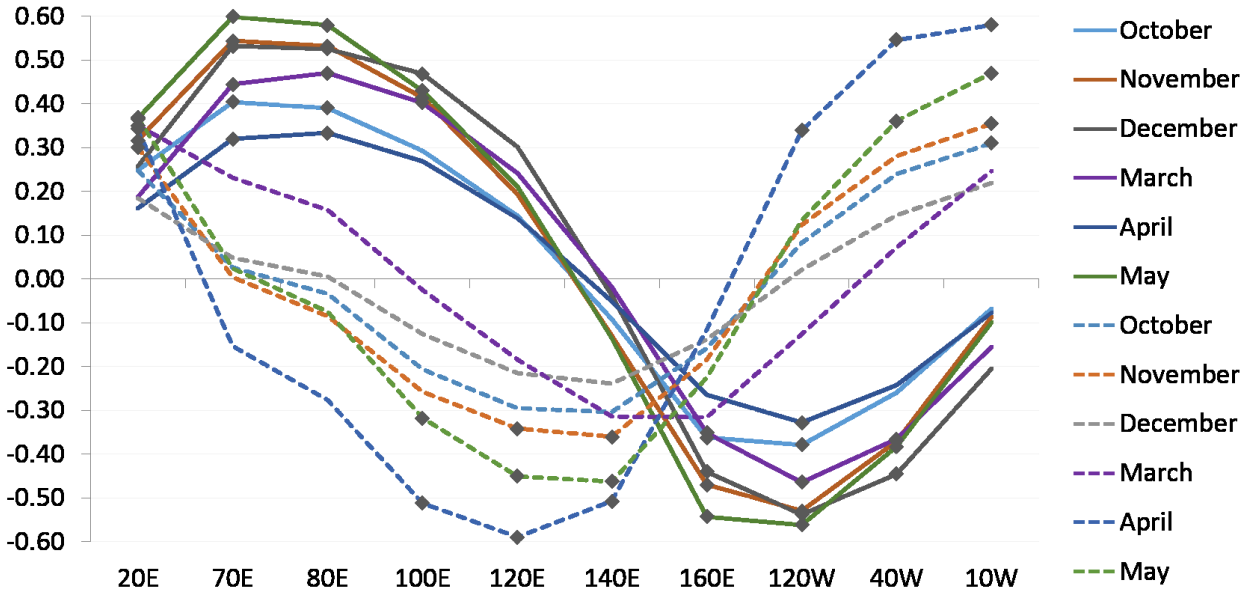

Figure 3.2. Correlations of area average precipitation over EA with each MJO index. Regions used for each month are 34°-38°E, 12°-2°S for March, 30°-38°E, 6°S-5°N for April and May, 30°-38°E, 2°S-8°N for October, 32°-38°E, 4°S-4°N for November and 32°-38°E, 10°S-2°N for December. Solid lines are correlations with concurrent MJO indices, while dashes are correlations with MJO

indices at two pentads lead. Squares show correlations that are significant at the 90% confidence level using the reduced degrees of freedom due to autocorrelation.

The spatial distributions of precipitation correlations summarized in Figure 3.2 are shown in the form of composite maps for MJO indices at 80°E and 120° W in Figure 3.3. For comparison, we have also shown composites of precipitation based on RMM phase 3, which corresponds to MJO's convective envelope over the Indian Ocean, in Figure 3.4.

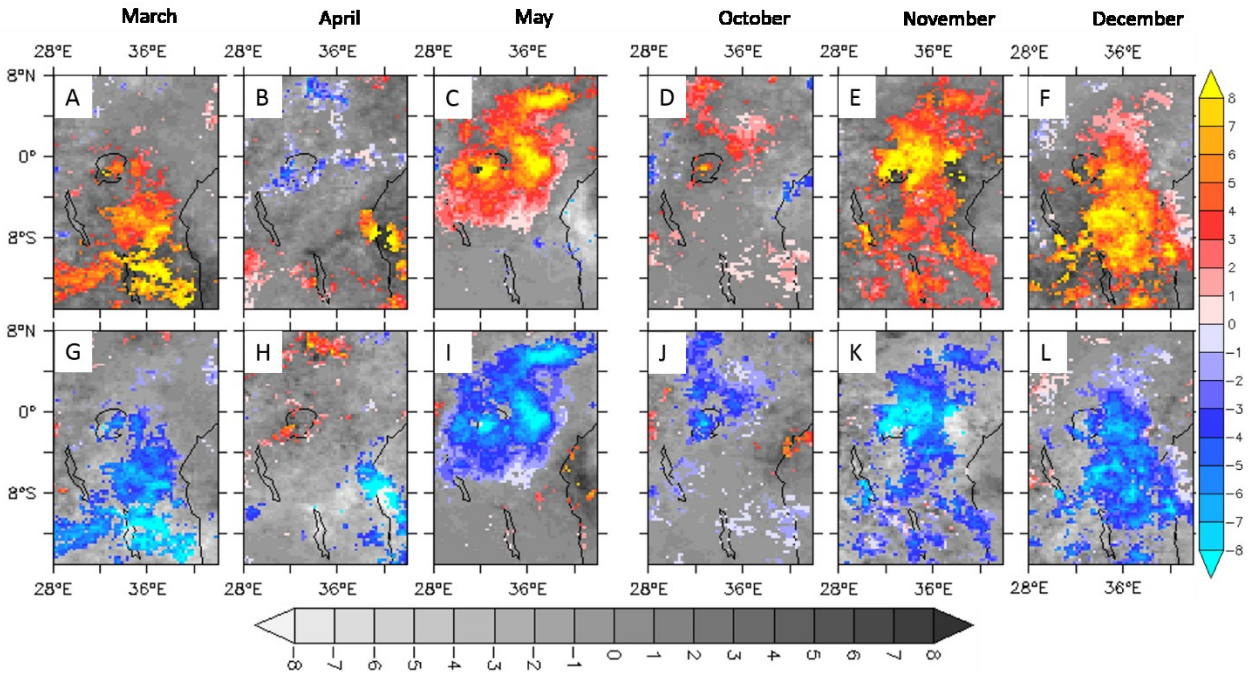

Figure 3.3. Composites of precipitation (mm day^{-1}) based MJO indices at 80°E (A-F) and 120°W (G-L) for 1998-2012. (A, G) March, (B, H) April, (C, I) May, (D, J) October, (E, K) November and (F, L) December. Non-gray shading shows results significant at the 90% confidence level. Maps of correlations at 90% significance level are nearly identical and are not shown.

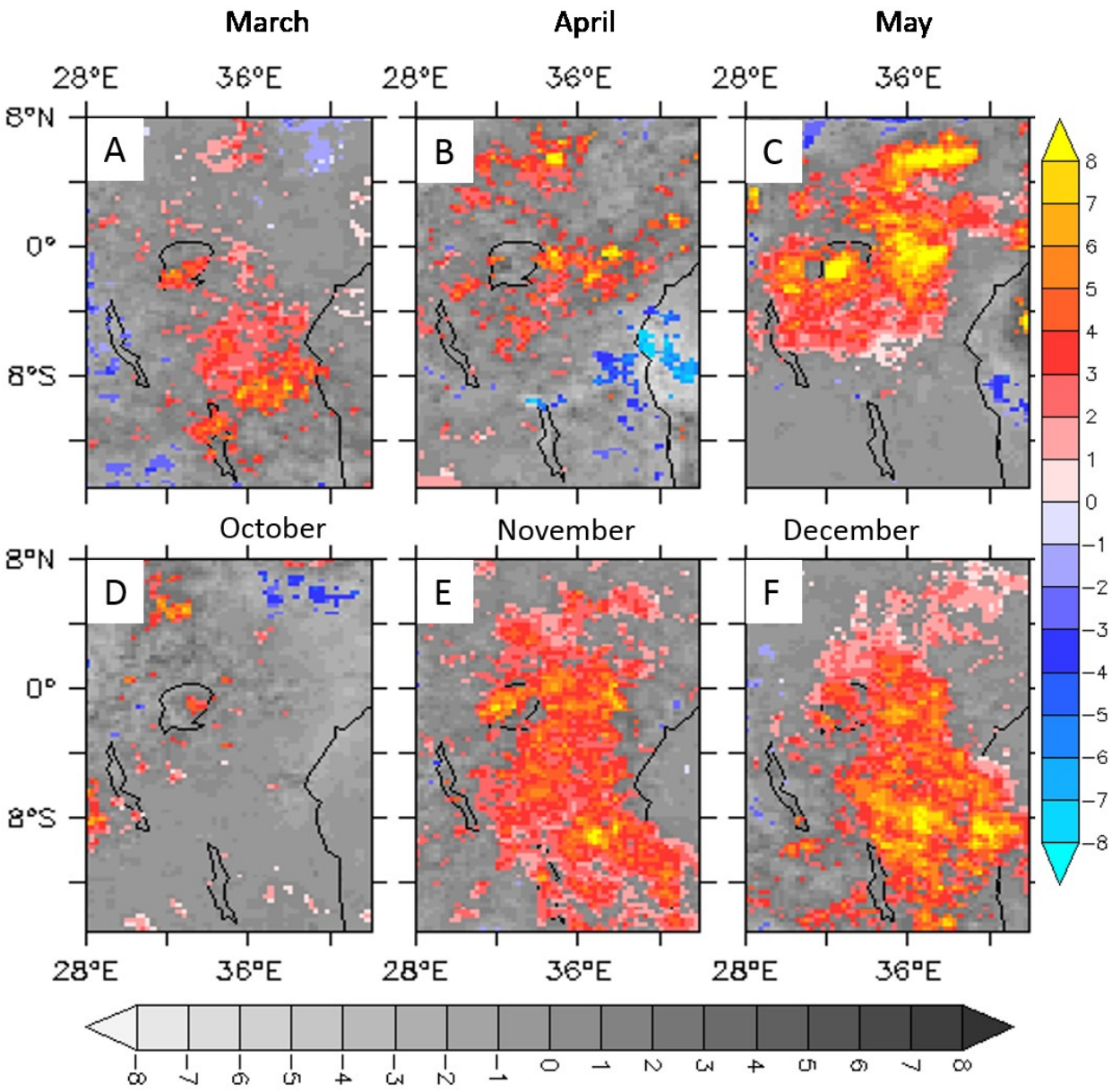

Figure 3.4. Composites of precipitation (mm day^{-1}) based RMM phase 3 for 1998-2012. (A) March, (B) April, (C) May, (D) October, (E) November and (F) December. Non-gray shading shows results significant at the 90% confidence level.

Composites of precipitation employing the RMM index and the CPC index are generally consistent. However, the composite results obtained using the RMM index are weaker than those

found using the CPC index because the composites using RMM index are calculated by deducting the climatology for each month from the average of the strong MJO events (RMM amplitude of one and above), whereas the composites using the CPC MJO index are calculated by decucting the average of strong MJO subsidence (index value of one and above) from the strong MJO convection (index value of -1 or less). This difference in analysis is a product of differences in the way that the CPC and RMM indices are calculated.

The composites confirm the fact that the association between precipitation and these MJO indices is widespread in Nov-Dec and March and May, covering large portions of the study region. The relationship is weaker in October and April. The EA coast is also affected by MJO at 80°E and 120°W to some degree (Figures 3.3 and 3.4), but in the coastal zone another MJO influence appears in October, when a strong association with MJO indices at 10°W and 120°E is evident (Figure 3.5). This October MJO association is distinct from the highland MJO influence in location and timing, suggesting that a different mechanism of influence may be active. Maps of precipitation correlations with the CPC MJO index are very similar to the composite maps included in Figures 3.3 and 3.5 and are not shown.

Relatively low associations between MJO indices and EA precipitation in April might be interpreted as a pause in MJO influence in the middle of the long rainy season. However, our analysis suggests that the apparent pause might simply be a result of the fact that the characteristics of the MJO vary from month to month and, as has been shown in previous studies, from decade to decade (Suhas and Goswami 2010). As such, no single, seasonally static MJO index system offers a perfect or complete representation of the MJO phenomenon. As shown in Figure 3.2, there are

large correlations between April EA precipitation and the MJO index at 10°W and 120°E at two pentad lead time.

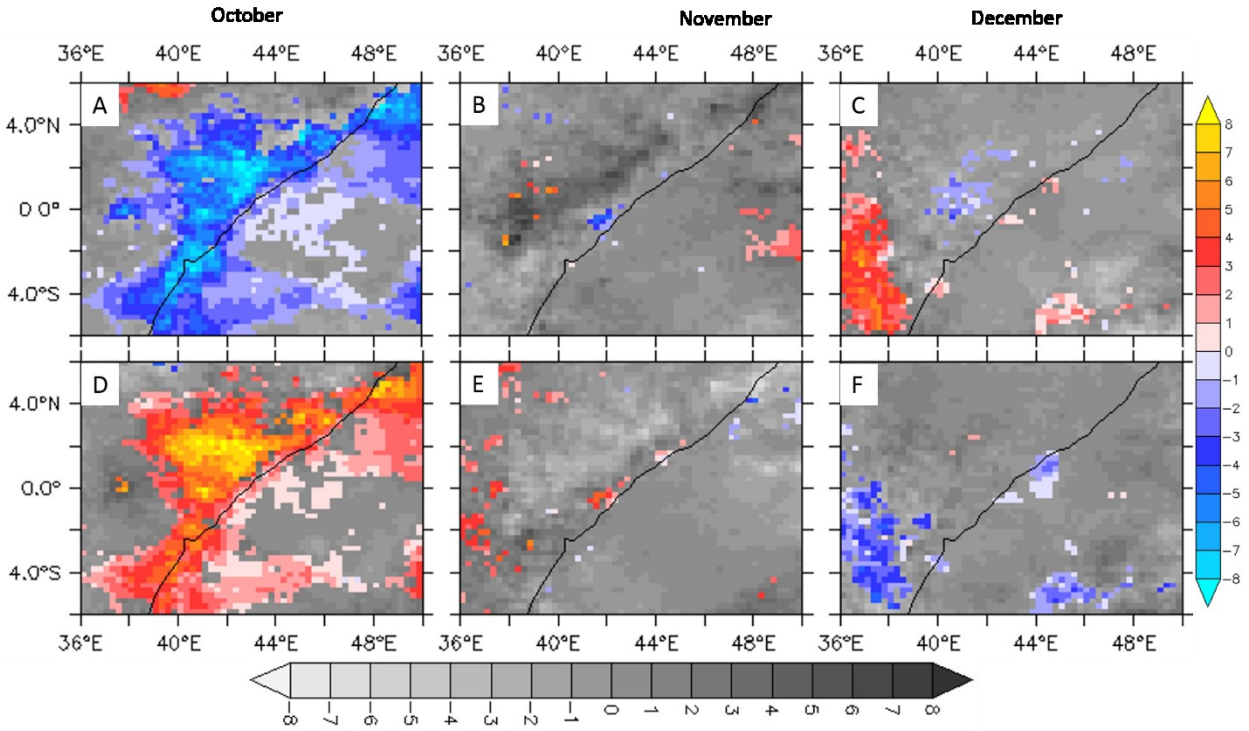

Figure 3.5. Composites of precipitation (mm day^{-1}) for 1998-2012. (A-C) based on MJO index at 120°E and (D-F) based on MJO index at 10°W . (A, D) October, (B, E) November, (C, F) December. Non-gray shading shows results significant at the 90% confidence level. Correlation maps at 90% significance level are nearly identical and are not shown.

These correlations are conceptually consistent with the zero-lag correlations found in March and May, as the MJO propagates at speeds of 4-8 m s^{-1} when convectively coupled in the Indian Ocean, but at speeds as high as 30-35 m s^{-1} when uncoupled from convection in other regions (Zhang 2005). This means that a two pentad lead correlation with MJO activity at 10°W, for example, can be roughly indicative of zero-lag correlation with MJO activity in the vicinity of 70-80°E. Indeed,

as described in Section 3.3b, below, the mechanisms that underlie these two pentad lead correlations in April are quite similar to those associated with zero-lag correlations in March and May. This would seem to indicate that the lack of a strong zero-lag signal results from the fact that high and low precipitation anomalies in EA are associated with patterns of Indian Ocean convection that do not align perfectly with CPC MJO indices at 70°E and 80°E during this month. Indeed, zero-lag associations are significant for all intermediate variables linking MJO to EA precipitation (OLR patterns, vertical motion, and proposed dynamic and thermodynamic links described below) when analyses are performed for the longer 1979-2012 period or for 1979-1997. This is true for both CPC and RMM MJO indices. This strongly suggests that there is a link between MJO activity and EA precipitation processes in April and that the lack of strong zero-lag association in the TRMM period of analysis results from some combination of nonstationarity in MJO behavior and in the difficulty of characterizing an evolving phenomenon like MJO with static index systems. This interpretation of statistical shifts in April is speculative and is a subject of our ongoing research. For consistency in presentation, we show zero-lag results for all months throughout this section. Lead time associations will be re-introduced in Sections 3.3b and 3.3d.

OLR composites corresponding to the TRMM period (not shown) are consistent with the precipitation analysis, showing strong associations between anomalies in deep convection in EA and convective activity in the Indian Ocean when MJO activity is centered at 80°E for all months that show significant associations between MJO at 80°E and precipitation. The opposite pattern is seen for composites on MJO convection at 120°W and similar patterns are seen in April for two pentad lead composites on MJO indices at 10°W and 120°E are employed. For OLR, however, we are able to perform pentad and daily analysis for a period that is not limited by the TRMM record.

Figure 6 shows composites of OLR using concurrent 80°E and 120°W CPC MJO indices for the entire study period (1979-2012). These composites are consistent with the composites in 1998-2012 time period, with the exception that April composites for this period do show significant zero-lag OLR anomalies. This result is further evidence that April precipitation in the region is, in fact, affected by MJO. The lack of significant zero-lag association seen in TRMM composites reflects variability in the MJO activity, its influence on East Africa, and/or the ability of standard MJO indices to capture these connections. The possibility of variability in the strength of MJO associations in EA is dicusssed in Section 3.3c. OLR composites generated using the RMM phase 3 and 6 indices give similar but weaker results for both 1979-2012 (Figure 3.7) and 1998-2012 (not shown).

The consistency of TRMM and OLR results reflects strong correlation between precipitation and OLR variability in the region: at pentad scale, these correlations range from -0.81 to -0.89 in the months of both the long and short rainy seasons (using the averaging boxes described in Figure 3.2), confirming that precipitation variability in the region is predominantly due to deep convection. Interestingly, OLR conditions indicative of deep convection in EA (i.e., strongly negative OLR anomaly) are in phase with convective activity in the MJO center of convection but are not contiguous with the core convection feature. In all cases, there is a gap or weakening in the OLR anomaly off the eastern coast of Africa that separates the EA convection anomaly from the MJO center of action. This suggests that the EA precipitation anomalies cannot simply be explained as a dynamical extension of MJO convection in the Indian Ocean. A mechanism of communication is required.

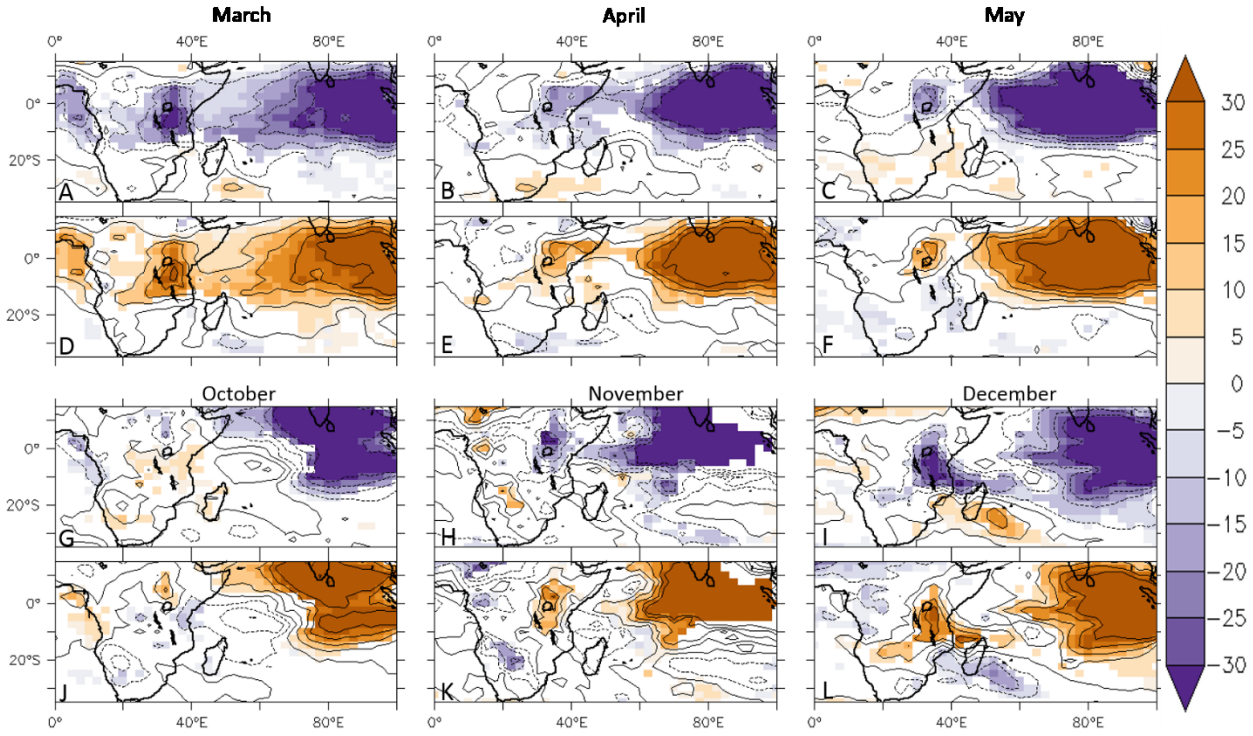

Figure 3.6. Composites of OLR (W m^{-2}) based on MJO indices at 80°E (A-C, G-I) and 120°W (D-F, J-L) for 1979-2012. (A, D) March, (B, E) April, (C, F) May, (G, J) October, (H, K) November and (I, L) December. Shading shows results significant at the 90% confidence level.

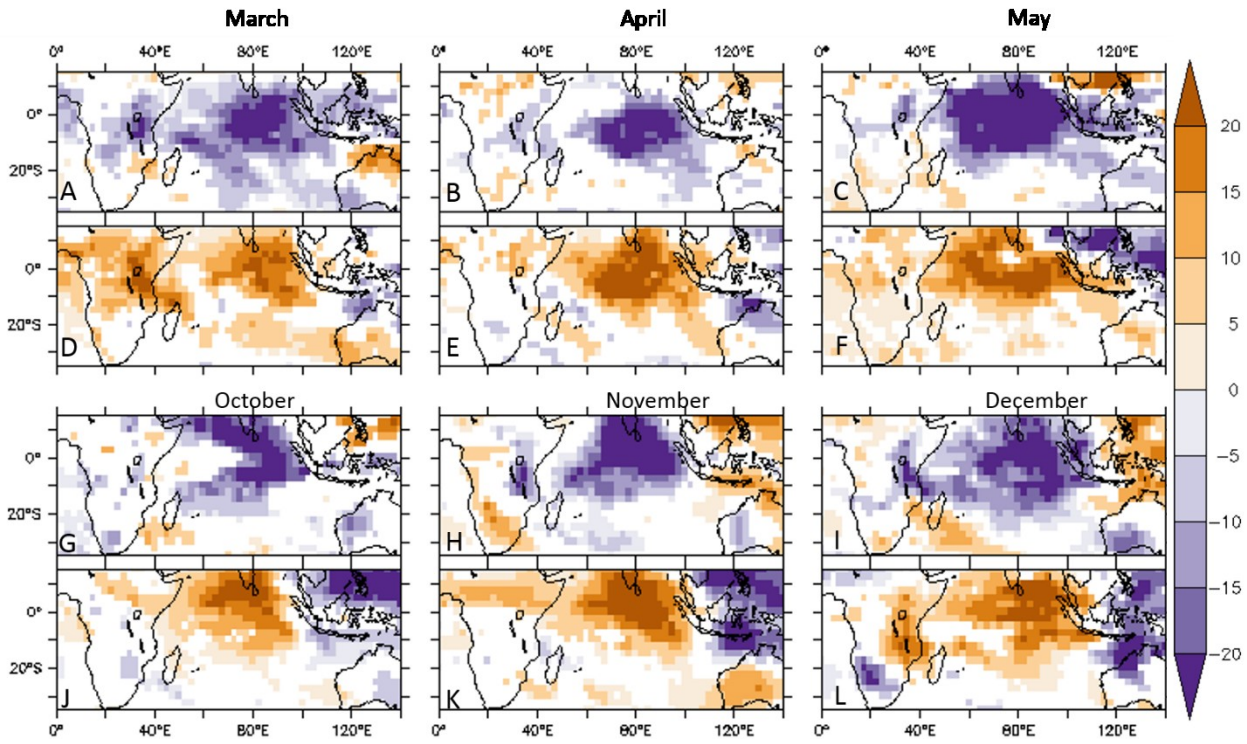

Figure 3.7. Composites of OLR (W m^{-2}) based on RMM phase 3 (A-C, G-I) and phase 6 (D-F, J-L) for 1979-2012. (A, D) March, (B, E) April, (C, F) May, (G, J) October, (H, K) November and (I, L) December. Shading shows results significant at the 90% confidence level.

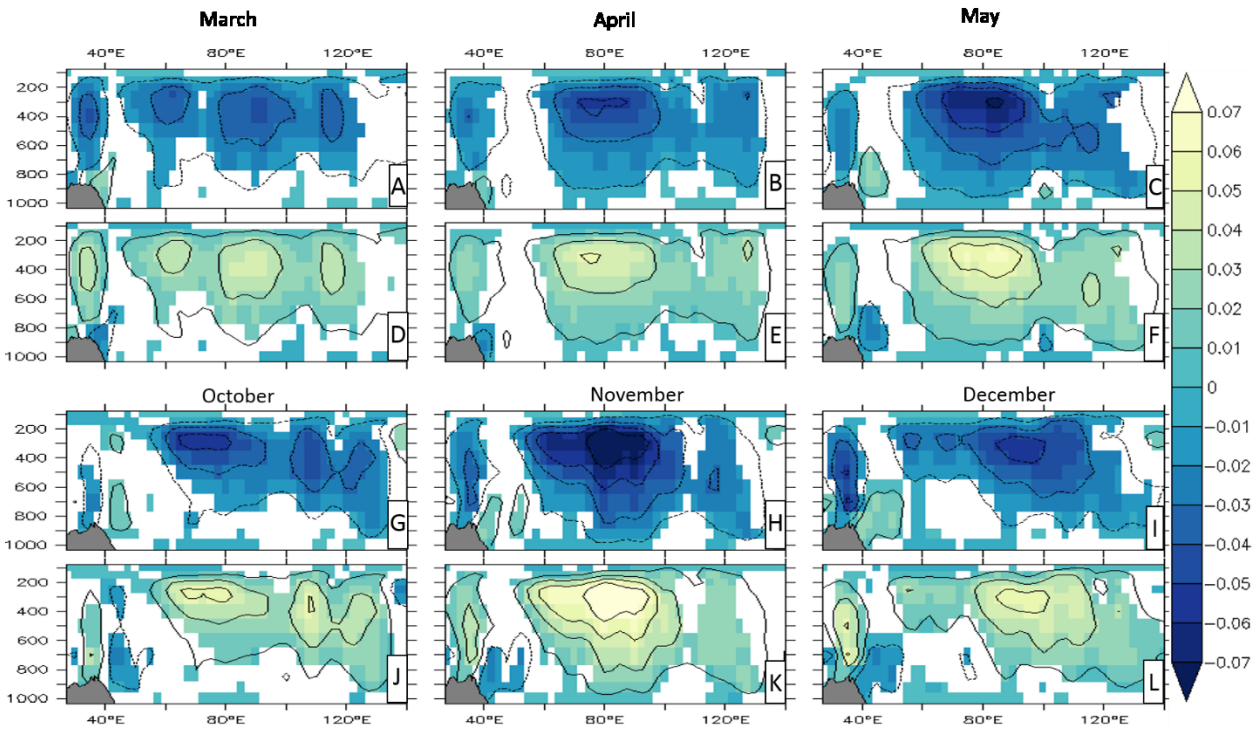

Figure 3.8. Composites of vertical velocity (Pa s^{-1}), for 1979-2012, based on MJO indices at 80°E (A- C, G- I) and 120^0 W (D- F, J- L). (A, D) March, (B, E) April, (C, F) May, (G, J) October, (H, K) November and (I, L) December. Shading shows results significant at the 90% confidence level.

MJO-related anomalies are also evident in vertical motion fields over EA (Figure 3.8). These anomalies represent an actual reversal of rising and descending motion in some cases and a weakening of prevailing motions in others. These anomalies were generated using NCEP-R1 vertical velocity fields, but the same patterns are evident when ERA-Interim vertical velocity data are used. During this period, when the convective envelope of the MJO is in the Indian Ocean (80°E), there is significantly enhanced upward vertical motion over EA in the months of March, May, November and December, and corresponding wet anomalies. In contrast, anomalous descent, which results in anomalous drying, is observed in the same months when the MJO migrates to the

eastern Pacific Ocean (120°W). Vertical motion in April over EA does not show statistically significant association with MJO indices at zero-lag in 1998-2012. However, in the 1979-2012 time period, consistent with the OLR anomalies, strong significant anomalies in vertical motion are observed in all months except in October. Similar pattern to the composites using CPC MJO index at 80^0 E are found employing RMM phase 3 index (Figure 3.9). For all other months vertical motion anomalies in the 1998-2012 time period are consistent with the 1979-2012 results.

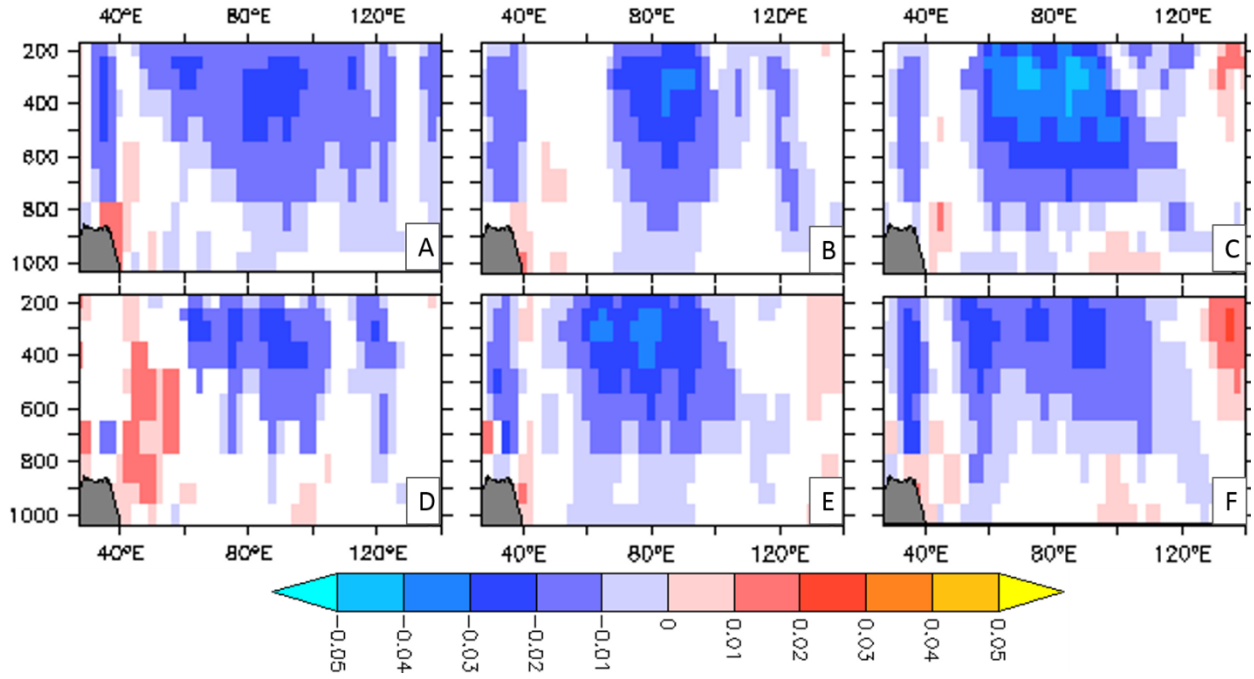

Figure 3.9. Composites of vertical velocity (pa s^{-1}) based on RMM phase 3 for 1979-2012. (A) March, (B) April, (C) May, (D) October, (E) November and (F) December. Shading shows results significant at the 90% confidence level.

In October, OLR and vertical velocity anomalies associated with MJO activity at 80°E and 120°W are very weak, but there are strong OLR associations with MJO indices at 120°E and 10°W

(Figures 3.10A, 3.10B). This is consistent with the precipitation results (Figure 3.5A, D): when MJO convective activity is centered at 120°E, positive OLR anomalies and negative rainfall anomalies are observed in the western Indian Ocean and coastal EA (Figure 3.10A). When MJO convective activity moves to 10°W, negative OLR anomalies and wet anomalies are observed over the western Indian Ocean and the coastal EA region (Figure 3.10B). These OLR anomalies are accompanied by anomalies in vertical motion: enhanced subsidence when the MJO is centered at 120°E and a tendency towards rising motion—which is sometimes actual rising motion and sometimes weakening of prevailing subsidence—when the MJO is centered at 10°W (Figure 3.10 C, D). MJO activity at 120°E is also associated with warm SST and low SLP over the Maritime Continent and cool SST in the west Equatorial Indian Ocean (Figure 3.10E, F, G). The opposite holds when MJO convection moves to 10°W. The SST pattern in Figures 3.10E and F is consistent with previous studies finding that positive (negative) SST anomalies tend to lead the maximum (minimum) in MJO convection by about two pentads (e.g., Lavender and Matthews 2009). As indicated in those previous studies, the two pentad lead SST anomalies associated with MJO convection result from the impact that the MJO convective center has on the ocean surface radiation and energy balances. In this sense the SST pattern observed here is an MJO response, but it is a direct response to the propagation of the MJO primary center of convection that does not depend on communication between the Indian Ocean MJO center of convection and East Africa.

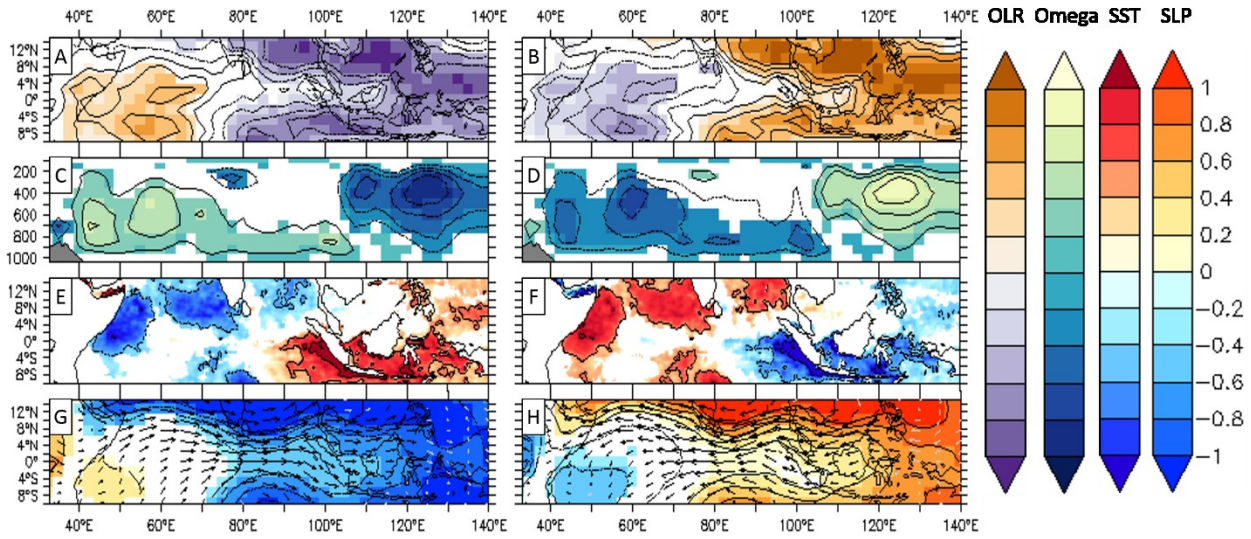

Figure 3.10. Composites of (A, B) OLR (40 W m^{-2}), (C, D) Omega (0.05 Pa s^{-1}), (E, F) SST (1.25 C°), (G, H) SLP (0.67 hPa) and wind (m s^{-1}) in October based on MJO indices at 120°E (A, C, E, G) and 10°W (B, D, F, H). Shading shows results significant at the 90% confidence level. Black vectors indicate that wind anomalies are significantly different from zero at the 90% confidence level in at least one of the wind components (meridional or zonal). SST composites are for 1982-2012, while all the rest are for 1979-2012.

The results shown in all panels in Figure 3.10 are consistent with anomalies in the zonal Walker circulation in the Indian Ocean. In October, when MJO activity is greatest at 120°E, there is a strengthened Walker cell across the Indian Ocean that enforces subsidence over the western Indian Ocean and coastal EA. When the MJO is centered at 10°W, there is a reversed or weakened Walker cell that leads to actual/anomalous upward motion in EA and downward motion in the Maritime Continent. This association is not observed in the other months of the short rains. We note that the MJO influence on the Walker Cell bears some resemblance to known Indian Ocean Dipole index (IOD) associations with the Walker Cell and EA precipitation (Saji et al. 1999). The MJO

association, however, occurs on shorter time scales than IOD variability and has an SST pattern (Figures 3.10E&F) that are spatially more extensive than the classic IOD signal (Saji et al. 1999).

The strength of OLR, vertical motion, and large scale atmospheric circulation anomalies associated with MJO-mediated precipitation variability in coastal EA in October contrasts with the findings of PC06a, who found only weak OLR associations with MJO-mediated precipitation variability in the coastal region. The difference could be due to differences in data set or period of analysis. In either event, our result suggests that MJO influence on coastal EA precipitation is due to deep convective processes influenced by variability in a Walker Circulation over the Indian Ocean, and cannot be attributed solely to shallow convection or stratiform precipitation, which were the primary mechanisms identified by PC06a. The Walker Circulation association is also observed when composites are averaged over the entire short rainy season, but this seasonal result derives from the strong association in October.

Intraseasonal precipitation variability during the EA long rains has also been linked to variability in the strength of near-surface and mid-level westerly wind anomalies (Camberlin and Wairoto 1997; Okoola 1999; Camberlin and Okoola 2003, among others). The most frequently cited mechanistic link between westerlies and EA precipitation is that these winds have the potential to transport moisture from the Atlantic Ocean and Congo basin into the region (Nicholson 1996). PC06a found that anomalies in low-level zonal winds are associated with MJO, and our analysis confirms this finding. During the long rains, strong low to mid-level westerly anomalies are associated with MJO convection at 80°E and the opposite is seen for MJO convection at 120°W (Figure 3.11; compare to precipitation and OLR in Figures 3.3 and 3.5). This pattern is clear for

both CPC and RMM index (Figure 3.12) composites, and it is similar for both the 1979-2012 and 1998-2012 time periods (with the exception of the previously noted lack of significance in April for the 1998-2012 period). We observe a similar pattern in the short rainy season. The anomalies do not, however, necessarily represent actual wind reversals. Analyses of daily low-level winds indicate that even when MJO convection is strong at 80°E very few incursions of humid and unstable westerlies from the Congo basin occur during the long rains; the anomaly is simply a weakening of prevailing easterly winds. This suggests that near-surface westerly wind anomalies influence long rainy season EA precipitation primarily because they represent a weakening of easterly winds (mechanisms discussed below), and not because of actual incursion of humid air from the Congo basin. In November and even more frequently in December westerly wind anomalies are, in fact, associated with wind reversals and with the incursion of westerly winds into EA.

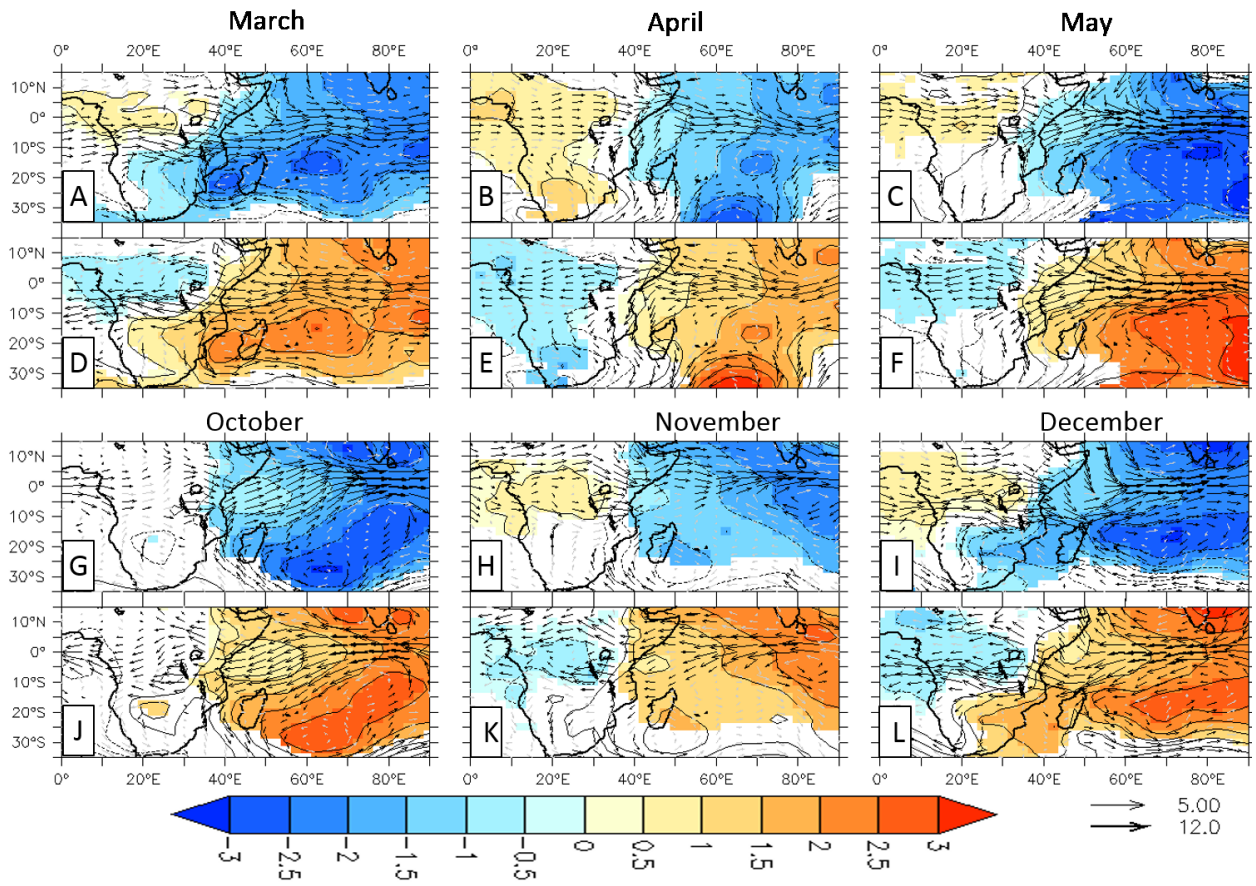

Figure 3.11. Composites of SLP (hPa) and wind at 850 hPa (m s^{-1}) based on MJO indices 80°E (A-C, G-I) and 120°W (D-F, J-L) for 1979-2012. (A, D) March, (B, E) April, (C, F) May, (G, J) October, (H, K) November and (I, L) December. Shading shows results significant at the 90% confidence level. Black vectors indicate that wind anomalies are significantly different from zero at the 90% confidence level in at least one of the wind components (meridional or zonal).

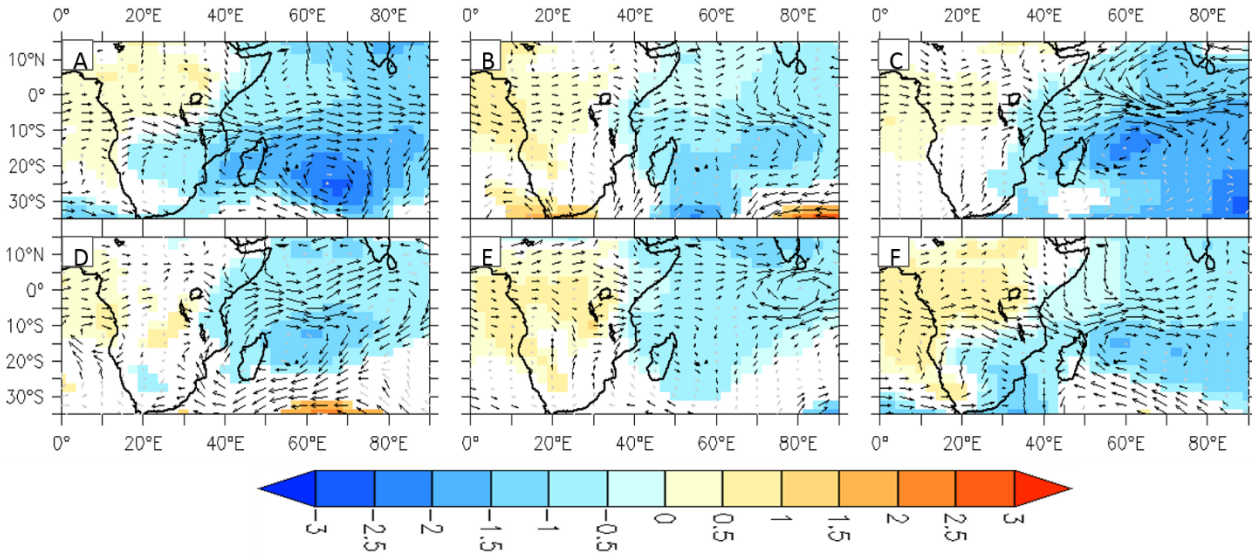

Figure 3.12. Composites of SLP (hPa) and wind at 850 hPa (m s^{-1}) based on RMM phase 3 for 1979-2012. (A) March, (B) April, (C) May, (D) October, (E) November and (F) December. Shading shows results significant at the 90% confidence level. Black vectors indicate that wind anomalies are significantly different from zero at the 90% confidence level in at least one of the wind components (meridional or zonal).

During both the long and short rains, these MJO-associated westerly wind anomalies are a product of SLP variations in the Indian Ocean. When MJO convection is centered on the Indian Ocean (80°E), a negative SLP anomaly produces a pressure gradient that weakens the easterlies and enhances westerly flow over the African continent, and the opposite holds when convection is suppressed in the Indian Ocean (Figure 11). Similar to the SLP composites using the 80^0 E CPC index is found using RMM phase 3 (Figure 12). This link between Indian Ocean SLP and both winds and precipitation over EA is consistent with previous studies (PC06a, PC06b, Black et al. 2003, Goddard and Graham 1999).

3.3.b. Mechanisms of precipitation variability

The strong precipitation, OLR, and low-level wind anomalies described above are consistent with multiple potential mechanisms of MJO influence. Enhanced westerlies, for example, could enhance precipitation in EA through increased moisture flux to the region, stronger low level convergence, and/or reduced stability in the lower troposphere. MJO-induced differences in Indian Ocean convection, meanwhile, impact lower-tropospheric air temperature over the Indian Ocean and the potential for both moisture advection and energy advection into EA from the east. Our analysis suggests that multiple mechanisms are active, and that the relative importance of these mechanisms differs between the long and short rains and between the interior highlands and the coast.

Focusing on the mechanisms that are most evident in MJO-based composites, we observe that low-level moisture flux divergence is strongly influenced by MJO activity during the short rains (Figure 3.13). The sign of the divergence composites is consistent with precipitation anomalies—negative divergence (i.e., convergence) is observed when MJO activity is centered in the Indian Ocean, westerly wind anomalies are enhanced (Figures 3.11 & 3.12), and the EA precipitation anomaly is positive. This indicates that a mechanism of moisture convergence leading to enhanced convection is potentially quite important in the short rains. The divergence composites are present in the long rains as well, but are somewhat less pronounced.

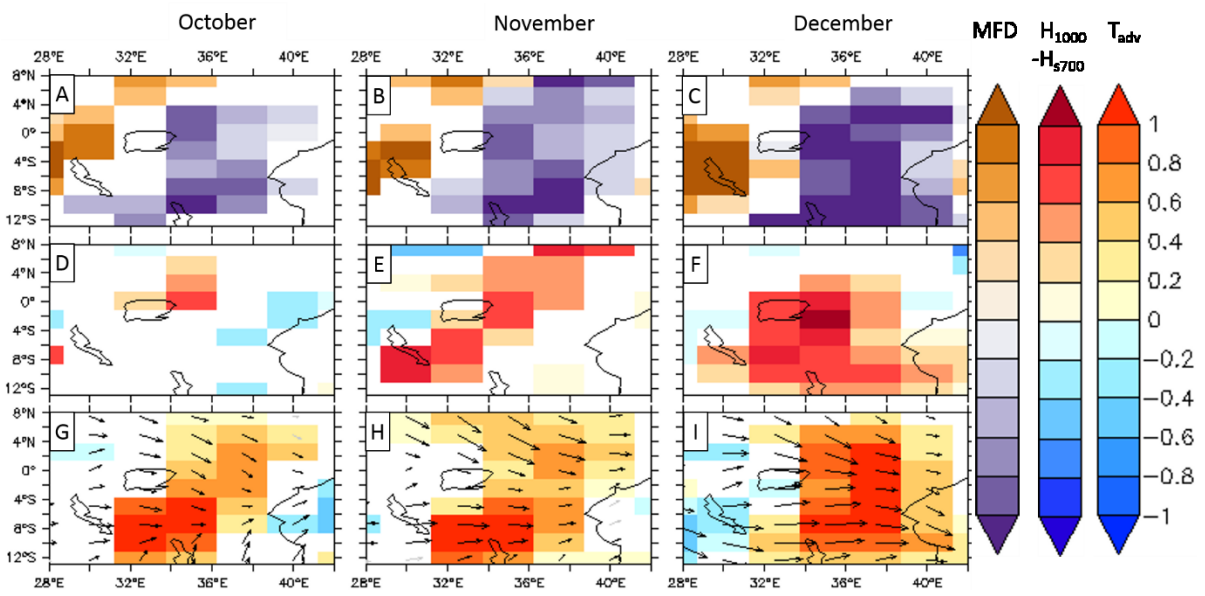

Figure 3.13. Composites of (A-C) MFD ($1/3 \times 10^{-7}$ s^{-1}), (D- F) buoyancy due to MSE profile ($H_{1000} - Hs_{700}$; 8×10^{3} J kg^{-1}), (G-I) Tadv (2×10^{-5} C° s^{-1}) and wind at 850 hPa (m s^{-1}) for the short rains for 1979-2012. (A, D, G) October, (B, E, H) November, (C, F, I) December. The composites are based on MJO at 80°E. Shading shows results significant at the 90% confidence level. Black vectors indicate that wind anomalies are significantly different from zero at the 90% confidence level in at least one of the wind components (meridional or zonal).

For Figure 3.13 and 3.14, we show only composites for 80°E; composites for MJO centered at 120°W are approximately equal and opposite to the 80°E composites in all cases. Additionally, for April we have replaced the 80°E zero-lag composites with two pentad lead time composites on the MJO index at 10°W. As explained previously, the two pentad lead MJO activity at 10°W shows stronger correlation with EA precipitation in April than any zero-lag MJO index (Figure 3.2) in the 1998-2012 time period.

Lower atmosphere moist static instability anomalies associated with MJO activity are pronounced in EA in the long rains and middle and late short rains (November and December) ($H_{1000} - Hs_{700}$; Figures 3.13 and 3.14). This is consistent with a mechanism in which anomalously warm, wet winds enter the region from the Indian Ocean—MJO convection in the Indian Ocean warming the lower troposphere (not shown)—and the slowing of winds allows for further local heating of the lower atmosphere. The resulting warm, moist air mass is primed for convective precipitation events.

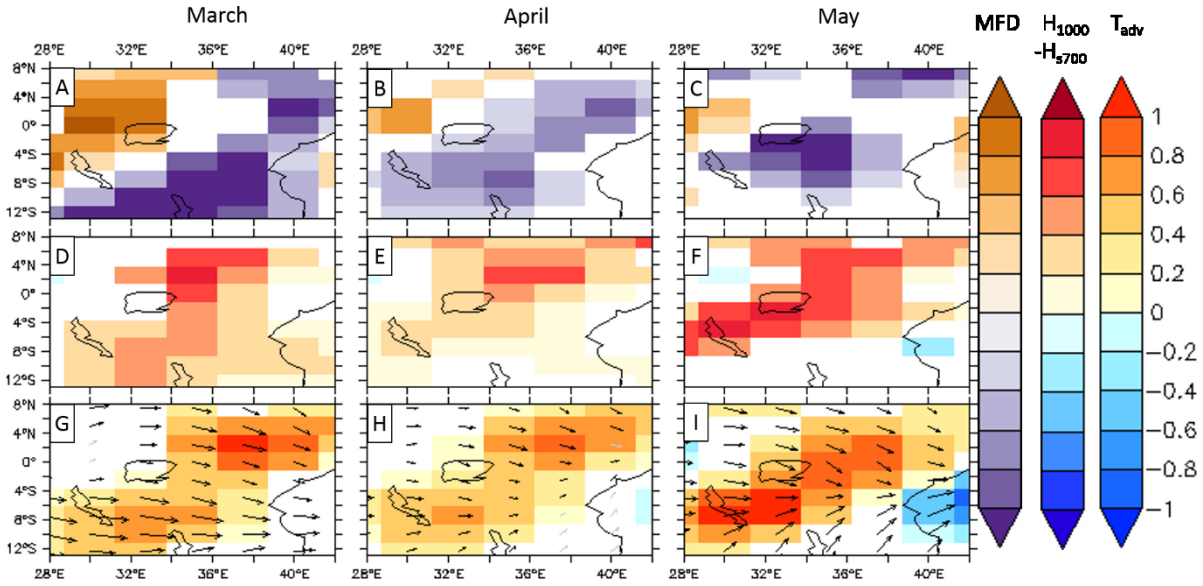

Figure 3.14. Composites of (A- C) MFD ($1/3 \times 10^{-7}$ s^{-1}), (D-F) buoyancy due to MSE profile ($H_{1000} - Hs_{700}$; 8×10^{3} J kg^{-1}), (G- I) Tadv (2×10^{-5} C° s^{-1}) and wind at 850 hPa (m s^{-1}) for the long rains for 1979-2012. (A, D, G) March, (B, E, H) April, (C, F, I) May. The composites are based on MJO at 80°E for March and May and MJO at 10°W at two pentads lead for April. Shading shows results significant at the 90% confidence level. Black vectors indicate that wind anomalies are significantly different from zero at the 90% confidence level in at least one of the wind components (meridional or zonal).

Indeed, analysis of the thermodynamic balance confirms this link. Figures 3.13G-I and 3.14G-I show the advective component of the lower atmosphere thermodynamic balance. In all months of both the short and long rainy seasons there is a significant association between MJO activity in the Indian Ocean and temperature advection into EA: enhanced MJO activity at 80°E (or, for April, 10°W) is associated with higher near-surface air temperature over the Indian Ocean, which is carried into EA on low level easterly winds, and the opposite occurs when MJO activity is centered at 120°W. Even though low level winds entering the region are anomalously slow when MJO convection is in the Indian Ocean (see the wind anomaly vectors in Figure 3.11 and 3.12), the warmer near-surface air temperatures over the Indian Ocean result in more energy advection into the region, contributing to instability and to moisture convergence. Analysis using ERA-Interim data shows similar patterns of temperature advection. Analysis of temperature advection, moisture flux divergence and buoyancy using RMM phase 3 index gives similar, but weaker, results (Figures 3.15-3.17).

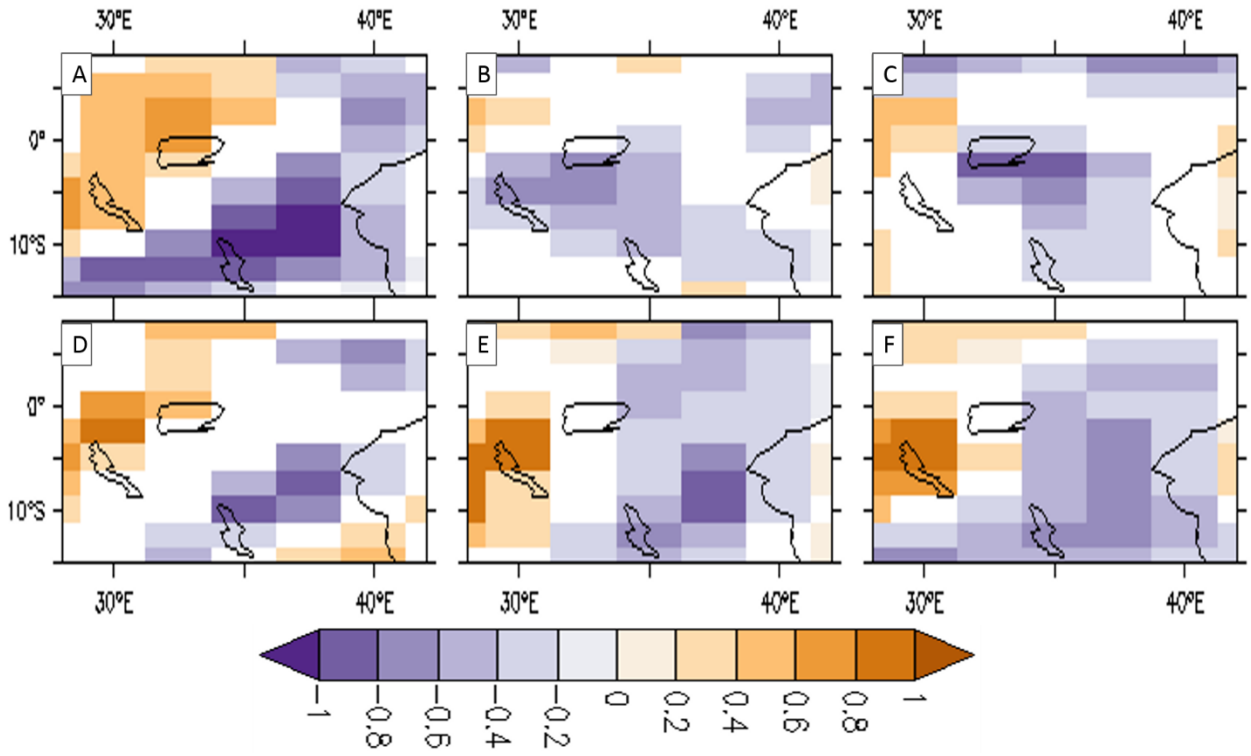

Figure 3.15. Composites of moisture flux divergence ($1/3*10^{-7}$) based on RMM phase 3 for 1979-2012. (A) March, (B) April, (C) May, (D) October, (E) November and (F) December. Shading shows results significant at the 90% confidence level.

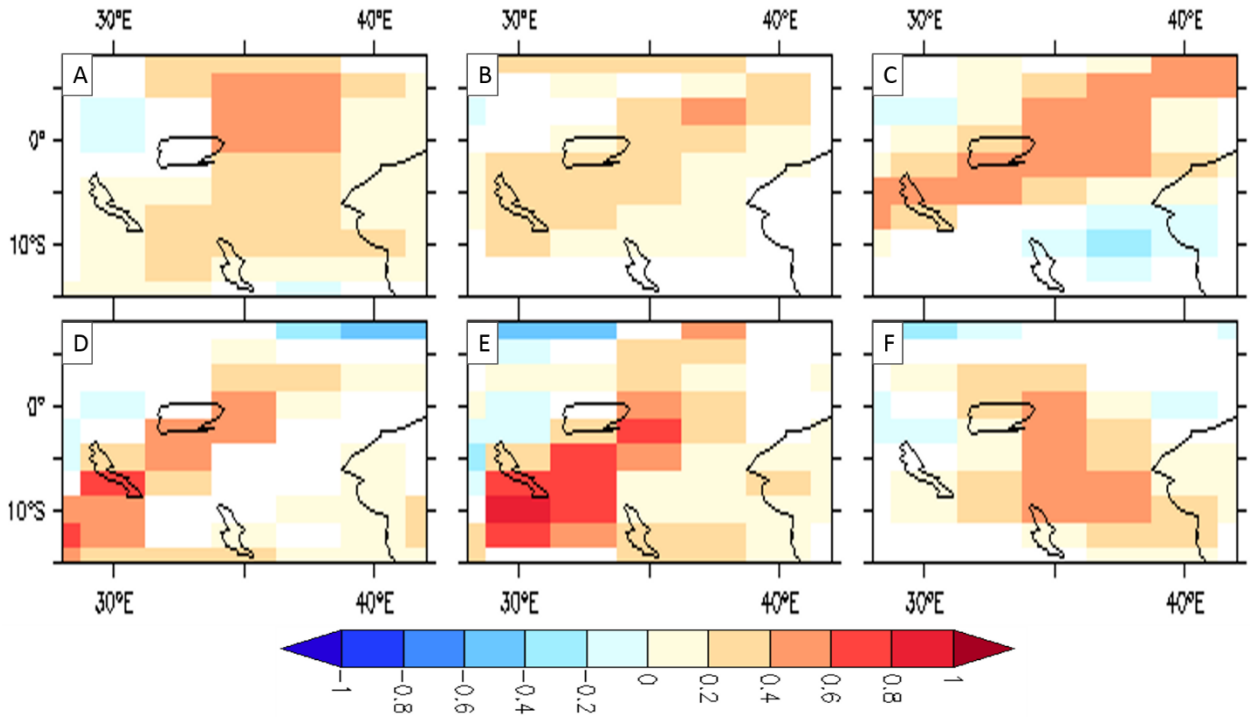

Figure 3.16. Composites of buoyancy due to MSE profile ($H_{1000} - Hs_{700}$; $8x10^3$ J kg^{-1}) based on RMM phase 3 for 1979-2012. (A) March, (B) April, (C) May, (D) October, (E) November and (F) December. Shading shows results significant at the 90% confidence level.

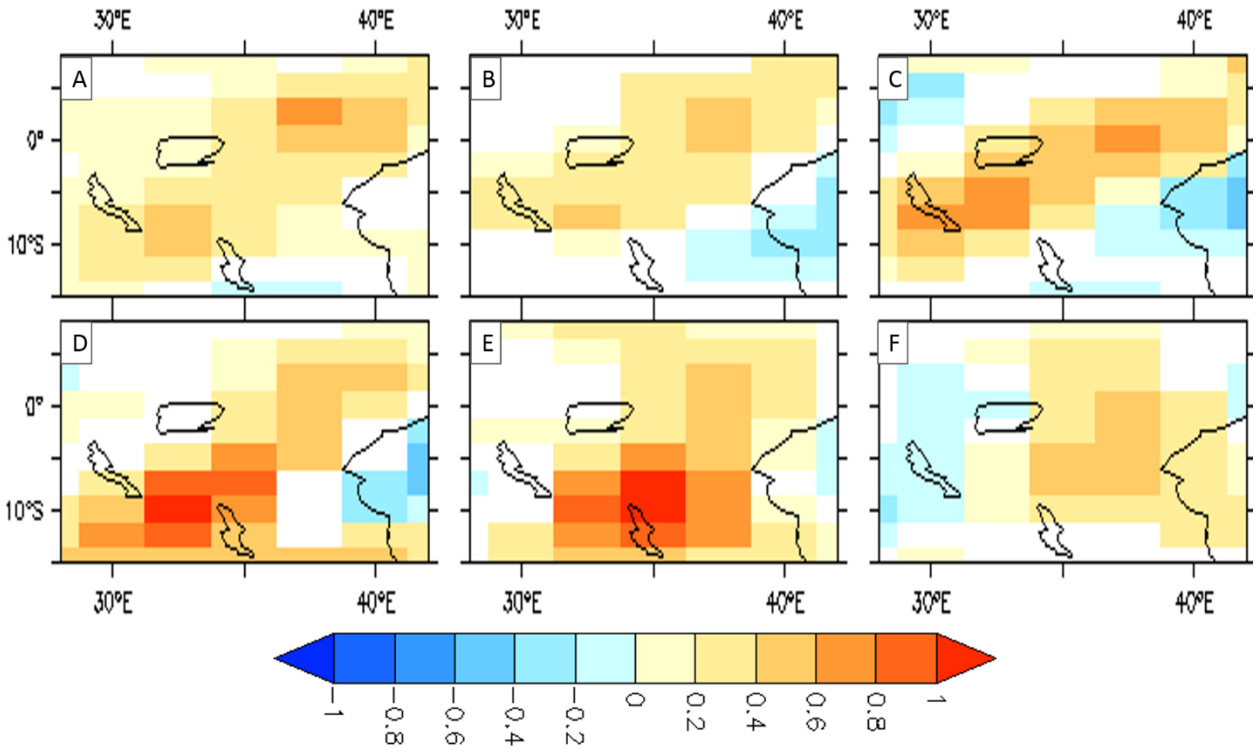

Figure 3.17. Composites of Tadv ($2x10^{-5}$ C° s^{-1}) based on RMM phase 3 for 1979-2012. (A) March, (B) April, (C) May, (D) October, (E) November and (F) December. Shading shows results significant at the 90% confidence level.

The MJO influence on coastal EA precipitation in October is distinct from the mechanisms that link MJO to the highlands. In this month, temperature and vertical motion anomalies in the Indian Ocean that occur when MJO convection is centered on 120°E are associated with strengthening of the zonal Walker circulation while MJO convection at 10°W is associated with weakening and even reversal of that circulation (Figure 3.10). The impact of this large scale strengthening and weakening/reversal of the Walker circulation extends just to the edge of EA, such that the precipitation effects are felt on the coast but not in the interior highlands. The strengthening (weakening or reversal) of the Walker circulation when MJO is centered at 120°E (10°W) is also

associated with stronger (weaker) near-surface winds along the coast of EA sometimes referred to as the Somali Low Level Jet (SLLJ). A strengthening of the SLLJ has been associated with enhanced frictionally-induced subsidence on the EA coast (Nicholson 1996). However, the depth and extent of the subsidence feature suggest that frictionally-induced subsidence is not the sole explanation for MJO-associated precipitation effects in these phases. Similar results are found when ERA-Interim data are used.

The mechanisms of MJO influence on the long rains, short rains, and coastal rains in October are summarized in Figure 3.18. The thermodynamic mechanism of influence appears to operate throughout the long rains and short rains. The dynamic, convergence-mediated mechanism is strong and widespread throughout the short rains. It is also strong in the long rains, especially in March and April. The October coastal mechanism of influence is distinct and is associated with the strengthening, reversal or weakening of the Walker cell in the Indian Ocean.

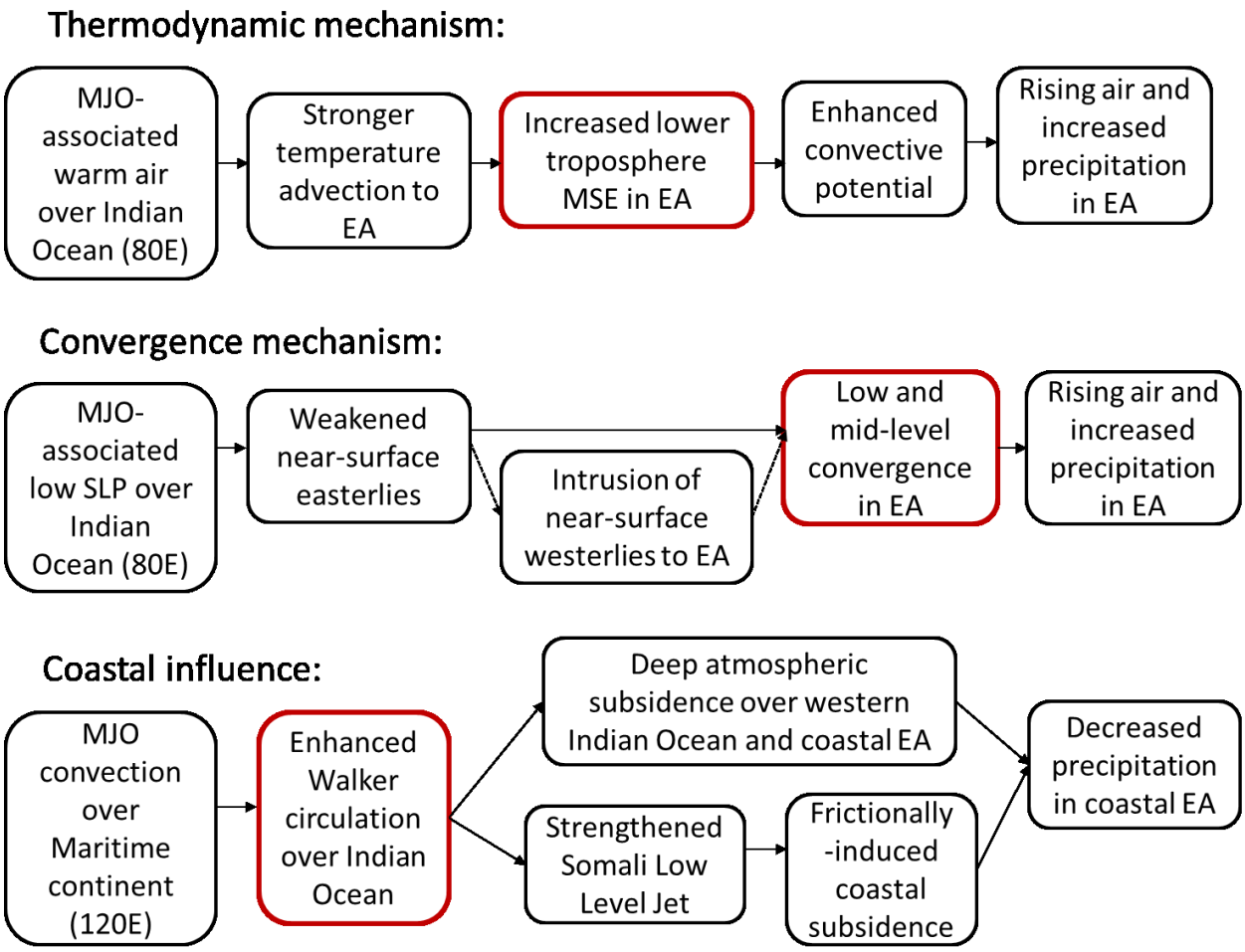

Figure 3.18. Mechanisms of MJO influence on East African precipitation.

3.3.c. Stability of associations

PC06b found that the strength of association between MJO and their study region in EA varied considerably on an interannual basis: the common variance between MJO and their smoothed rainfall timeseries varied from 5% to 53% on an annual basis for their period of analysis. Similarly, the influence of MJO on EA might change over longer time periods due to evolving characteristics of MJO itself or due to changes in the strength of its connection to EA. To evaluate the stationarity of MJO influence on EA we compare results for the periods 1979-1997, 1998-2012 and 1979-2012. Overall, we find a consistent pattern for each of these time periods, but there are some

differences in monthly scale associations. As noted previously, April stands out as a month in which concurrent associations between MJO indices at 80°E and 120°W and mechanisms influencing EA precipitation are difficult to detect in the 1998-2012 period. These associations are much clearer for 1979-2012 (Figures 3.6-3.9, 3.11 & 3.12), and they are also clear for 1979-1997 (not shown).

In addition to April, minor shifts in the significance of MJO associations are found in November—in which statistical associations are weaker for 1979-1997 than they are for 1979-2012 or for 1998-2012—and May, in which OLR results are weaker for 1979-1997 than for the other time periods, even though dynamic and thermodynamic composites are consistent with a significant MJO influence in all three periods. For coast East Africa, the associations between precipitation and MJO indices at 120^0 E and 10^0 W are consistent for 1979-1997, 1998-2012, and 1979-2012.

Overall, these analyses of different time periods suggest that the influence of MJO on EA has shifted somewhat between the 1979-1997 and 1998-2012 period, and that this shift has altered the statistical association between standard MJO indices and EA precipitation variability. Nevertheless, the general patterns and mechanisms of association are consistent across time periods. This indicates that MJO has been an important influence on EA precipitation since at least 1979.

3.3.d. Potential for prediction

As shown in Figures 3.2 and 3.19, the CPC MJO indices are significantly correlated with EA precipitation at various lead times. For April, for example, at two pentads lead, we see correlations

of 0.58 with MJO index at 10°W and -0.59 with MJO index at 120°E (Figures 3.2, 3.19). These correlations are both strong and widespread across the EA highlands. Significant correlations (0.41 and -0.40 with MJO indices at 160°E and 20°E, respectively) are also found in April at four pentads lead.

Various studies have developed statistical and/or dynamical prediction models of the MJO with skills extending to about 25 days and beyond (e.g., Waliser et al. 2003, Maharaj and Wheeler 2005; Vitart et al. 2007, Jiang et al. 2008; Lin et al. 2008, Love et al. 2008, Love et al. 2008; Seo 2009; Seo et al. 2009; Kang and Kim 2010; Rashid et al. 2011). Waliser et al. (2003), for example, find that in the Eastern Hemisphere useful predictability of the MJO extends out to about 25 -30 days for 200-hPa velocity potential. Employing a dynamical prediction system, Rashid et al. (2011) document that the MJO can be predicted to about 21 days.

Insomuch as MJO variability can be predicted with reasonable skill on a time horizon of up to one month, the lead-time correlations presented in Figure 3.19 suggest that predictions of the variability and volume of rains in April, which is the main rainy month in the study region, could be usefully attempted up to two months in advance. In other months, correlations at somewhat shorter lead times could be used to predict intraseasonal variability on the order of one month to six weeks in advance. In April and May the two pentad lead correlations are promising, while in November, December and March correlations are stronger at zero to one pentad lead. Employing the MJO indices in forecast models can help to minimize difficulties in the predictions of the long rains characteristics (Semazzi et al. 1996; Okoola 1998; Indeje et al. 2000; Camberlin et al. 2009) and to mitigate impacts of weather extremes by mobilizing resources in appropriate time.

	Simultaneous		One pentad lead		Two pentad lead		Three pentad lead		Four pentad lead	
Oct.	0.40	-0.38	0.41	-0.40	0.31					
Nov.	0.54	-0.53	0.48	-0.47	0.35	-0.36	0.34	-0.34		
Dec.	0.53	-0.54	0.45	-0.45						
Mar.	0.47	-0.46	0.48	-0.51	0.35					
Apr.	0.33	-0.33	0.53	-0.50	0.58	-0.59	0.49	-0.48	0.41	-0.40
May	0.60	-0.56	0.56	-0.52	0.47	-0.46	0.32	-0.32		

Figure 3.19. Correlations of area average precipitation over EA, for 1998-2012, with the various MJO indices at various lead times that are significant at the 90% confidence level using the reduced degrees of freedom due to autocorrelation. At a given pentad lead, the highest negative and positive correlations are provided. Regions used for each month are 34°-38°E and 12°-2°S for March, 30°-38°E and 6°S-5°N for April and May, 30°-38°E and 2°S-8°N for October, 32°-38°E, 4°S-4°N for November and 32°-38°E and 10°S-2°N for December.

3.4 Conclusions

The livelihood of millions of people in EA is critically affected by frequent droughts and floods that retard progress toward Millennium Development goals. From the perspective of floods, flash droughts, and crop production, understanding variability on intraseasonal timescales is vital to

develop weather and short-term climate forecasting tools to mitigate impacts of departures from normal weather in the region.

Numerous studies have noted the low temporal coherence of precipitation in EA and have urged for further study of precipitation variability at sub-seasonal timescales (e.g., Camberlin and Philippon 2002; Zorita and Tilya 2002, Camberlin and Okoola 2003). This study examined the associations of precipitation and MJO, using the CPC and RMM MJO indices, in EA for each calendar month separately employing pentad and daily data. The region of MJO influence in EA varies within each rainy season, as the ITCZ moves through the region. The magnitude of MJO influence also varies from month to month. During the long rains, the influence is somewhat greater in the late season (May) than the early season (March), while the middle of the season (April) shows no statistically significant association with synchronous CPC MJO indices. This apparent "pause" in MJO influence in April, however, seems to be a product of modest nonstationarities in MJO that make it difficult to characterize associations across all months and time periods using standard static MJO index systems: we do find lead-time associations between April precipitation and MJO indices that are consistent with proposed MJO mechanisms of influence, and statistical relationships at zero-lag are significant in April when we consider other time periods. During the short rains, the MJO modulation of EA highland precipitation is significant in November and December. In October the MJO influence on highland EA is modest, but strong associations between MJO and precipitation in the coastal regions of EA are observed.

The results show that anomalous wetness is experienced when the MJO convective center is between 20°E and 120°E and dry anomalies prevail when the MJO is located in the region from

160°E and 10°W. Maximum correlations between the MJO strength and precipitation over EA are observed using 70°/80°E and 120°W MJO indices. When the MJO convective envelope is located at 70°/80°E (120°W), negative (positive) SLP anomalies over the Indian Ocean are observed which result in westerly (easterly) anomalies in low and mid-troposphere winds. In the short rains, when the MJO is centered in the western Indian Ocean, the Congo Air boundary (CAB) moves east and brings moist, unstable air to EA resulting in increased convective activity. In contrast, when the MJO moves to the eastern Pacific, the CAB moves far west and cold and dry easterlies prevail over EA.

Low level easterly winds in the western Indian Ocean are weaker when the MJO is centered in the western Indian Ocean, but they are anomalously warm and advect significant moisture and temperature to the EA. However, as the MJO moves to the eastern Pacific Ocean, the easterlies become stronger, dry, cold and divergent. In November and December there is strong evidence for both a dynamic precipitation influence due to lower atmosphere convergence and a thermodynamic mechanism due to temperature advection and lower atmosphere instability. Both mechanisms are also potentially active in the long rainy season. In October a completely distinct mechanism of influence is evident in the coastal region, as MJO-mediated precipitation variability is associated with the strengthening and reversal or weakening of the Walker cell in the Indian Ocean. The fact that the MJO influence on EA depends on a diverse set of large scale and synoptic scale mechanisms is relevant to studies of subseasonal precipitation variability in a changing climate. Changes in either the MJO or in background humidity and winds affecting EA have the potential to modify each of these mechanisms in different ways. A robust understanding of climate change impacts on the region, then, must include an appreciation for how various mechanisms of MJO influence might evolve in a nonstationary climate.

Another potentially useful result of this analysis is the finding that precipitation over EA exhibits significant correlations with the MJO indices at reasonable lead times. Therefore, since the MJO position and strength can be predicted with skill up to a month in advance, a combination of MJO prediction and the statistical associations explored in this paper could be applied to predict rainfall anomalies in EA at time scales between long-range weather forecasts and short-term seasonal predictions.

4. Chapter 4: The Madden-Julian Oscillation's influence on Spring Rainy Season Precipitation over Equatorial West Africa[3]

Abstract

This paper characterizes the influence of the Madden-Julian Oscillation (MJO) on spring rainy season (March-June) convection variability over Equatorial West Africa (EWA) and investigates mechanisms of association. It is found that the MJO has a significant impact on convection and precipitation anomalies over the region. Over large portions of EWA, MJO impacts on rainfall constitute a difference on the order of 20-50% from average daily rain rates for the season. This impact is primarily due to the direct influence of the eastward movement of the MJO convective core into EWA, which is associated with westerly low-level wind anomalies that advect moisture from the Atlantic Ocean to the region. In addition, equatorial Rossby and Kelvin waves triggered by MJO convection anomalies over the Indian Ocean have a significant and systematic influence on EWA spring rainy season precipitation. The Kelvin wave contribution and the relative strength of the direct MJO convective influence compared to that of equatorial wave activity differs from findings of studies that have examined MJO influence on EWA during boreal summer. In addition, MJO is found to influence precipitation extremes during spring rains in a manner that is not

[3] Berhane, F., and B. Zaitchik, under review: The Madden-Julian Oscillation's influence on Spring Precipitation over Equatorial West Africa. *Journal of Climate*.

observed in summer. Importantly, in our analysis the influences of MJO convection and each of the MJO-associated convectively coupled equatorial waves frequently coincide, reaching EWA approximately twenty days after MJO convection initiates in the Indian Ocean. This coincident timing enhances the total MJO impact on the region, and it also implies that MJO events have potential for prediction of regional-scale convection and rainfall anomalies over EWA in this season.

Key words: Madden-Julian Oscillation, Kelvin waves, Rossby waves, West Africa, intraseasonal variability, Equatorial West Africa

4.1. Introduction

The Madden-Julian Oscillation (MJO; Madden and Julian 1971a 1972b) is the strongest driver of intraseasonal precipitation variability in the tropics (Madden and Julian 1994). The oscillation is a planetary-scale, baroclinic disturbance trapped around the equator (Ventrice et al. 2013) that has a period between 30 and 60 days (Schreck et al. 2013). It appears as an eastward propagating large-scale anomaly in convection, zonal winds, and upper level velocity potential (Hendon and Salby 1994). The MJO's convective signal, which propagates at about 5 m s^{-1} (Zhang 2005), is focused on the Eastern Hemisphere tropics (Madden and Julian 1971a 1972b); however, its circulation signal affects the global tropics (Hendon and Salby 1994). These impacts vary by region and season, and are stronger in boreal winter than in boreal summer (Wang and Rui 1990; Hendon and Salby 1994).

The nature of MJO impacts on local precipitation have been documented in many regions (e.g., Barlow and Salstein 2006; Hidayat and Kizu 2010; Pai et al. 2011; among many others). For

Africa, previous studies have focused on regionally distinct areas such as the highlands and coastal regions of Eastern Africa (Pohl and Camberlin, 200a, 200b; Berhane and Zaitchik 2014), West Africa (Matthews 2004; Maloney and Shaman 2008; Gu 2009; Janicot et al. 2009; Lavender and Matthews 2009; Mohino et al. 2012) and southern Africa (Pohl et al. 2007). These studies have shown that the mechanisms of MJO influence differ by region and season. Convective variability over the West African monsoon region, for example, is modulated by the migration of the MJO convective center and by Rossby waves excited by MJO anomalies over the Indo-Pacific region (Janicot et al. 2009; Lavender and Matthews 2009; Mohino et al. 2012). In the highlands of East Africa, on the other hand, the MJO influences precipitation variability by modulating temperature advection to the region from the Indian Ocean, and by modifying stability of the lower troposphere and convergence of near-surface winds associated with MJO conditions over the Indian Ocean (Berhane and Zaitchik 2014).

Equatorial West Africa (EWA), like much of the global tropics (e.g., Gadgil 2003; Webster et al. 1998; Wheeler and McBride 2005), exhibits strong intraseasonal variability in precipitation. This variability has significant impacts on rainfed agriculture, food and water security, and human health (Gadgil and Rao 2000; Sultan et al. 2005; Verdin et al. 2005), affecting the lives of millions of people. But while several studies have examined general aspects of precipitation in the region (e.g., Nguyen and Duvel 2008; Jackson et al. 2009; Dezfuli and Nicholson 2012; Nicholson and Dezfuli 2013), relatively few have focused on intra-seasonal variability or on the potential influence of the MJO. Of the studies that have considered MJO influence on the region (e.g., Matthews 2004; Maloney and Shaman 2008; Janicot et al. 2009; Lavender and Matthews 2009; Mohino et al. 2012), all but one (Gu 2009) have focused exclusively on boreal summer. The

findings of Gu (2009), however, show that region-wide anomalies in convection and precipitation occur during the passage of intraseasonal convective signals associated with the MJO, suggesting that further study of MJO influence during spring is warranted.

The spring rainy season accounts for up to 45% of annual precipitation in portions of EWA and is a vital cropping season in much of the region. It is also subject to significant inter-annual variability in total precipitation (Eugène et al. 2012) and to variability in the onset and cessation of rains (Odekunle 2004; Odekunle et al. 2005). This variability has large impacts on the livelihoods and socio-economic activities across the region (Eugène et al. 2012).

Recognizing the importance of this season, we present a detailed investigation of MJO mechanisms of influence during the spring rains as compared to influence during boreal summer rains. The analysis builds on the work presented by Gu (2009) by including a robust wavenumber-frequency spectral analysis that allows us to distinguish between MJO influences attributable to the direct eastward propagation of the MJO convective center to the region and those attributable to Kelvin and Rossby waves triggered by the MJO in the Indian Ocean. In addition, we perform MJO analyses in a consistent manner for the spring and boreal summer rainy seasons in order to compare mechanisms of MJO influence across these two seasons. The comparisons are useful for understanding fundamental processes of MJO influence in EWA and contribute to the scientific basis for long-range weather forecasts in both seasons. Finally, we examine the influence that MJO has on precipitation extremes across the region.

4.2. Data and Methods

4.2.a. Data

A number of indexing systems have been used to quantify MJO activity. Here we consider several different indices in order to verify the robustness of identified associations with EWA precipitation. These are:

1. Real-Time Multivariate MJO Index (RMM): a combined measure of convection and circulation. It is calculated as the principal component (PC) time series of the two leading empirical orthogonal functions (EOFs) of combined daily mean fields of 850-hPa and 200-hPa zonal winds and OLR averaged over the tropics (Wheeler and Hendon 2004; hereafter WH04). In order to view the spatial and temporal evolution of the MJO, WH04 developed a two-dimensional phase-space diagram. In this phase-space diagram, strong MJO events move in a large counter-clockwise direction around the origin. In contrast, weak MJO variability usually appears as random movement near the origin of the phase-space diagram. RMM indices are available at http://cawcr.gov.au/staff/mwheeler/maproom/RMM/index.htm.
2. OLR MJO index (OMI): a univariate index calculated by projecting 20-96 day filtered OLR onto the daily spatial EOF patterns of 30-96 day filtered OLR (Kiladis et al. 2013). The 20-96 day filtered OLR comprises all eastward and westward wave numbers while the 30-96 day filtered OLR consists of the eastward wave numbers only (Kiladis et al. 2013).
3. Velocity Potential MJO index (VPM): developed in the same way as WH04 except using 200 hPa Velocity Potential (VP200) instead of OLR (Ventrice et al. 2013). Both OMI and VPM indices can be accessed from http://www.esrl.noaa.gov/psd/mjo/mjoindex/.

All three of these indexing systems categorize the eastward propagation of the MJO into eight phases, with each phase corresponding to the geographical position of the active convective center

of the MJO (see, for example, WH04 Figure 7). Generally, the MJO lasts for about 6 days in each phase. In all three systems the phases correspond to periods when the center of MJO convective activity is over the Indian Ocean (phase 2 and 3), the maritime continent (phase 4 and 5), and the western Pacific Ocean (phase 6 and 7). In phase 8 and 1 the MJO circulation signal is in the Western Hemisphere and over Africa. The eight MJO Phases are categorized as "strong" when the amplitude of the MJO is greater than 1; otherwise the MJO is categorized as "weak" irrespective of the phase of the MJO.

In addition to these established indices, we calculate an MJO index derived specifically from OLR anomalies in the African domain, following a suggestion raised by the Climate Variability and Predictability MJO Working Group (Waliser et al. 2009) to employ a 20-100 day band pass filter with 201 weights in extracting intraseasonal variability associated with the MJO. We define this index as:

4. First principal component of the EOF of OLR over Africa (PC-EOF1): performed on the 20-100-day bandpass filtered March-June OLR values for the domain 30^0W-40^0E and 15^0S-25^0N (Figure 4.1B; results were not sensitive to moderate changes in the domain extents). The leading eigenvector from the empirical orthogonal function (EOF), which passes both scree (Cattell 1966) and North (North et al. 1982) tests, accounts for 18.5% of the variance and was well separated from second eigenvector, which accounts for 10.5% of the variance. The third eigenvector accounts for 7.6% of the variance. The PC of the second and third eigenvectors do not exhibit significant associations with the PC of the first eigenvector. Therefore, the second and third eigenvectors will not be considered further. The time series of the first principal component (PC-EOF1) has been used to investigate the evolution of the MJO impacts over the

study region in the spring rainy season. As we will show in the results section, positive PC-EOF1 corresponds to phase 1 of the other MJO indices considered in this study, whereas negative PC-EOF1 is phase 5. To compare the strength of the impacts of the MJO in the spring rainy season and in boreal summer, PC-EOF1 was calculated for JAS following the same procedure to the calculation of PC-EOF1 in MAMJ.

Gu (2009) use the principal component time series of the first EOF of 20-100-day filtered OLR anomalies centered over EWA to explore impacts of the MJO on convection and precipitation over EWA in the spring rainy season. We generate PC-EOF1 index in a similar way to that of Gu (2009). This index is used to investigate further the mechanisms in detail by breaking up the total MJO influence into direct eastward propagation of the MJO to the region, and into equatorial convectively coupled Kelvin and Rossby waves. Moreover, this index is used to assess influences of the MJO on rainfall distribution in the spring rainy season, and to compare and contrast the strengths of the MJO impacts on precipitation over EWA in the spring and summer rainy seasons.

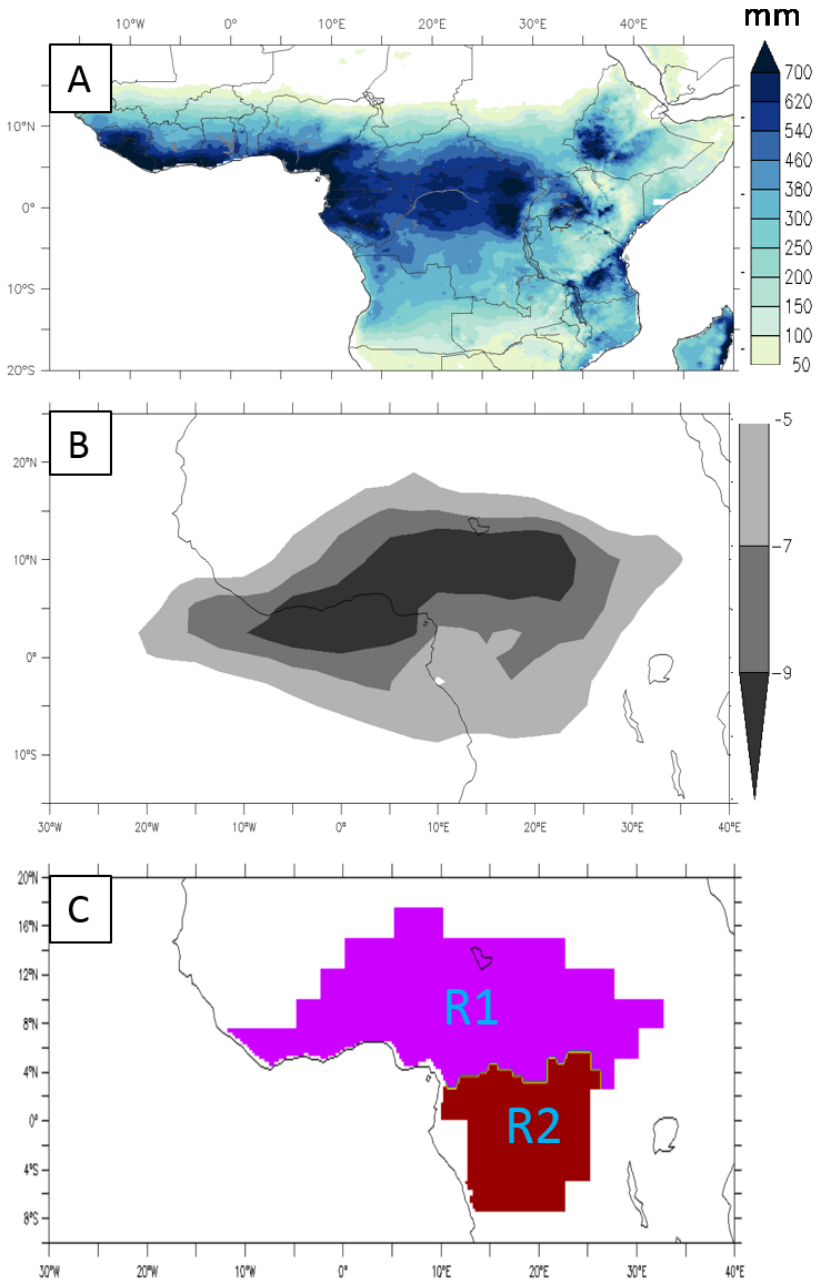

Figure 4.1. (A) Climatology of March-June precipitation (mm) from USGS Climate Hazard Group Infrared Precipitation with Station (CHIRPS) merged gauge and satellite product for the period 1981-2013. (B) Loading of the first EOF (W m^{-2}) of 20–100-day bandpass filtered OLR centered over West Africa (15^0S–25^0N, 30^0W–40^0E) for March–June from 1980-2013. (C) Regionalization of Fig. 1B based on the spring rainy season CHIRPS precipitation

Throughout the analyses presented in this paper, we use 2.5° resolution interpolated OLR estimates derived from the Advanced Very High Resolution Radiometers (AVHRR) aboard National Oceanic and Atmospheric Administration (NOAA) polar orbiting satellites (Liebmann and Smith 1996) as a proxy for deep convective precipitation. Negative (positive) OLR anomalies correspond to positive (negative) precipitation anomalies. *High resolution (0.25°)* Sea surface temperature estimates come from the National Climatic Data Center (Reynolds et al. 2007*;* http://www.ncdc.noaa.gov/sst). All other atmospheric fields (i.e., geopotential height, wind vector data, pressure velocity (omega) and temperature) and sea level pressure (SLP) are drawn from the National Centers for Environmental Prediction (NCEP) Reanalysis I (Kalnay et al. 1996), which also has a resolution of 2.5°. OLR and Reanalysis data are distributed by the NOAA/Earth System Research Laboratory (ESRL) Physical Sciences Division (PSD; http://www.esrl.noaa.gov/psd/).

Atmospheric reanalysis is notoriously difficult for Africa, due to lack of observational data and complex atmospheric dynamics. As such, the choice of reanalysis dataset does represent a source of uncertainty in our analysis. In this study, NCEP Reanalysis I (NCEP-R1) is used because it has been verified over West Africa using pibal and rawinsonde reports (Nicholson and Grist 2001) and because it has been applied successfully in previous studies over EWA (e.g., Dezfuli and Nicholson 2012; Nicholson and Dezfuli 2013). Furthermore, in our studies of MJO impacts on EWA in boreal summer, we found general agreement between NCEP-R1, the NCEP–Department of Energy (DOE) Atmospheric Model Intercomparison Project II (AMIP-II) Reanalysis (R-2) dataset (Kanamitsu et al. 2002), and European Centre for Medium-Range Weather Forecasts (ECMWF) Interim Re-Analysis (ERA-Interim, Dee et al. 2011).

The USGS Climate Hazard Group Infrared Precipitation with Station (CHIRPS) merged gauge and satellite product (Funk et al. 2014), which is available at a 0.05^0 latitude/longitude resolution since 1981, is employed to investigate the anomalies in precipitation over EWA associated with the MJO. CHIRPS is used because it covers a longer time-period as compared to other daily precipitation datasets. The dataset is global but has an Africa focus, and it has already been used in several studies over Africa (Bastiaanssen et al. 2014; Platts et al. 2014; Simane et al. 2014). Nevertheless, as CHIRPS is a recent product with limited validation studies, it must be applied with some caution. All CHIRPS analyses presented in this paper were also performed using the Global Precipitation Climatology Project (GPCP; Huffman and Bolvin 2013) daily product for the period of GPCP availability (1997-2014). Results are generally similar and are not shown.

4.2.b. Data analysis

First, time-lagged linear regression and zero-lag composites of OLR, precipitation, temperature, SST, vertical motion, geopotential height, wind and moisture flux anomalies at different levels are computed for MAMJ based on each of the MJO indices described above. These anomalies are used to elucidate the associations between the MJO and convection and precipitation anomalies over EWA in the spring rainy season. Temporal autocorrelation was accounted for in all significance tests through reduced degrees of freedom. We calculated reduced degrees of freedom as follows:

$$\mathrm{N}' = N * \frac{1-\rho}{1+\rho} \qquad (1)$$

where N' is the reduced degrees of freedom and N is the number of temporal data points while ρ is lagged autocorrelation of the MJO index.

In the composite analysis, PC-EOF1 values greater than one standard deviation (σ) are considered enhanced intraseasonal convective events and PC-EOF1 values less than -1σ are taken as suppressed intraseasonal convective events. Over the study period, in MAMJ, there are 58 enhanced convection cases (655 days) and 64 suppressed convection cases (667 days) using PC-EOF1. Composites are calculated as the average of fields when PC-EOF1 is greater (less) than 1(-1)σ minus climatology.

Moisture transport anomalies from the tropical Atlantic Ocean to EWA are explored following Vigaud et al. (2009) and Nnamchi and Li (2011). The moisture flux at each pressure level is calculated by the formula below:

$$\mathbf{Q} = q_{lvl} v_{lvl} \qquad (2)$$

where q is specific humidity and v is horizontal wind speed. The subscript lvl denotes a specific atmospheric level. Further, following Behera et al. (1999) and Nnamchi and Li (2011), the vertically integrated moisture transport is calculated by vertically integrating equation (1), which can be written as:

$$\mathbf{Q} = \frac{1}{g} \int_{1000}^{300} q v dp \qquad (3)$$

where g is the acceleration due to gravity (9.81 m s^{-2}), q is specific humidity, and v is horizontal wind speed. The values 1000 and 300 indicate the pressure levels (hPa) over which the integration is computed. To test the significance of composites, a bootstrapping procedure outlined by Terray et al. (2003) is used. This procedure is useful to overcome weaknesses associated with the normality assumption of the Student's t-test.

Next, we compare the impacts of the MJO in the spring rainy season and in boreal summer by decomposing the MJO influence on tropical OLR into components associated with (1) the propagation of the MJO core convective envelope, (2) equatorial Rossby waves triggered by MJO activity in the Indian Ocean, and (3) equatorial Kelvin waves also triggered by MJO in the Indian Ocean using the wavenumber-frequency spectral analysis procedure presented by Wheeler and Kiladis (1999). The filtering is performed by creating an OLR dataset through an inverse transform that retains only the Fourier coefficients corresponding to the regions of the wavenumber-frequency domain of each signal shown in Figure 4.2 (see Wheeler and Kiladis (1999) for details on the calculation techniques). We then regressed a number of relevant time-lagged variables against PC-EOF1 to investigate the evolution of associations between convection anomalies over EWA and the MJO and to compare their relative importance in the spring rainy season and in boreal summer.

To investigate impacts of the enhanced and suppressed phases of the MJO on precipitation distribution, we started with testing the homogeneity of the region influenced by MJO (Figure 4.1B) via objective regionalization techniques described in Badr et al. (2015). As our goal was to divide the region into subregions that respond differently to large-scale forcings of intra-seasonal variability, we performed the analysis on daily precipitation of each season using the "regional linkage" hierarchical clustering method, which minimizes correlation between subregions. This analysis yielded two largely independent subregions (Figure 4.1C) for MAMJ. Analyses were performed in R using the HiClimR package (Badr et al. 2014). The average intra-regional correlations for both regions A and B in Figure 4.1C are statistically significant at the 99%

significance level while the correlation between the two regions is insignificant. Then, we analyzed the influence of the MJO on precipitation extremes in each region separately.

To streamline the presentation results, we only present composites based on when PC-EOF1 time series has amplitude greater than 1σ. The analyses are performed using daily data for the both seasons and are repeated separately for each month to examine the intraseasonal variability of the impacts of the MJO on convection over the region. All analyses are performed for the time period 1980-2013 except for those involving SST (1982-2013) and CHIRPS (1981-2013).

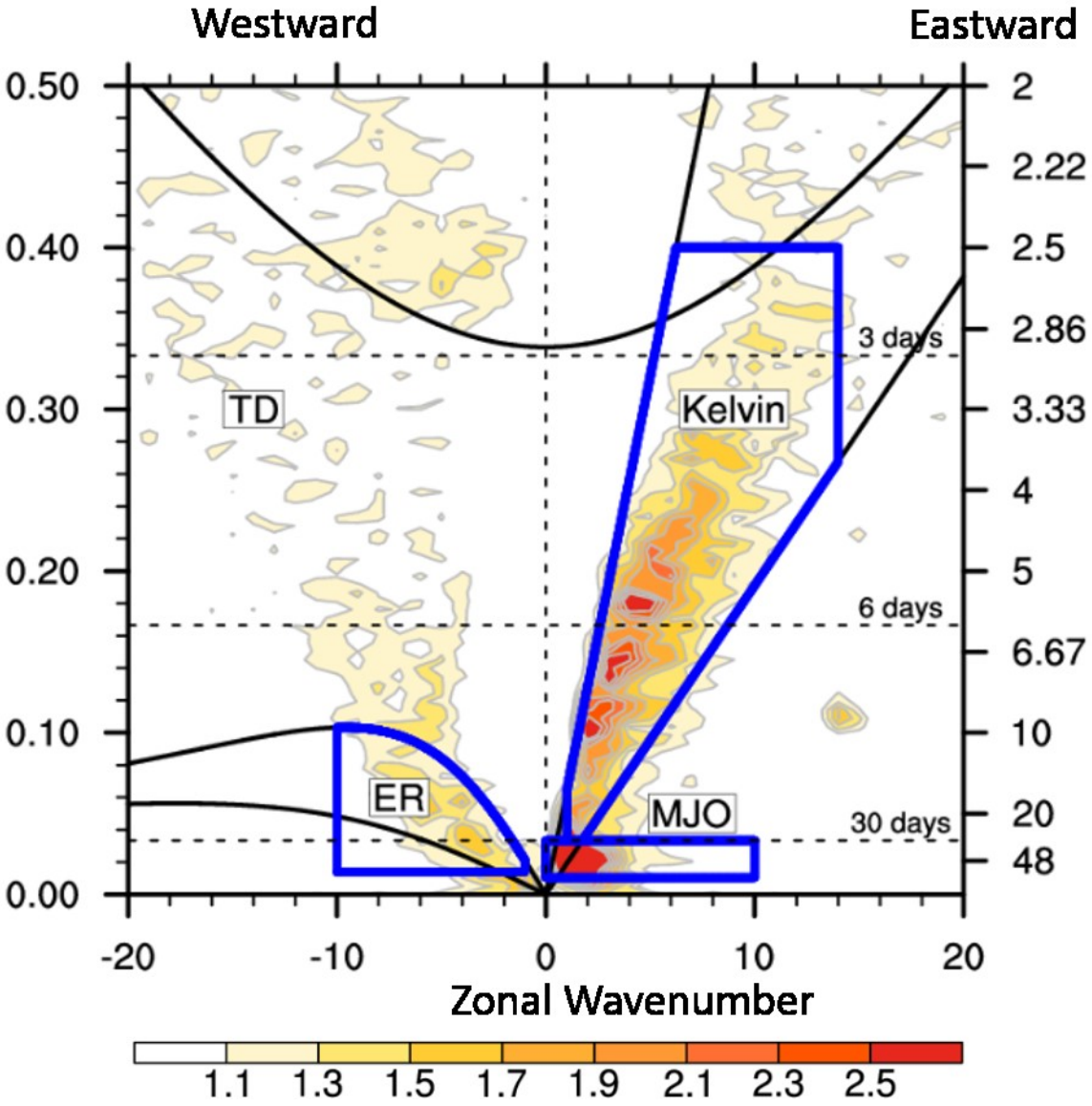

Figure 4.2. Wavenumber–frequency spectra of OLR component symmetric about the equator for March-June 1980-2013 summed from 15^0S–15^0N divided by the background spectrum. Black lines denote shallow water equatorial wave dispersion curves for equivalent depths of 8 and 90 m. Blue boxes define the filter bands used in this study [Graphic design after Schreck et al. 2013] (see Wheeler and Kiladis 1999 for details on the computation techniques).

4.3. Results and discussion

4.3.a. Links of the MJO to convection anomalies over West Africa

Figure 4.3 shows composites of unfiltered MAMJ OLR based on each of the MJO indices. Generally, all indices yield similar results. OMI, RMM and VPM give negative OLR anomalies when the MJO is in phase 1 (Figures 4.3A, 4.3C and 4.3E), which is when the MJO convective envelope is centered over Africa and the western Indian Ocean. Conversely, significant positive OLR anomalies are found during MJO phase 5 (Figures 4.3B, 4.3D and 4.3F). This shows that when the MJO convective envelope is centered over the Maritime continent, Equatorial West Africa experiences anomalous dryness.

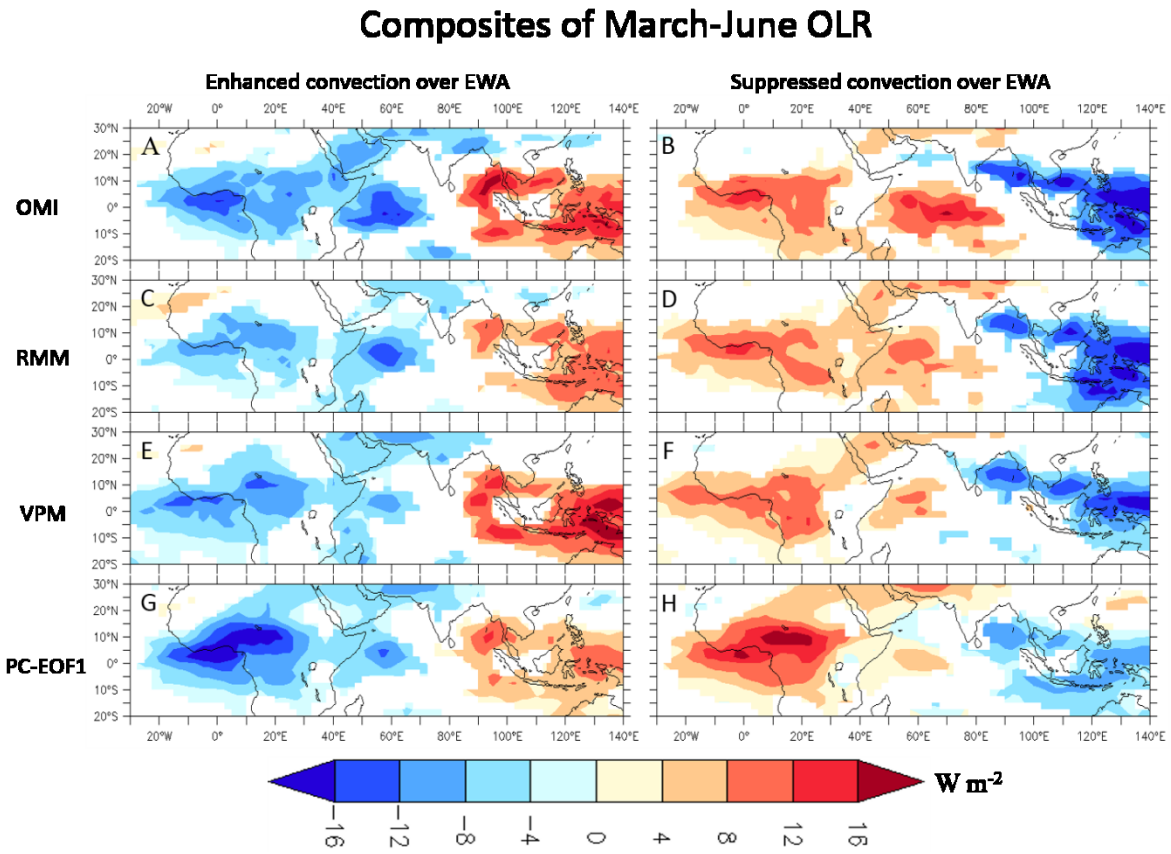

Figure 4.3. Composites of March-June unfiltered OLR (W m^{-2}). (A,B) using OMI, (C,D) based on RMM, (E,F) using VPM, (G,H) based on PC-EOF1. (A,C,E) phase 1, (B,D,F) phase 5. (G) PC-EOF1 > 1σ and (H) PC-EOF1 < -1σ. Results shown are significant at the 90% confidence level.

In MAMJ, composites of OLR based on PC-EOF1 provide results that are generally similar to the conventional MJO indices, and they are similar to the findings of Gu (2009) (see their figs. 3 and 4e). When the value of PC-EOF1 is greater than one σ (Figure 4.3G), we observe negative OLR anomalies over West Africa, which correspond to anomalous wetness over the region, and positive OLR anomalies in the maritime continent associated with MJO convective activity. The negative OLR anomalies shown in Figure 4.3 represent from 45-70% of the standard deviation of the

unfiltered OLR over the region covering 10^0W-25^0E and 5^0S-10^0N. This demonstrates that the MJO has substantial influence on deep convective precipitation of the region.

When PC-EOF1 is less than negative one σ, the region experiences suppressed convection (Gu 2009; Figure 4.3H). Therefore, generally speaking, in MAMJ, large positive values of PC-EOF1 correspond to phase 1 of the MJO and large negative values of PC-EOF1 correspond to phase 5 of the MJO as defined by the other indices considered in this study. However, the composites of OLR based on PC-EOF1 give stronger composites over West Africa and weaker values over the maritime continent as compared to the other MJO indices (Figure 4.3). It is also worth noting that the composites of OLR over West Africa based on the different MJO indices (Figure 4.3) have a similar spatial pattern to the loading of the first EOF of 20-100-day bandpass filtered OLR centered over West Africa (4.1B), which is similar to Fig. 3 of Gu (2009).

We compare the impacts of the MJO in the spring rainy season and the boreal summer (JAS) using consistent data and analysis methods. Though we do find generally similar results for all MJO indices for the spring rainy season, this is not the case in JAS. In JAS, we see rather significant differences in OLR composites based on different MJO indices (Figure 4.4). In JAS, substantial difference in both EWA and Indian Ocean OLR anomalies are observed between the four different indices (Figure 4.4). Comparison of Figure 4.3 to Figure 4.4 reveals that the choice of MJO index makes relatively little difference for analyses of the spring rainy season but makes a large difference for analyses of boreal summer. Hence the choice of MJO index represents a potential source of uncertainty in studies of MJO influence, and our use of PC-EOF1 cannot be extended to other regions and seasons without careful consideration.

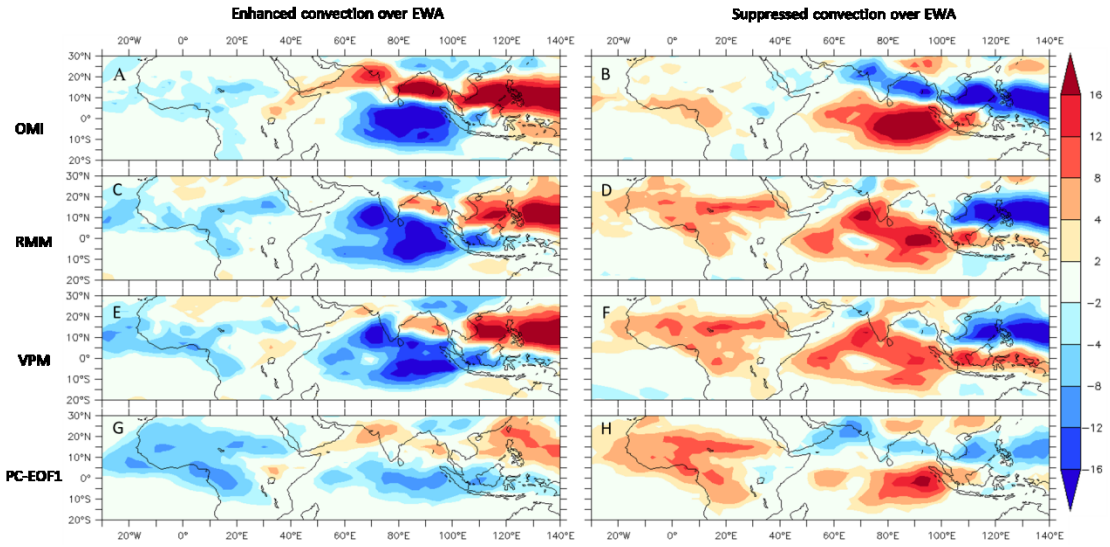

Figure 4.4: Unfiltered OLR composites (1980-2013) for summer (JAS) based on EWA enhanced and suppressed convection phases for four different MJO indices. Note the substantial difference in both EWA and Indian Ocean OLR anomalies between the four different indices. For OMI, RMM and VPM enhanced/suppressed convection associated with the MJO is maximum at phase 2/6.

The OLR composites shown in Figure 4.3 also suggest that the influence of the MJO on EWA convection is somewhat stronger in the spring rainy season than the boreal summer, a period that has been studied by Janicot et al. (2009) and Mohino et al. (2012). Both our analysis (Figures 4.3 and 4.4) and comparison with Janicot et al. (2009) and Mohino et al. (2012) indicate that the connection between MJO and EWA convection is stronger during the spring rains.

The influence of the MJO on spring rains over EWA is shown in Figure 4.5. The composites confirm the fact that the MJO modulates spring precipitation over large parts of EWA. When PC-EOF1 is greater than 1σ, positive precipitation anomalies are observed over most parts of

EWA (Figure 4.5A), on the other hand, negative precipitation anomalies prevail over the region when PC-EOF1 is less than -1σ (Figure 4.5B). This is consistent with Gu (2009) who find significant results by regressing TRMM Multi-satellite Precipitation Analysis (TMPA) rainfall product against PC-EOF1. Over large portions of EWA, the positive and negative composites have magnitude greater than 1 mm/day. This constitutes a difference on the order of 20-50% from average daily rain rates for the season (Figures 4.5C and 4.5D). The other MJO indices give similar results (not shown). We also checked using GPCP dataset, which covers a shorter time period, and the results are generally consistent.

To investigate MJO associations with zonal circulation patterns affecting EWA in MAMJ, we examine longitude-height cross-section of circulation composites (Figure 4.6). The two dimensional wind vectors in the figure are calculated by dividing the actual zonal winds and vertical velocity by their respective standard deviation for the entire cross-sectional domain (20^0 W-140^0 E and 8^0 S-12^0 N). Therefore, the magnitude of the vectors in Figure 4.6 is a measure of the local strength of the circulation relative to that across the cross-sectional domain. As shown in Figure 4.6A, when PC-EOF1 is greater than 1σ, there is enhanced upward vertical motion over EWA and subsidence over the Maritime Continent. On the other hand, when PC-EOF1 is less than -1σ, there is anomalous subsidence over EWA and anomalous ascent over the Maritime Continent (Figure 4.6B). Circulation composites using phase 1/phase 5 of the conventional MJO indices are similar to Figures 4.6A/4.6B, respectively (not shown). The circulation composites shown in Figure 4.6 are physically consistent with the OLR anomalies presented in Figures 4.3 & 4.4, and precipitation composites shown in Figure 4.5.

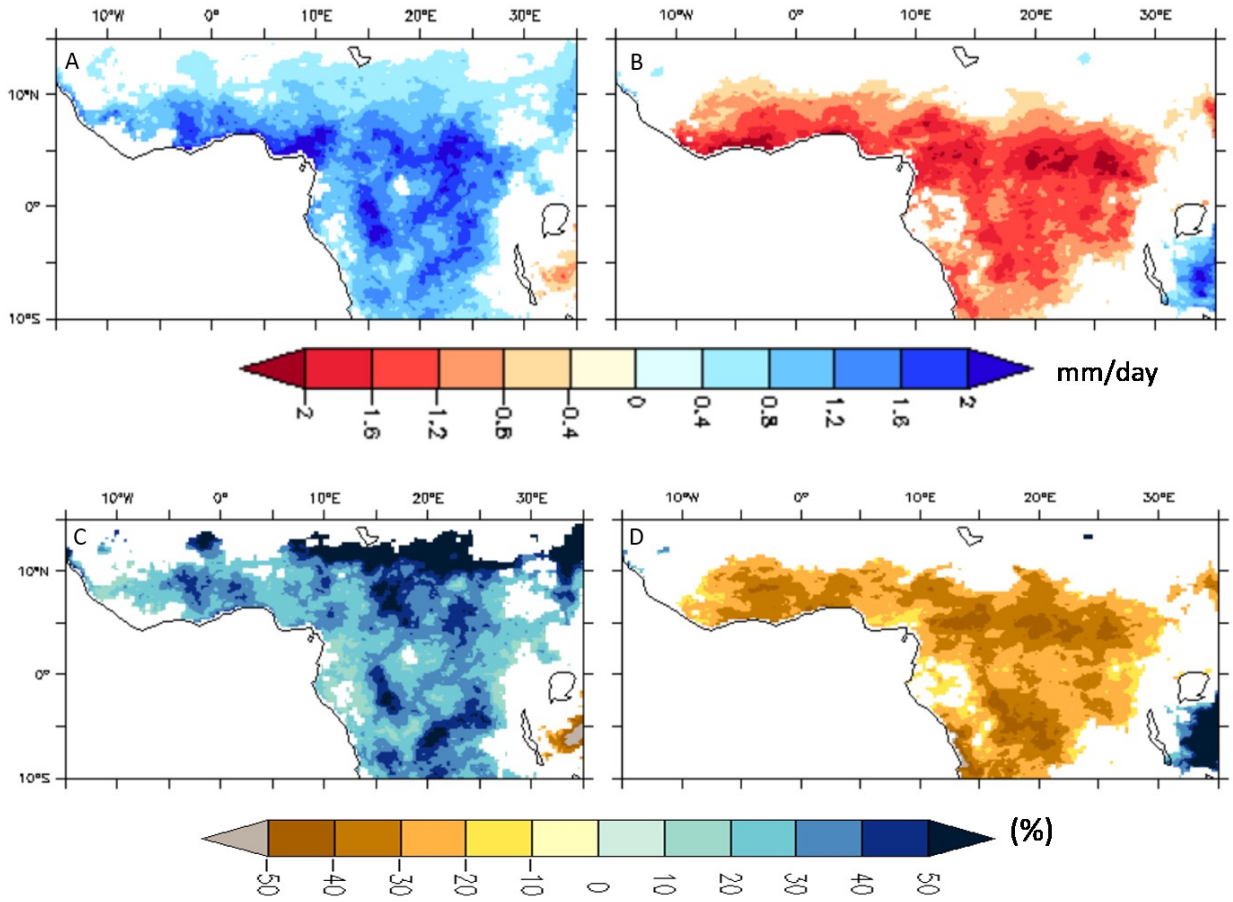

Figure 4.5. (A, B) composites of March-June raw precipitation (mm day^{-1}) from 1981-2013. (C, D) composites of March-June raw precipitation divided by the MAMJ average rain rate (%). (A,C) PC-EOF1 > 1σ and (B,D) PC-EOF1 < -1σ. Shading shows results significant at the 90% confidence level.

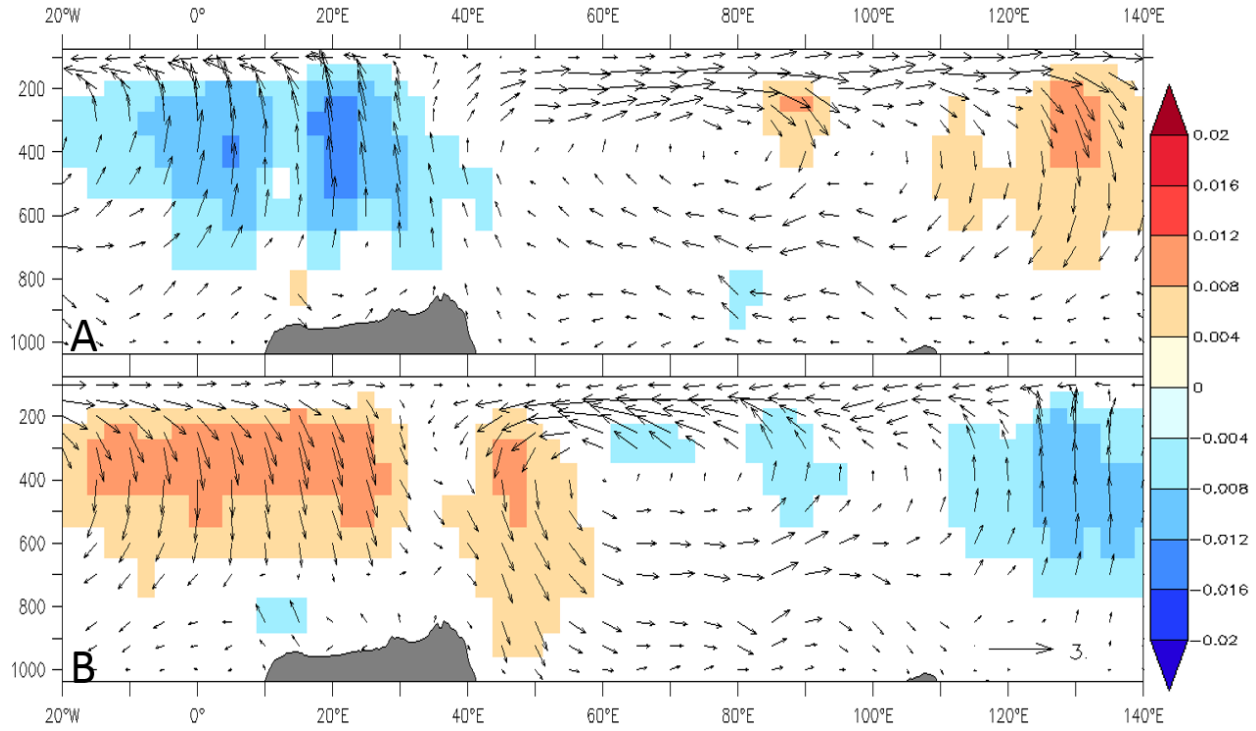

Figure 4.6. Composites of March-June longitude-height cross-section of raw circulation, expressed as normalized zonal winds and vertical velocity (see text for explanation), averaged from 8^0 S -12^0 N, from 1980-2013. Horizontal wind anomalies are in m s^{-1} (standard deviation)$^{-1}$, and vertical velocity anomalies are in Pa s^{-1} (standard deviation)$^{-1}$, where the deviation for each variable is calculated over the entire cross-sectional domain. (A) PC-EOF1 > 1σ and (B) PC-EOF1 < -1σ. Shading shows that vertical velocity (Pa s^{-1}, negative upwards) anomalies are significant at the 90% confidence level.

To explore moisture advection anomalies associated with the MJO in MAMJ, composites of vertically integrated moisture flux are presented in Figure 4.7. As Figure 4.7A shows, there is enhanced moisture transport from the equatorial Atlantic Ocean to EWA when PC-EOF1 is greater than 1σ. Conversely, when PC-EOF1 is less than -1σ, the moisture transport to EWA from the

equatorial Atlantic Ocean is anomalously negative (Figure 4.7B). The vertically integrated moisture fluxes are shown for simplicity, recognizing that much of this signal is driven by near surface moisture flux.

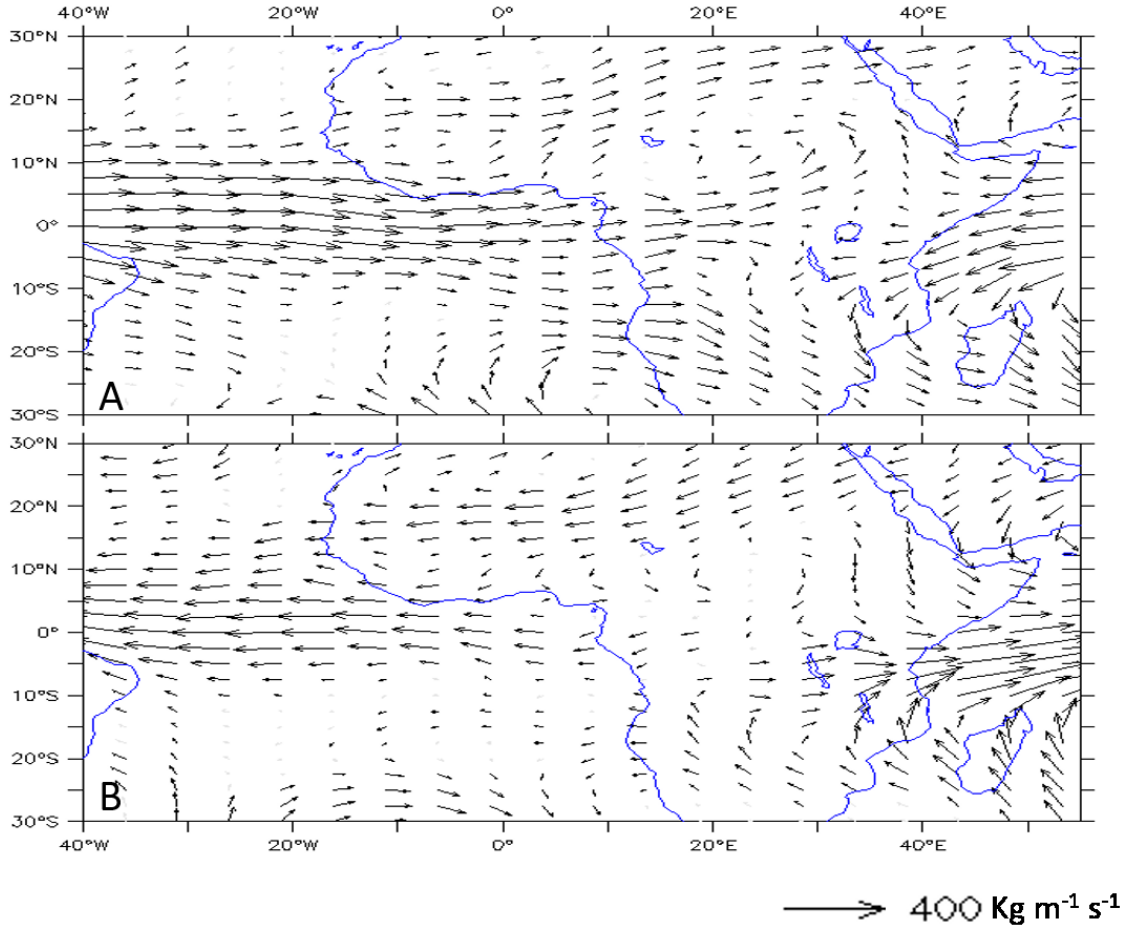

Figure 4.7. Composites of March-June vertically integrated moisture transport (kg $m^{-1}s^{-1}$), from 1980-2013. (A) PC-EOF1 > 1σ and (H) PC-EOF1 < -1σ. Black vectors indicate that moisture flux anomalies are significantly different from zero at the 90% confidence level in at least one of the directions (meridional or zonal).

Since all MJO indices provide similar results for MAMJ, and PC-EOF1 captures maximum MJO influence in boreal summer, from this point on we use only the PC-EOF1 index to examine the

mechanisms of MJO influence on convection over EWA, and to compare the relative strengths of the MJO influence over the region in both seasons. As a starting point, Figure 4.8 presents regression of raw OLR against PC-EOF1 for MAMJ and JAS. The regression maps for MAMJ are similar to the findings of Gu (2009) and the JAS results are generally similar to the findings of Janicot et al. (2009) and Mohino et al. (2012) who consider the June-September season in their analysis. We show both here to facilitate seasonal comparisons and provide a point of reference for wavenumber-frequency spectral analysis.

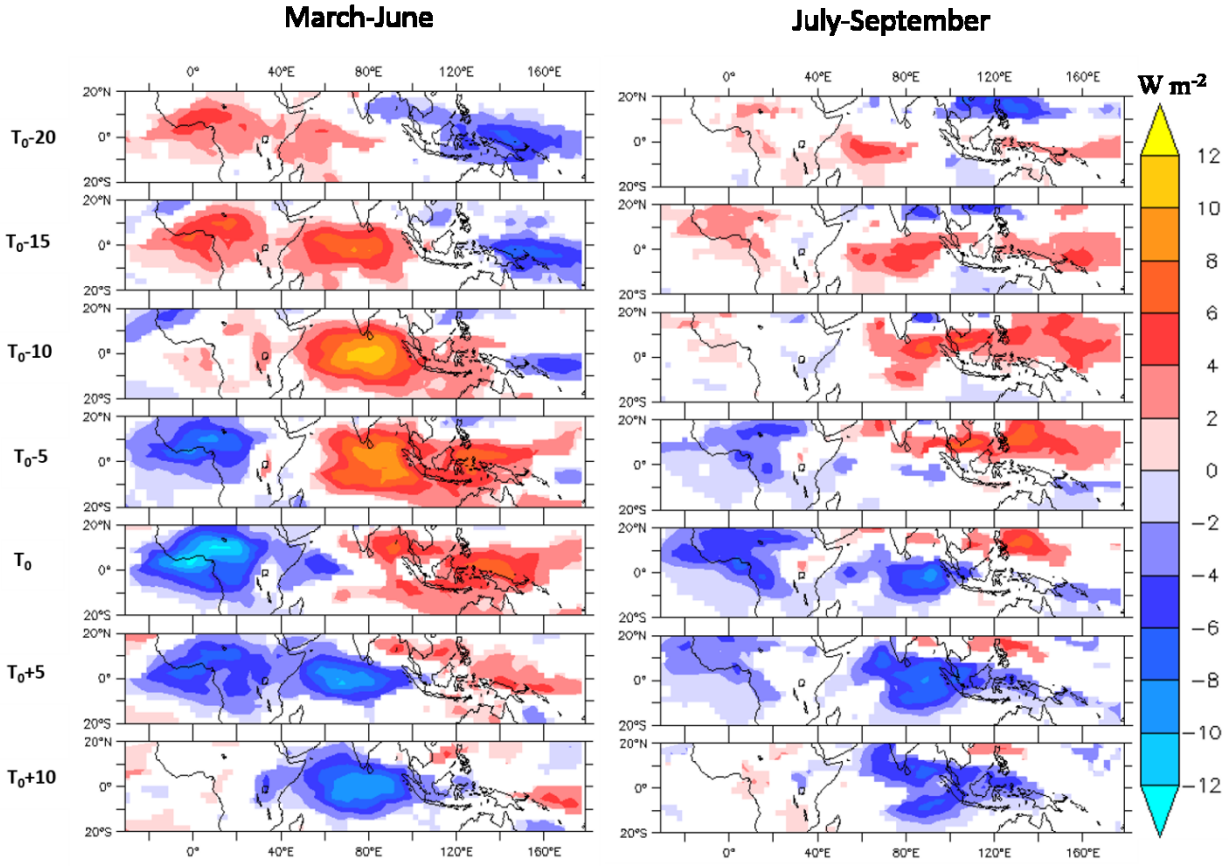

Figure 4.8. Regression of time-lagged raw OLR against PC-EOF1 for 1980-2013. (left panel) MAMJ, (right panel) JAS. Time T_0 is a zero-lag regression, times T_0-20 days to T_0-5 days are time-lead OLR and winds regressed on PC-EOF1 and T_0+5 days to T_0+10 days are time lag regressions. Shading indicates values significant at the 90% confidence level. Black vectors

indicate values significantly different from zero at the 90% confidence level in at least one of the wind components (meridional or zonal).

In Figure 4.8, time T_0 refers to zero-lag regressions; i.e., the patterns of OLR correlations for when the MJO signal in EWA is greatest. The other panels show regression sequence for lags from -20 days through +10 days (T_0-20 to T_0+10), with an interval of 5 days. This sequence shows the evolution of OLR associations preceding and following the time of maximum MJO influence on EWA. At T_0 OLR modulation of more than 26 Wm^{-2} around the mean is observed (Figures 4.3 and 4.8) in MAMJ, with positive PC-EOF1 values corresponding to enhanced convection over EWA. As shown in Figure 4.8, at T_0-20 and T_0-15, suppressed convection prevail over EWA in both seasons, whereas from T_0-5 to T_0+5, the region experiences enhanced convection in both MAMJ and JAS. However, we can see from the regression sequence that the MJO impact is stronger in the spring rainy season than in boreal summer. For example, at time T_0 the MJO signal over EWA in MAMJ is up to more than double of the signal observed in boreal summer.

At T_0-20, we observe that in both seasons positive OLR anomalies start to develop over the Western Equatorial Indian Ocean and move eastward and strengthen up to T_0-5. Subsequently, the negative OLR anomalies that start to develop on T_0 over the western equatorial Indian Ocean migrate eastward while increasing in intensity up to T_0+10. The sequence of linear regressions displayed in Figure 4.8 is consistent with the composites shown in Figure 4.3 and 4.4 for all MJO indices: when convection is suppressed over EWA, we observe enhanced convection over the western Pacific Ocean warm pool region (T_0-20 to T_0-15), and when convection is suppressed

over the warm pool region, EWA experiences anomalous wetness (T_0 -5 to T_0+5). At T_0-15 and T_0-10, we observe that the MJO signal is stronger over the Indian Ocean in MAMJ than in JAS. This has implications for the strength of the equatorial waves triggered in the Indian Ocean basin by diabatic heating anomalies associated with the MJO anomalies over the Indian Ocean and we will investigate this in the next sections.

In both seasons, at T_0-10 days, the Gulf of Guinea experiences anomalous positive SST (not shown). This is consistent with Lavender and Matthews (2009), who document that positive (negative) SST anomalies associated with the MJO, generally, lead the enhanced (suppressed) convection of the MJO by approximately 10-12 days. However, the coherence and significance of these patterns is weak, and we do not explore this mechanism further in this paper.

Analysis of the propagation of MJO equatorial waves has proved to be fruitful for studies of MJO influence on EWA summer rains (Janicot et al. 2009; Lavender and Matthews 2009; Mohino et al. 2012), but such analysis has not been performed for the spring rainy season, even though it is a period when MJO activity tends to be stronger. Indeed, a regression sequence of PC-EOF1 against time-lagged 925-hPa wind and geopotential height from T_0-20 to T_0+10 (Figure 4.9) shows distinct wave-like patterns. On day T_0, negative 925-hpa geopotential height anomalies start to develop over the Western Equatorial Indian Ocean (Figure 4.9). From Figure 4.8 (left panel), we see that negative OLR anomalies begin to develop over the western equatorial Indian Ocean on day T_0, indicating the onset of the MJO over the western Indian Ocean. This is consistent with MJO dynamics, as the onset of the MJO over the western Indian Ocean is characterized by the development of a negative low level geopotential height anomaly which leads to enhanced

boundary layer convergence, convection and precipitation over the region (Lavender and Matthews 2009). These fields have baroclinic vertical structures and change sign around 500 hPa (Janicot et al. 2009). These patterns point to the potential for the MJO to influence the EWA spring rains through equatorial wave activity.

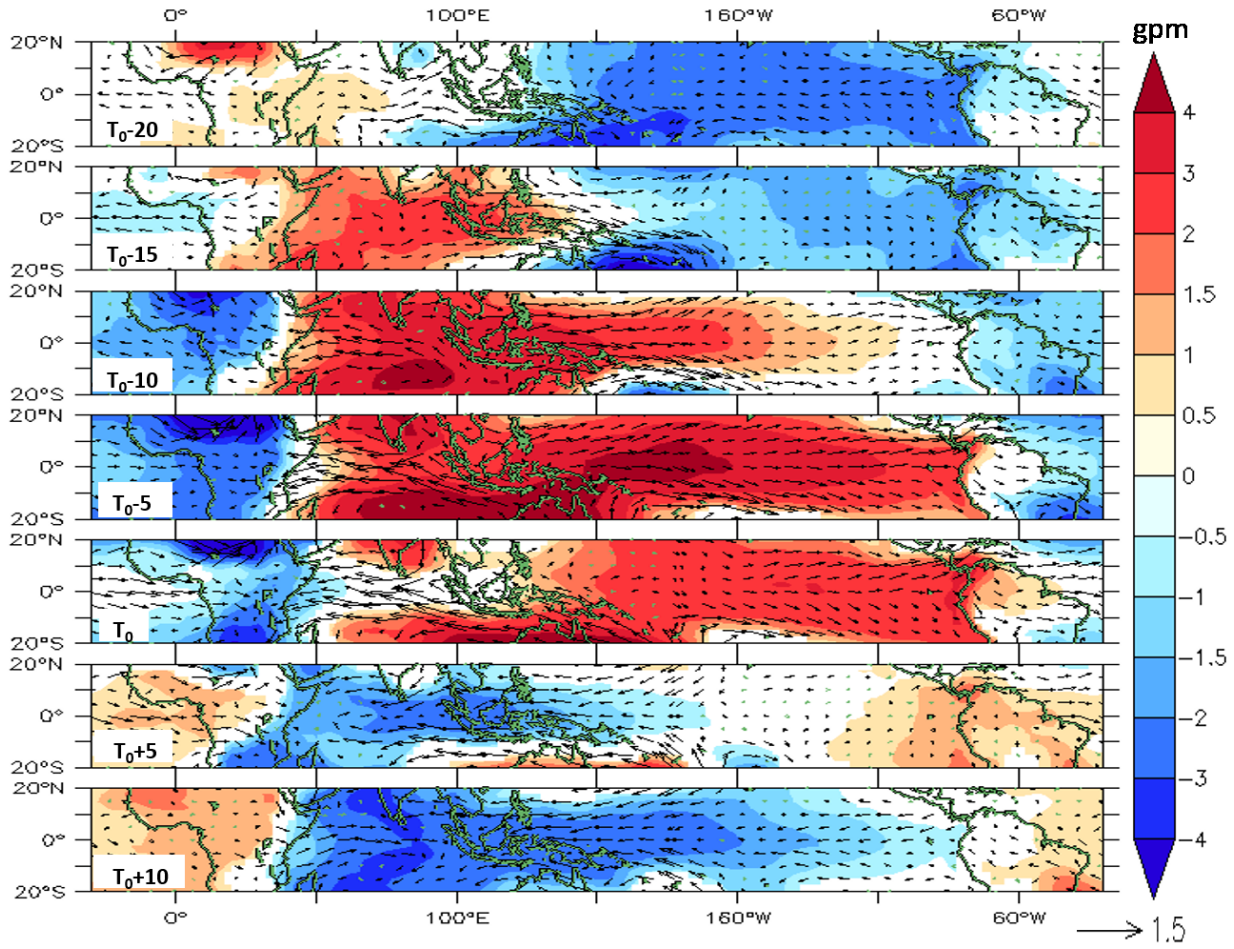

Figure 4.9. Regression of unfiltered geopotential height (geopotential meters (gpm)) and wind vectors (m s^{-1}) at 925 hPa against PC-EOF1 for MAMJ 1980-2013. Time T_0 is a zero-lag regression, times T_0-20 days to T_0-5 days are time-lead geopotential and winds regressed on PC-EOF1 and T_0+5 days to T_0+10 days are time lag regressions. Shading indicates geopotential height anomalies significant at the 90% confidence level. Black vectors indicate values

significantly different from zero at the 90% confidence level in at least one of the wind components (meridional or zonal).

4.3.b. Equatorial Waves

Anomalies in convection over the Indo-Pacific warm pool can trigger dry eastward moving Kelvin and westward moving Rossby waves (Gill 1980). Matthews (2004), Janicot et al. (2009), Lavender and Matthews (2009) and Mohino et al. (2012) have documented that during boreal summer, West African convection is modulated by diabatic heat anomalies associated with the suppressed and active phases of the MJO over the Indo-Pacific warm pool. Diabatic heating over the region results in a dry Kelvin wave that is associated with positive equatorial tropospheric temperature anomalies, easterly wind anomalies at low levels and descent at the wave front. Moreover, it excites a dry Rossby wave to its west which is associated with a couple of twin cyclones that straddle the equator in low levels, with westerly anomalies over the equator and descent to the west of the cyclone.

Diabatic cooling, on the other hand, triggers a dry Kelvin wave that is associated with negative equatorial tropospheric temperature anomalies, westerly wind anomalies at low levels and ascent at the wave front. In addition, it excites a dry Rossby wave which is associated with a couple of twin anticyclones straddling the equator in low levels, with easterly anomalies over the equator and ascent to the west of the anticyclone (Janicot et al. 2009 and Mohino et al. 2012).

We note that these dry Kelvin waves only become free to propagate on their own when MJO convection dissipates. The convectively coupled Kelvin waves associated with propagation of the

MJO are forced by the MJO convective core and are tied to its eastward propagation. Propagation of these convectively coupled waves is evident in propagating OLR anomalies (Straub and Kiladis 2003; Straub et al. 2006; Sobel and Kim 2012). Moreover, the convectively coupled waves are complex and not easily explainable as the dry waves since their scales do not correspond to that expected from the linear theory of dry waves (Kiladis et al. 2009; Nguyen 2014).

Fields plotted in Figures 4.8 and 4.9 show evidence of this MJO-associated equatorial Kelvin-Rossby wave pattern. As shown in the left panel of Figure 4.8, about 15 days before the enhancement of convection over EWA (T_0-15), there is a positive OLR anomaly over the Indian Ocean, indicative of the suppressed phase of the MJO. The Kelvin Wave response is visible in Figure 4.9 as a tongue of positive geopotential height anomaly that grows eastward along the equator, resulting in strengthened low-level westerly winds over the tropical Pacific. Notably, the geopotential height anomaly crosses the Atlantic Ocean and migrates over Africa, with wind anomalies reaching EWA at T_0-5. This influence appears to be specific to the spring rainy season: Janicot et al. (2009) found that the geopotential height anomaly does not propagate beyond 50°W in boreal summer, and that Kelvin wave activity has little influence on EWA rainfall in that season.

Figure 4.8 also shows some evidence of an Equatorial Rossby wave response to Indian Ocean OLR anomalies. This is visible in easterly low level wind anomalies and a horseshoe-shaped pattern of positive geopotential height anomalies symmetric about the equator visible in the western Indian Ocean at T_0-10. However, in the regression of raw data shown in Figure 4.9, the Rossby wave features are not as clearly visible as the Kelvin wave. This can be partly attributed to the interaction

of the Rossby wave response with the Kelvin wave propagating from the Atlantic Ocean and Africa to the western Indian Ocean.

At T_0 active MJO convection develops over the western Indian Ocean, and this convective center strengthens and extends eastward through T_0+5 and T_0+10. This convective activity results in negative geopotential height anomalies due to diabatic heating. The Kelvin wave associated with this atmospheric pattern is accompanied by strengthened easterly anomalies over the entire tropical Pacific Ocean, as can be seen in Figure 4.9 at T_0+5 and T_0+10. This negative geopotential height anomaly propagates to the Atlantic Ocean and Africa resulting in divergent easterly wind anomalies over the eastern Atlantic Ocean and West Africa. This pattern results in increased subsidence over the region and dry anomalies prevail over EWA. The westward moving cyclone associated with the Rossby wave enhances this subsidence.

To quantify the relative contributions of the convectively coupled waves to the MJO influence on MAMJ EWA convection and to compare the strength of the impacts of these waves in the spring rainy season and in boreal summer, we present regression of PC-EOF1 against OLR filtered to the characteristic wavenumber and frequency of MJO, Rossby waves, and Kelvin waves (boxes in Figure 4.2) in Figures 4.10-4.12. Figure 4.10 shows the MJO-filtered OLR signal regressed against PC-EOF1 for both seasons. We can observe that in MAMJ, the figure retains much of the signal seen in Figure 4.8, indicating that a considerable amount of the MJO influence on West Equatorial African springtime precipitation is directly attributable to the migration of the MJO center of convection. This contrasts with boreal summer, when the direct influence of MJO convection on West Africa is comparatively modest. Janicot et al. (2009) and our own analysis (Figure 4.10 right

panel) suggest a weak impact, while Mohino et al. (2012), using different data and methods, find a direct impact that is more pronounced but still not as strong as our results for the spring rains. Even so, the magnitude of the MJO-filtered OLR anomaly in MAMJ in Figure 4.10 is weaker than in the non-filtered OLR data shown Figure 4.8, suggesting that the direct impact of MJO convection is not the sole mechanism of MJO-influence during the spring months.

The Rossby-filtered OLR, which has a westward propagating signal, is shown in Figure 4.11. Its maximum anomaly over EWA coincides with the maximum signal of the MJO-filtered OLR which occurs at T_0, but the Rossby-filtered signal is considerably weaker (compare Figure 4.10 to Figure 4.11, noting the difference in color scale) in MAMJ. In JAS, both MJO-filtered and Rossby-filtered OLR give similar results but while the MJO-filtered OLR values are generally centered along the equator, the Rossby-filtered results propagate centered along about 10^0N. This is because the Indian Summer Monsoon triggers Rossby waves which propagate over North Africa (Janicot et al. 2009). The mechanism of Rossby wave generation differs between the two seasons: in boreal summer, in addition to the MJO anomalies over the Indian Ocean, the active/break cycle of the Indian monsoon influences initiation of Rossby Waves that propagate westward over North Africa (Janicot et al. 2009). In March-June the Rossby waves appear to be initiated over the Equatorial Indian basin as a result of the diabatic heating anomalies caused by the enhanced and suppressed phases of the MJO over the region (Figures 4.8 and 4.11). We observe positive OLR anomaly in MAMJ over east Africa associated with the Rossby Wave at T_0+5 (Figure 4.11) which could be one reason for the observed split of negative OLR signal going from T_0 to T_0 +5 days (Figure 4.8).

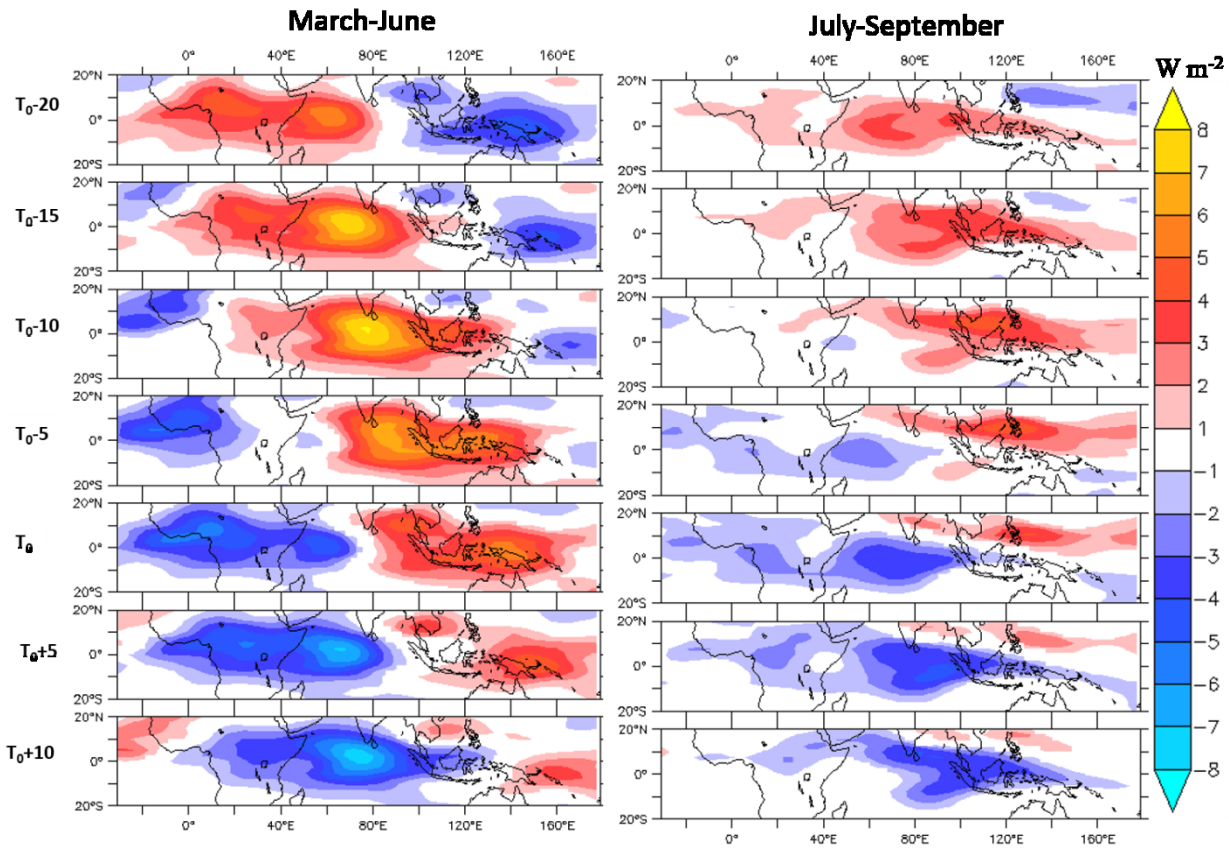

Figure 4.10. Regression of MJO-filtered OLR against PC-EOF1 for 1980-2013. (left panel) MAMJ, (right panel) JAS. Times T_0-20 to T_0+10 comprise a lagged regression sequence, as in Figure 8. Shading indicates values significant at the 90% confidence level.

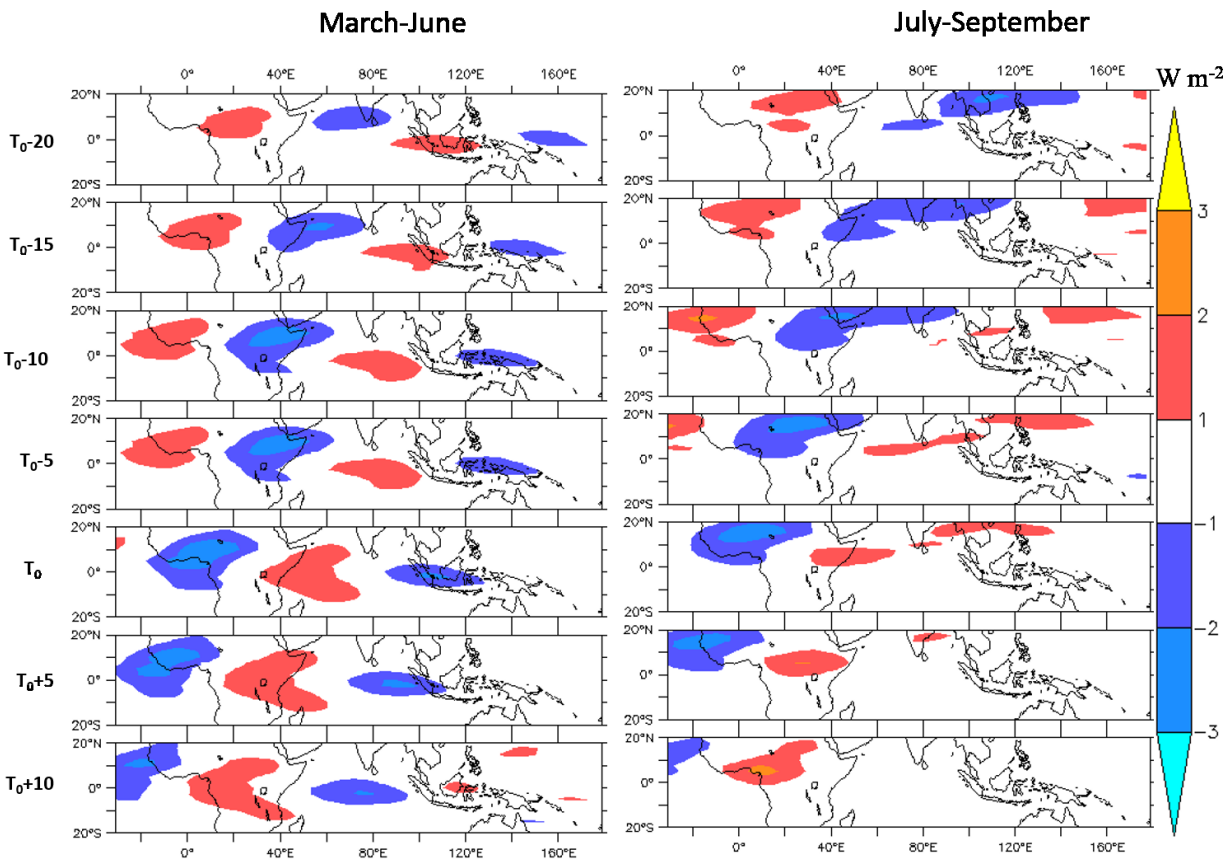

Figure 4.11. Regression of time-lagged Rossby-filtered OLR against PC-EOF1 for 1980-2013. (left panel) MAMJ, (right panel) JAS. This regression sequence is shown from T_0 -20 to T_0+10 days, as in Figures 8 and 9. Shading indicates values significant at the 90% confidence level.

The regression time sequence of Kelvin-filtered OLR (Figure 4.12) is also weaker than the MJO-filtered signal in MAMJ, but it does show clear evidence of a Kelvin wave influence on OLR over EWA. Studies of boreal summer have found that these equatorial convectively coupled Kelvin waves do not significantly impact convection over the region (Janicot et al. 2009; Mohino et al. 2012). Our analysis also agrees with previous studies that the Kelvin wave does not have significant impacts on EWA convection in boreal summer (Figure 4.12 right panel). The Kelvin-filtered OLR signal in MAMJ in Figure 4.12 is consistent with the Kelvin wave-associated

geopotential height features shown in Figure 4.9, and indicates that the Kelvin influence extends across the Atlantic Ocean and into EWA during the spring rainy season. Of course, because of possible spectral leakage on the filtered results, the contribution of the MJO, Kelvin and Rossby signals could be larger than the results shown.

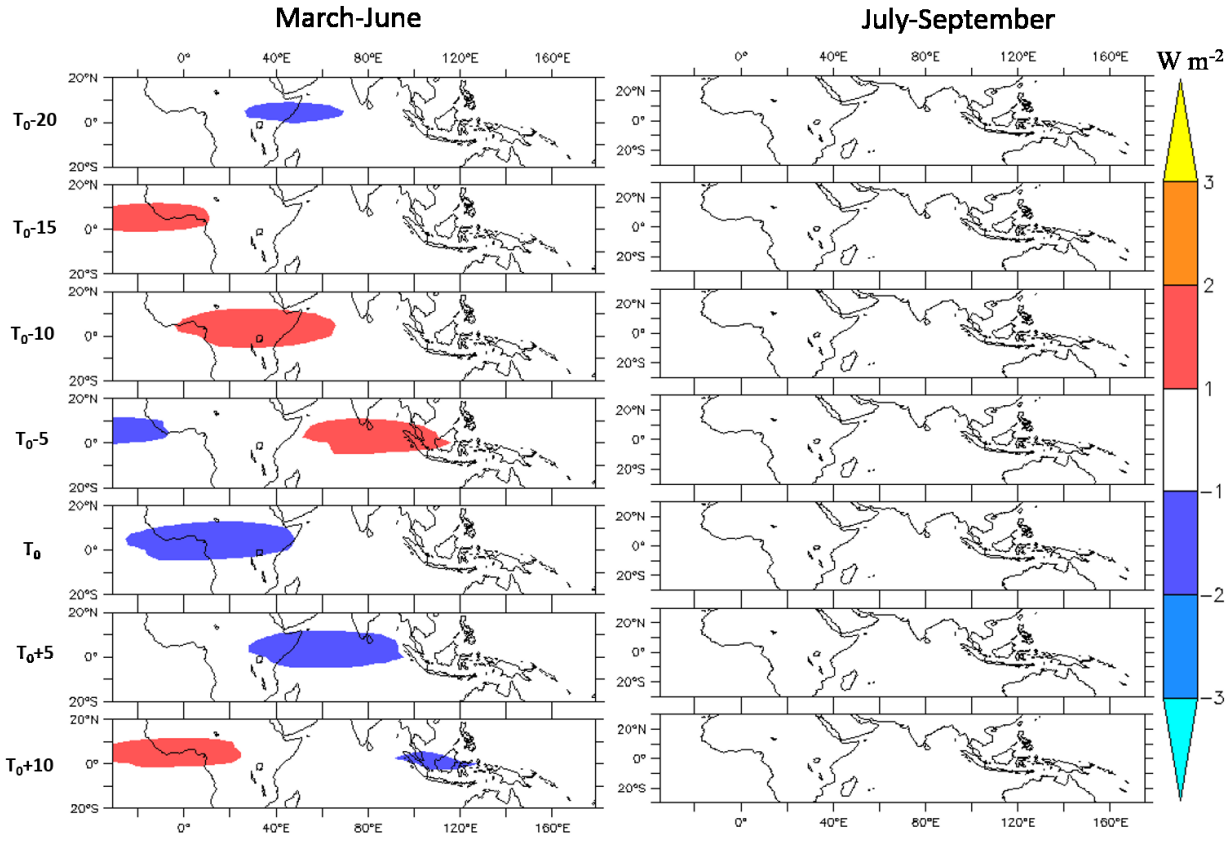

Figure 4.12. Regression of time-lagged Kelvin-filtered OLR against PC-EOF1 for 1980-2013. (left panel) MAMJ, (right panel) JAS. This regression sequence is shown from T_0 -20 to T_0+10 days, as in Figures 8-10. Shading indicates values significant at the 90% confidence level.

The sum of the MJO-, Rossby-, and Kelvin-filtered OLR signals for both seasons is shown in Figure 4.13. This sum is qualitatively similar to the unfiltered OLR regression pattern shown in Figure 4.8, with a slightly lower magnitude. This study shows that in addition to the eastward-

propagating MJO signal, a convectively coupled westward-propagating equatorial Rossby wave and an eastward moving Kelvin wave are needed to explain the overall impact of the MJO on convection over Equatorial West Africa in March-June. In boreal summer, the MJO impact over Equatorial Africa is weaker than what is observed in the spring rainy season. Moreover, while the Kelvin wave triggered by the MJO in the Indian Ocean has significant impacts on convection in the spring rains, its impacts in the summer season are insignificant.

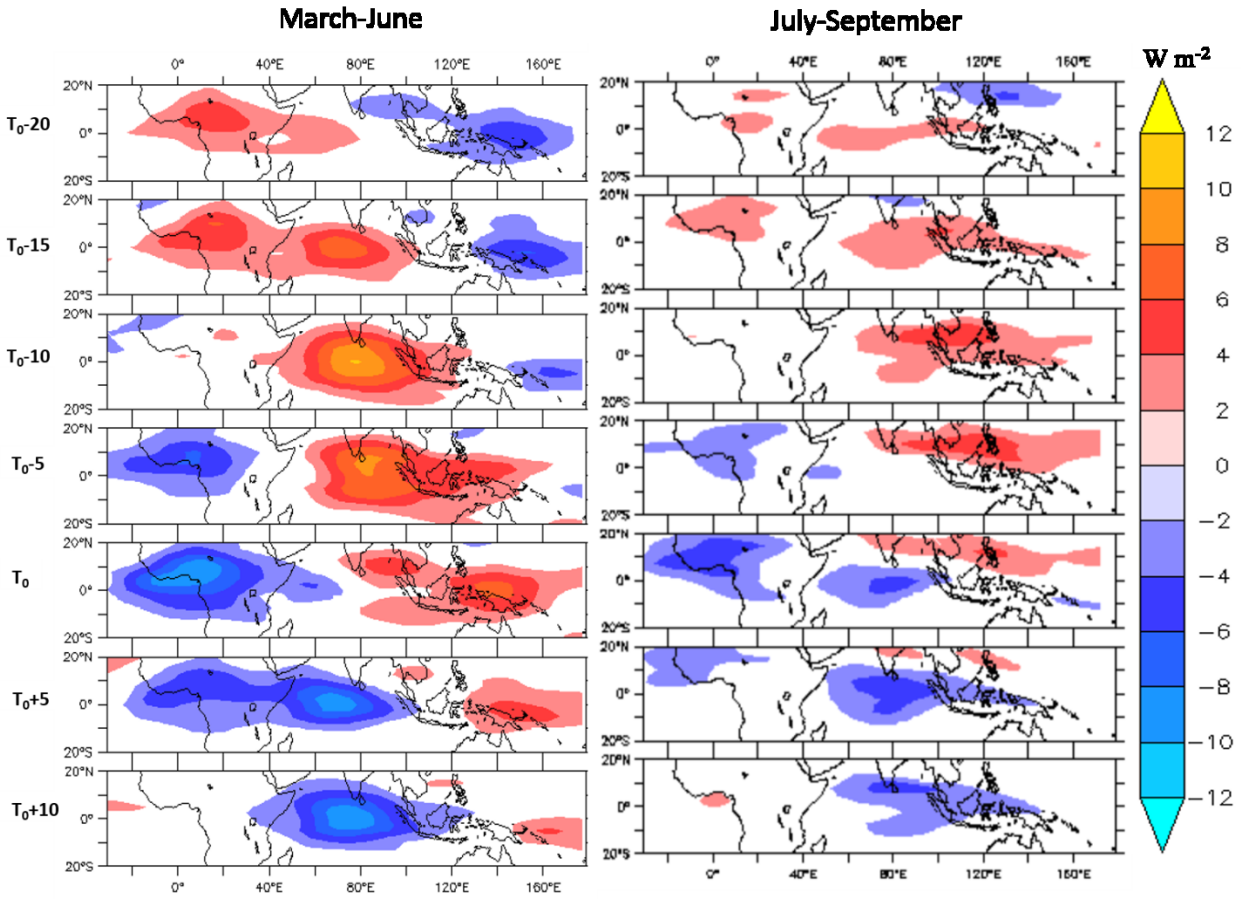

Figure 4.13. Regression of PC-EOF1 against time-lagged sum of MJO-, Rossby-, and Kelvin-filtered OLR for 1980-2013. (left panel) MAMJ, (right panel) JAS. This regression sequence is shown from T_0 -20 to T_0+10, as in Figures 8-11. Shading indicates values significant at the 90% confidence level.

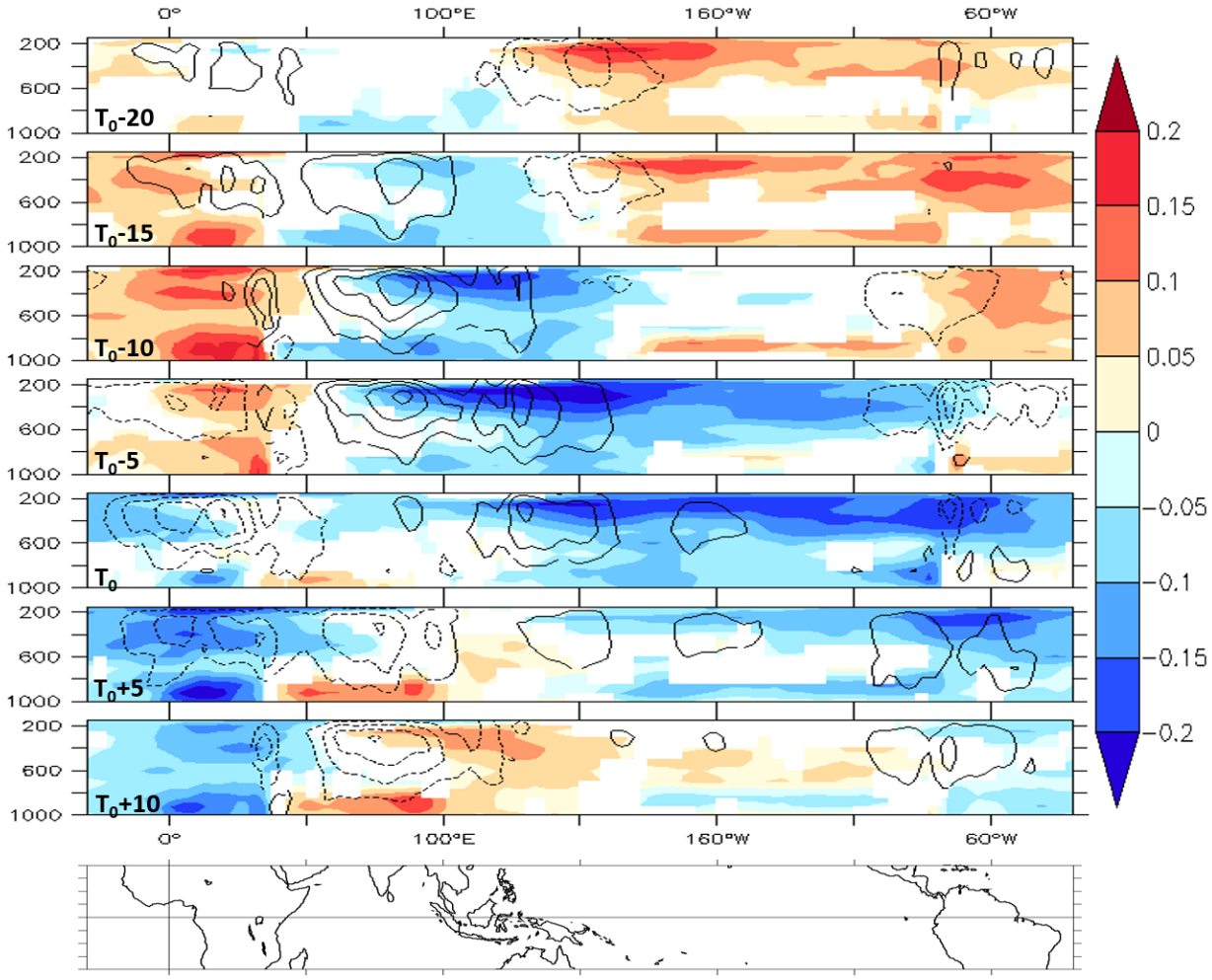

Figure 4.14. Regression of PC-EOF1 against time-lagged unfiltered tropospheric temperature (colors; units are degrees K) and Omega (contours, interval is 0.005 Pa S^{-1}), averaged between 10^0S to 10^0N, for MAMJ 1980-2013. This regression sequence is shown from T_0 -20 to T_0+10 days, as in Figures 4.9-4.13. Shading and contours indicate values significant at the 90% confidence level. Bottom plot shows the world map between 20^0N and 20^0S.

In the boreal summer, Lavender and Matthews (2009) found MJO-associated diabatic heating (cooling) anomalies over the warm pool result in positive (negative) mid-tropospheric temperature anomalies that propagate to West Africa by dry Kelvin and Rossby waves and stabilize

(destabilize) the troposphere over West Africa resulting in enhanced subsidence (ascent). However, in the spring rainy season, the anomalies in convection are already strong before the temperature anomalies reach the region (Gu 2009; Figure 14). At T_0-5, we observe from Figure 4.14 that there is already significant anomalous upward vertical motion and Figures 4.8 and 4.12 also show significant anomalous OLR anomaly at T_0-5, which is consistent with the regression field of omega at T_0-5 (Figure 4.14). This suggests that the tropospheric temperature anomalies that propagate to the region have a relatively small effect on the relationship between the MJO and EWA convection in this season.

It is known that the MJO undergoes strong interannual and intraseasonal variability in strength and location (e.g., Hendon and Salby 1994; Zhang 2005). For this reason, we further investigate the evolution of the MJO influence on EWA convection on a month-by-month basis within both seasons. As shown in Figure 4.15, in MAMJ, MJO impacts on EWA OLR are strongest in March and decrease as the season progresses. The composite field of omega exhibits a similar pattern (not shown). This tendency likely reflects the seasonal evolution of the MJO. By June, the MJO shows northeastward migration in the Indian basin (Figures 4.15G and 4.15H) that is consistent with the link between MJO activity and the Indian Monsoon noted in previous studies (e.g., Lawrence and Webster 2002). The Indian Monsoon, in turn, has the potential to modulate West African convection, but the mechanisms of these teleconnections require their own, independent analysis (Janicot et al. 2009). In the JAS season, however, MJO impacts on EWA do not exhibit clear differences from month to month as they do in the spring rainy season (not shown).

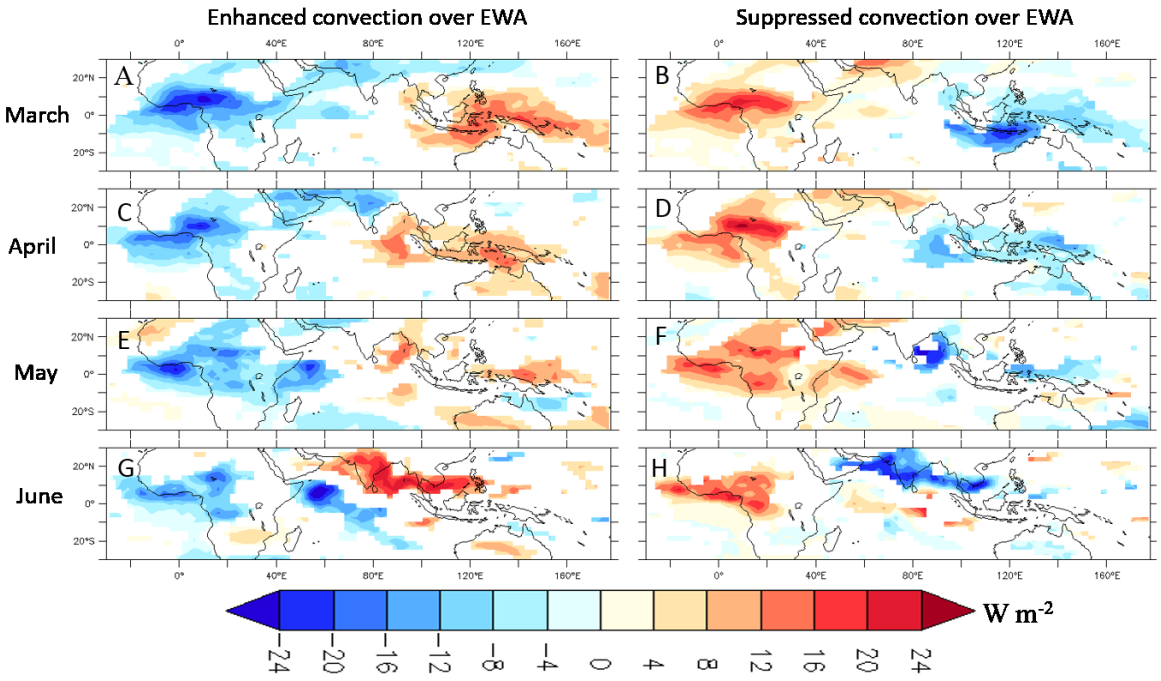

Figure 4.15. Composites of unfiltered OLR (W m^{-2}). (A,B) March, (C,D) April, (E,F) May and (G,H) June using PC-EOF1 time series (A,C,E,G) PC-EOF1 > 1σ and (B,D,F,H) PC-EOF1 < -1σ.

4.3.c. MJO impacts on precipitation extremes

To investigate the impacts of the MJO on precipitation distribution over EWA, we first divide EWA into relatively homogenous regions and then analyze rainfall relationships with the MJO in each region separately. As shown in Figure 4.16, the MJO has strong influences on precipitation extremes in the spring rainy season. Moreover, in the spring rainy season, the influence of the MJO on extremes differs systematically between the two regions shown in Figure 4.1C. The enhanced phase of the MJO increases probability of increased precipitation over region R2 as shown in Figure 4.16A. In contrast, the suppressed phase mainly suppresses precipitation over region R1 (Figure. 4.16B). In region R2, the enhanced phase of the MJO increases daily rainfall by 41% but the suppressed phase of the MJO reduces daily average rainfall by only 15% (Figure. 4.16A).

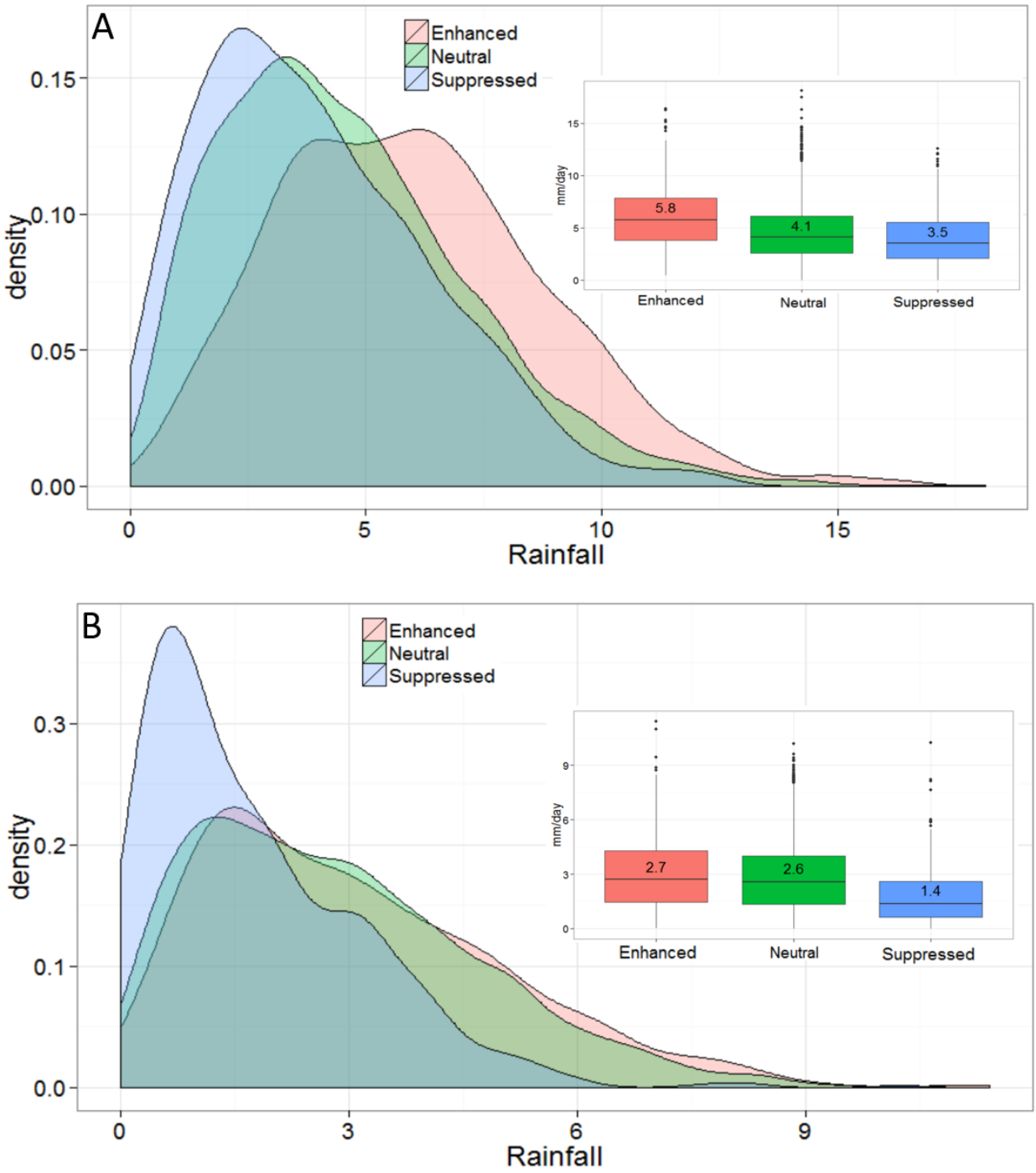

Figure 4.16. Distribution and box plots of precipitation during enhanced-, suppressed- and non-MJO days for the homogenous regions shown in Figure 4.1C. (A) for region R1 in Figure 4.1C (B) for region R2 in Figure 4.1C.

On the other hand, over region R1, we observe from the box plot in Figure 4.16B that the suppressed phase of the MJO decreases daily rainfall by 46%, while the enhanced phase of the MJO increases rainfall over the region by only 4%. In JAS such differences are not observed (not shown). The results in Figure 4.16 suggest that the MJO has important implications for precipitation extremes and prediction of flash floods and droughts in MAMJ. Moreover, while the enhanced phase of the MJO is more important over region R2, the suppressed phase of the MJO is more important over region R1. This shows that the enhanced phase of the MJO can have stronger impacts in some regions and the suppressed phase may be of more importance in other regions. We performed the same evaluation for JAS—regionalization followed by analysis of precipitation extremes—and found no MJO impacts on rainfall extremes in that season. Previous studies have found that the MJO influences the African easterly Jet (Matthews 2004; Lavender and Matthews, 2009) and African easterly waves (Ventrice et al. 2011) in boreal summer. Analyzing the MJO's impacts on and interactions with synoptic and regional systems in the spring rainy season can help to better understand why EWA responds differently to the MJO in spring and summer and why MJO has different impacts on precipitation extremes in different regions within EWA.

4.4. Conclusions

This study examined mechanisms of MJO influence on spring rainy season (March-June) convection in EWA. It also compared the strength of the impacts of the MJO over EWA in the spring rainy season and in boreal summer. To that end, wavenumber-frequency spectral analysis was employed to isolate the influences of the MJO convective center and of Rossby and Kelvin waves triggered by MJO activity in the Eastern Hemisphere. The analysis shows that the primary

mechanism of MJO impact on EWA in March-June is the eastward migration of the MJO convective center into the region. This convective center modulates low level westerlies, which advect moisture from the Gulf of Guinea and the eastern Atlantic Ocean to the region. In MAMJ, when the MJO convective envelope moves to the maritime continent, EWA experiences low level divergent winds and enhanced subsidence. As a result, in this phase anomalous dryness prevails over EWA.

In addition, in MAMJ, MJO anomalies over the Indian Ocean excite convectively coupled Rossby and Kelvin waves which reach EWA at the same time with the eastward moving MJO convective center. This coincident timing enhances the total MJO impact over the region during the spring rainy season. Our results also suggest that the MJO influence on EWA—both direct and via wave propagation—is stronger during the spring rainy season (March-June) than in boreal summer (July-September). Within the March-June season the influence is strongest in March and weakens as the season progresses. The waning of the MJO influence in late spring and summer is a product of general weakening of MJO dynamics in boreal summer (Hendon and Salby 1994), the competing influence of Indian Monsoon generated teleconnections during the summer months, and evolving atmosphere and SST background conditions in EWA.

We have also shown that the MJO has strong impacts on precipitation distribution over EWA in the spring rainy season. The impact of the MJO on MAMJ precipitation extremes could be useful in predicting flash floods and droughts.

The present study has focused exclusively on characterizing and explaining the influence of MJO on the EWA spring rainy season and comparing the strength of the MJO influences in the spring

and summer seasons. The results, however, have clear implications for long range weather forecasting in the region. First, our results indicate that the MJO has a strong influence on spring rains relative to summer rains, such that applications to forecasting are likely to be more meaningful in the spring season. This is an important point, since most previous studies of the MJO influence on EWA have focused on summer. Second, the analysis shows that anomalous increase (decrease) in MJO-associated convection in the Indian Ocean basin precedes significant reduction (enhancement) of West African convection by approximately two weeks (Figures 4.8 and 4.13). This provides a target time horizon and predictor region for statistical forecast systems, and our analysis of mechanisms of communication can inform development of dynamical forecast models. Third, the fact that MJO activity and EWA precipitation anomalies are associated with two week lead raises the possibility of combining existing predictive models of the MJO, which have useful skill that extends out to about 25 days (Love and Matthews 2009; Seo 2009; Kang and Kim 2010; Rashid et al. 2011; among others) with an EWA-specific model of MJO influence to extend MJO associated rainfall forecast over the region beyond 25 days. At this lead time forecast information has the potential to influence water resource decisions, agriculture management, and disaster response.

Much additional work is required to connect the atmospheric analyses presented in this paper to actionable forecast information. But the utility of incorporating MJO in long range precipitation forecasts has been demonstrated in other regions (e.g., Leroy and Wheeler 2008; Jones et al. 2010; Jones et al. 2011; Johnson et al. 2011), and the magnitude and predictability of the MJO influence on EWA holds significant promise for this application.

5. Chapter 5: Conclusions

Intraseasonal spatiotemporal precipitation variability over tropical Africa has significant impacts on rainfed agriculture, human health, and food and water security, affecting the lives of tens of millions of people. However, there is a paucity of studies that focus on precipitation variability over the region on this time-scale, which is essential for more accurate forecasts and precipitation projections in a changing climate. The thesis was an attempt to understand the dynamics of sub-seasonal precipitation variability over selected regions of tropical Africa particularly the summer rains of the Ethiopian portion of the Blue Nile, the long and short rains of East Africa, and the spring and summer rains over tropical West Africa. Various data sets and statistical analyses techniques were used to investigate the factors that influence rainfall variability at sub-seasonal scale over the regions and seasons mentioned above.

In Chapter 2, I explored sub-seasonal scale drivers and mechanisms of rainfall variability in the Blue Nile river basin. It is found that associations with the TEJ, Pacific modes of variability, and the Indian monsoon are strongest in the late rainy season. July and August, on the other hand, exhibit mixed associations with Pacific/Indian Ocean variability and Atlantic Ocean indices, along with connections to regional pressure patterns and the AEJ. Further, June precipitation is negatively correlated with SLP over the equatorial Atlantic and upper-tropospheric geopotential height. June and July precipitation show little significant correlation with the sea surface temperature over the equatorial Pacific Ocean and hence ENSO cannot be used for rainfall prediction over the region in these months.

In the subsequent chapter, I investigated impacts of the MJO on the long and short rains of East Africa. It is found that MJO influences wet and dry spells over the region during the long and short rains. This influence, however, is found to vary between the beginning, middle and end of each season. Specifically, indices of MJO convection at 70°/80°E and 120°W are strongly associated with precipitation variability across much of EA in the early (March) and late (May) long rainy season and in the middle and late (November-December) short rainy season. In the middle of the long rains (April) the MJO influence is obscured but is evident in lead-time associations, and in the early short rains (October) a different pattern emerges, in which MJO strength at 120°E (10°W) is associated with dry (wet) spells in coastal EA but not the interior.

Chapter 4 explores the various ways through which the MJO influences rainfall over tropical West Africa. It is found that the MJO has a significant impact on convection and precipitation anomalies over the region. This impact is primarily due to the direct influence of the eastward movement of the MJO convective core into EWA, which is associated with westerly low-level wind anomalies that advect moisture from the Atlantic Ocean to the region. In addition, equatorial Rossby and Kelvin waves triggered by MJO convection anomalies over the Indian Ocean have a significant and systematic influence on EWA spring season precipitation, though their impact is smaller than the direct influence of the MJO convective core. The influences of MJO convection and each of the MJO-associated convectively coupled equatorial waves coincide, reaching EWA approximately twenty days after MJO convection initiates in the Indian Ocean. This coincident timing enhances the total MJO impact on the region, and it also implies that MJO events have potential for prediction of regional-scale convection and rainfall anomalies over EWA in this season.

5.1. Future Work

ENSO has significant impacts on rainfall over East Africa in the short rains—El Niño is associated with high rainfall conditions and La Niña with dry conditions (Mutai and Ward, 2000; Philippon et al., 2002; Hastenrath et al. 2004; Ummenhofer et al 2009; Gitau et al. 2014; Figures 5.1 and 5.2). Furthermore, in this season, EA's precipitation is also strongly modulated by the Indian Ocean Dipole (IOD, Saji et al 199). During the positive phase of the IOD—when the SST is anomalously higher over the western Indian Ocean—EA experiences anomalous wetness and sometimes disastrous floods. During the negative phase of the dipole, on the other hand, dryness prevails over EA (Camberlin and Wairoto 1997; Mutai et al. 1998; Saji et al. 1999). However, not all ENSO and IOD events are associated with significant precipitation anomalies over EA (e.g., Goddard and Graham 1999; Latif et al. 1999; Black et al. 2003).

In chapter 3, I demonstrated that the MJO modulates intraseasonal precipitation anomalies over both the interior highlands and coastal zones of East Africa (EA) during the short rains. Since ENSO and IOD modulate the characteristics of the MJO, and the background states through which the MJO propagates (Roundy et al., 2010, Figure 5.3), the MJO could be one of the ways ENSO and IOD communicate with EA during the short rains.

Composite analysis shows that the MJO over the Indian Ocean (phases 2 and 3 of the Wheeler and Hendon MJO index) is associated with significant increase in precipitation over EA during El Niño events, as shown in Figures 5.4, 5.5 and 5.6. In La Niña events and non-ENSO years, the MJO over the Indian Ocean has very week impacts on EA's convection and precipitation (Figures 5.4D, 5.4E, 5.5D, 5.5E and 5.6). It is also worth noting that, although previous studies

have found that El Niño/ La Niña events are associated with anomalous wetness/dryness over EA, the associations are very weak in the absence of the MJO (Figures 5.4 and 5.5).

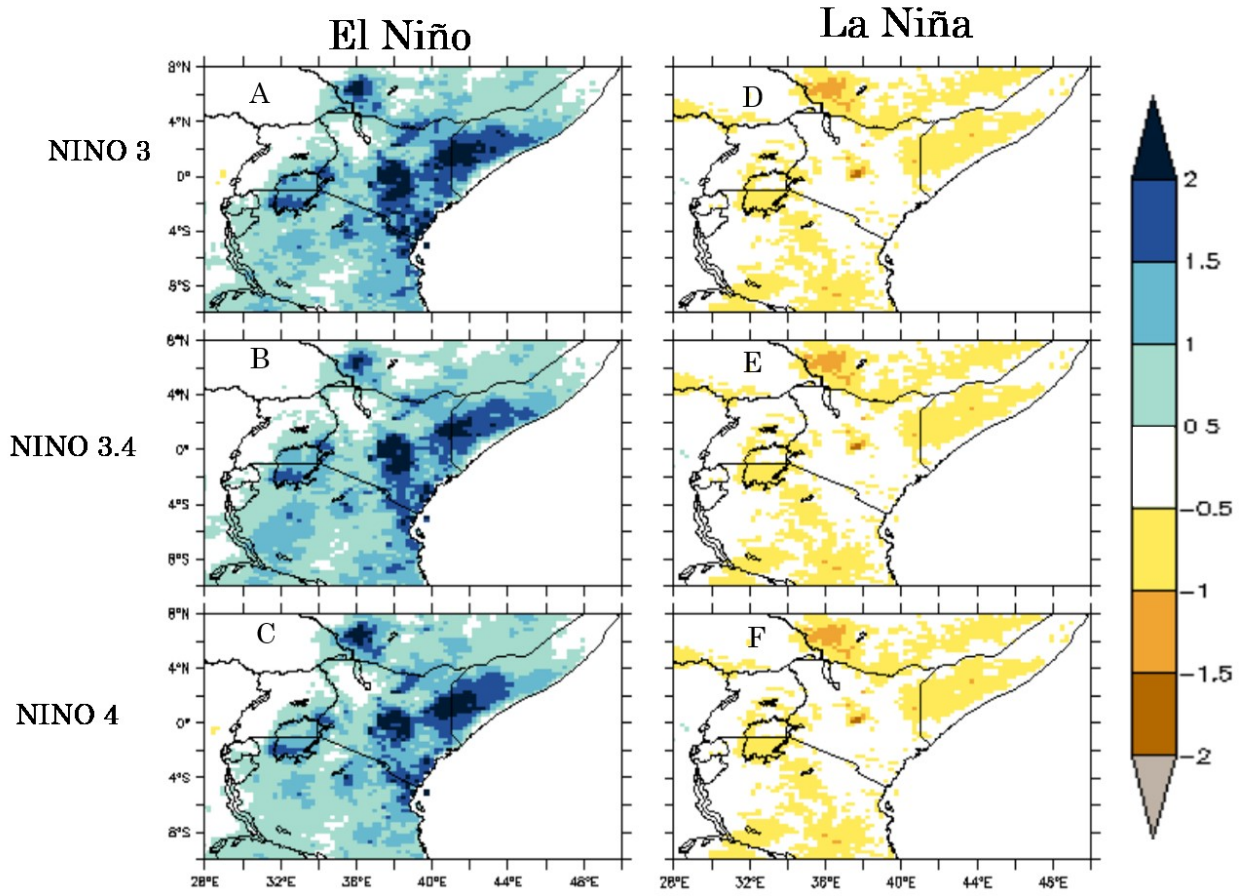

Figure 5.1. Composites of October-December CHIRPS rainfall over East Africa. (Left) based on El Niño, (Right) based on La Niña. (A), (D) using NINO3, (B),(E) based on NINO3.4 and (C) and (F) based on NINO4.

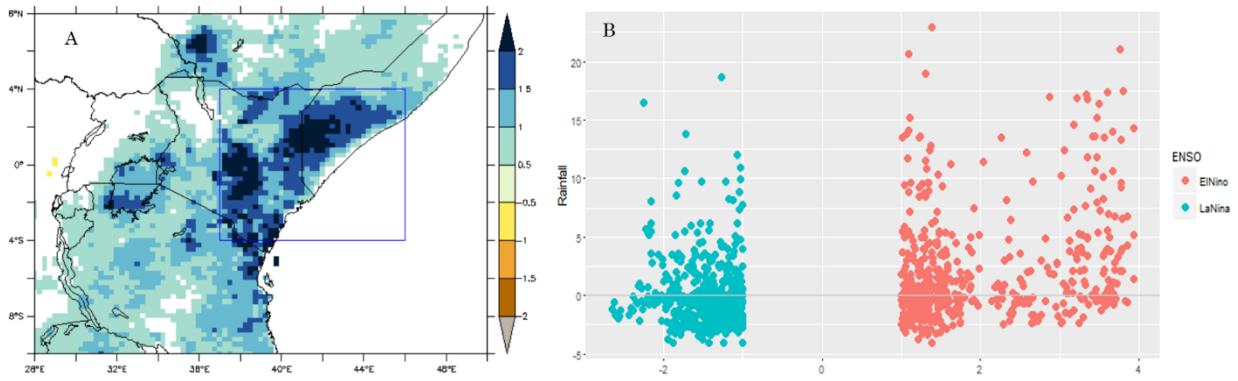

Figure 5.2. Composites of CHIRPS rainfall (mm/day) based on NINO3 ENSO index. The rectangular region shown in (A) is used to calculate area average composites in (B).

Similarly, the IOD exhibits strong associations with EA's precipitation when there is strong MJO over the Indian Ocean. During the positive phase of the IOD, the MJO over the Indian Ocean has impacts that extend to EA. In the absence of the MJO, however, the IOD shows very weak associations with precipitation over EA (not shown).

Furthermore, there are more MJO days in the Indian Ocean during El Niño and positive IOD events (Figure 5.3) which implies stronger impacts on EA's rainfall. During La Niña events, on the other hand, more MJO days are observed in the Pacific Ocean. Since MJO convection over the Pacific Ocean is associated with subsidence over the western Indian Ocean, the MJO over the Pacific Ocean during La Niña events is associated with dryness anomalies over EA (Figures 5.4 and 5.5).

When the MJO is in the Indian Ocean during El Niño events, the center of negative SLP moves further west to the western Indian Ocean and coastal EA (Figure 5.7). Associated with this

pattern, there are strong near surface easterly anomalies over the Indian Ocean (Figure 5.7). This winds are a reversal and weakening of the walker circulation in the Indian Ocean. These winds advect moisture to EA and increase convection and precipitation over the region. As we can see from Figure 5.8, When the MJO is in the Indian Ocean during El Niño events, there is anomalous upward vertical motion over EA which is consistent with the SLP and near surface wind composites. This is consistent with previous studies that find that lower tropospheric easterlies over the Indian Ocean are associated with wetness and sometimes with disastrous floods over EA (e.g., Hastenrath et al., 2010).

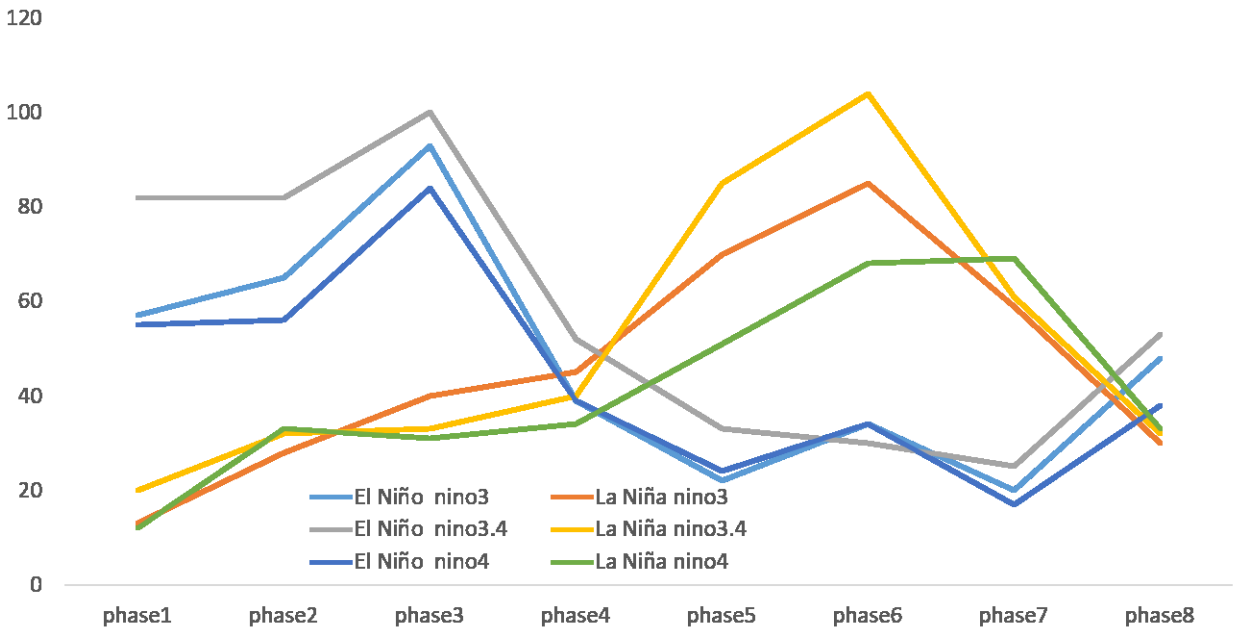

Figure 5.3. Number of strong MJO days in each phase El Niño and La Niña based on RMM

Exploring the dynamics, by employing detailed data analysis and modeling, of the interactions of the MJO, ENSO and IOD and how these interactions influence rainfall over EA can help for more accurate predictions of dry and wet spells and to cope with the disastrous floods over the region. Further, understanding the impacts of the interactions of the MJO, ENSO and IOD on EA precipitation can help to get a better understanding of how climate change may impact the region.

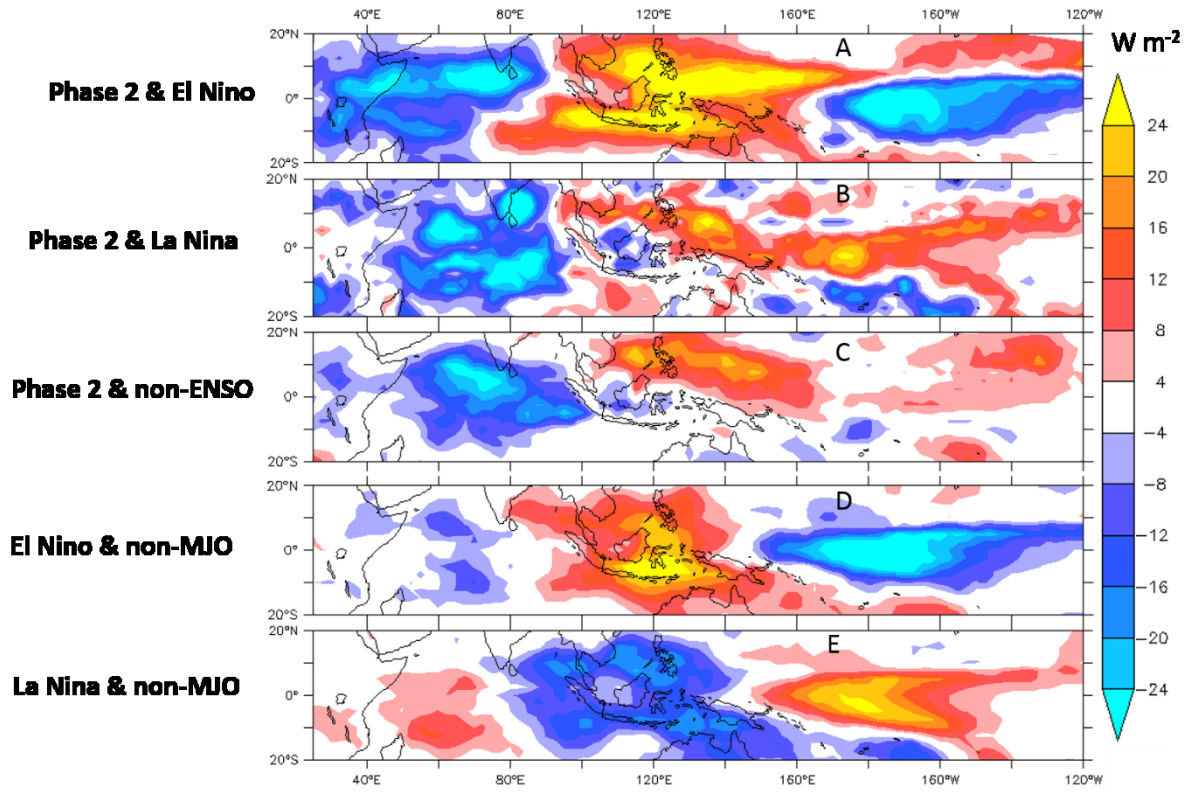

Figure 5.4. Composites of 1982-2013 OND OLR during (A) El Niño events and phase 2 of the MJO (b) La Niña events and phase 2 of the MJO (C) Phase 2 of the MJO and non-ENSO (C) El Niño and non-MJO events and (D) La Niña and non-MJO events.

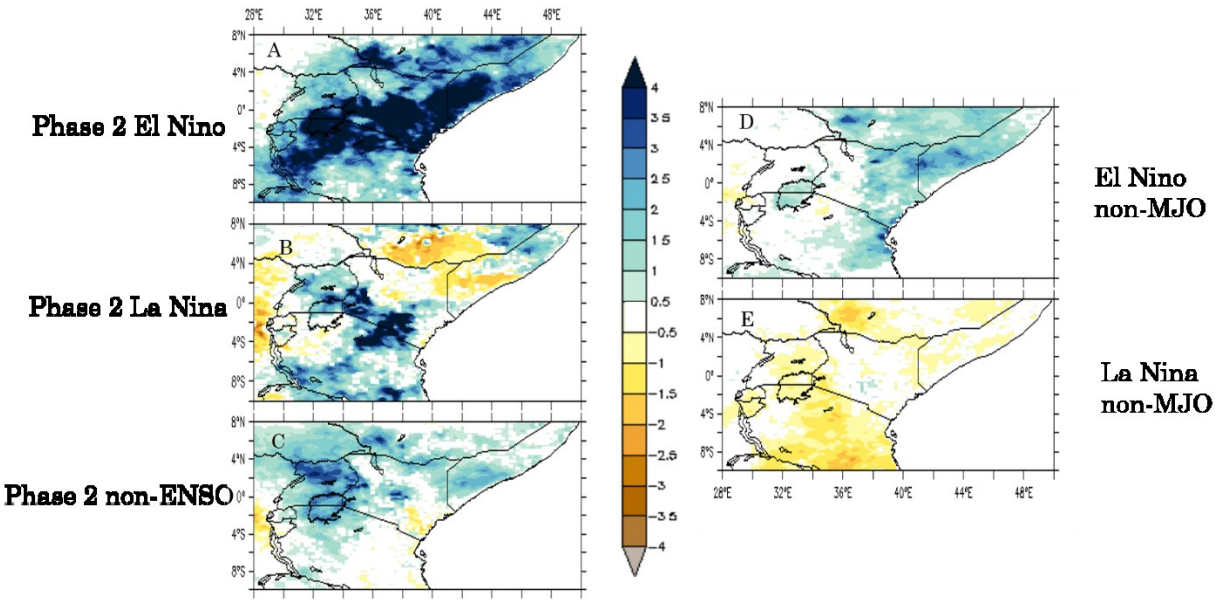

Figure 5.5. Composites of short rain CHIRPS rainfall. (A) Phase 2 MJO and El Niño, (B) Phase 2 MJO and La Niña, (c) phase 2 MJO and non-ENSO, (D) El Niño and non-MJO and (E) La Niña and non-MJO

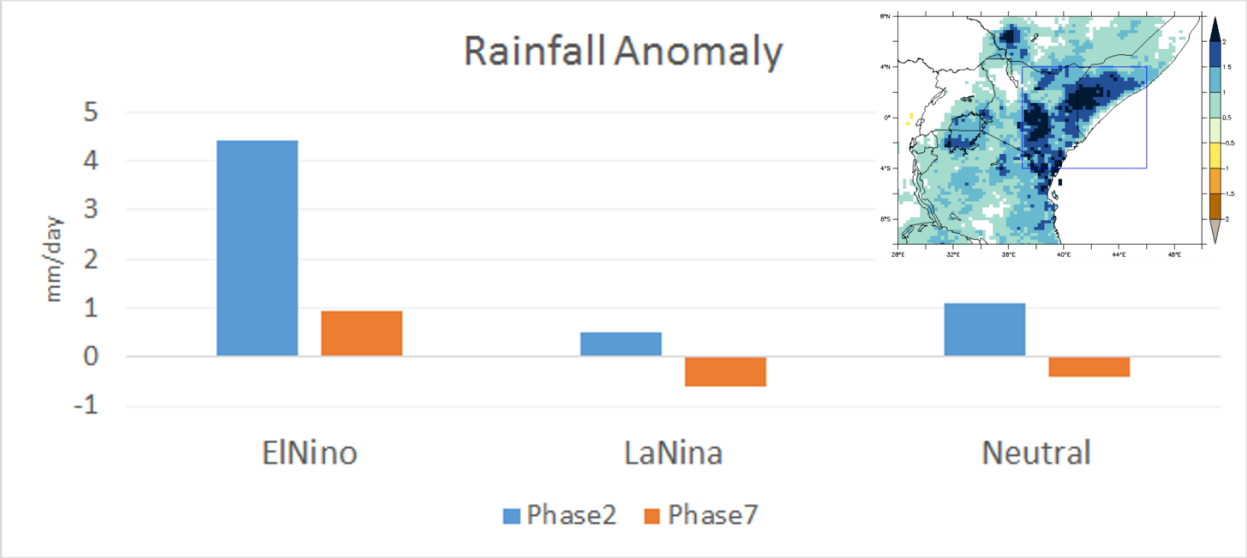

Figure 5.6. Composites of CHIRPS rainfall based on MJO and ENSO. The rectangular region shown on the top right is used to calculate area average composites.

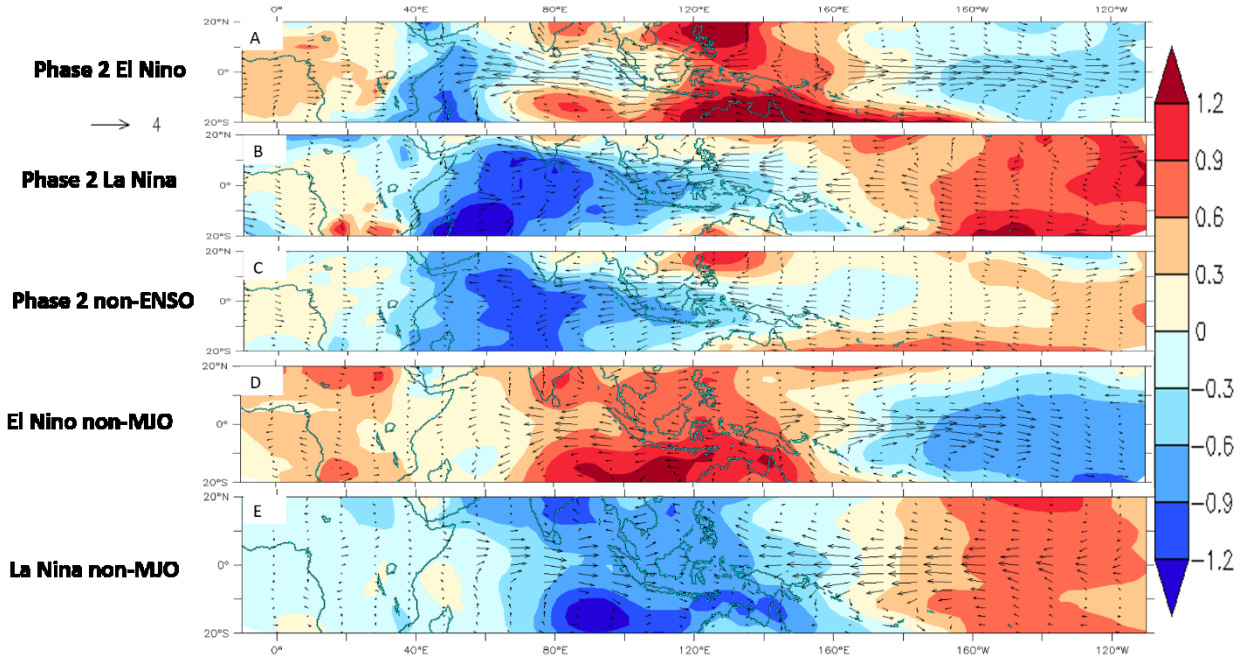

Figure 5.7. Composites of sea level pressure (hPa) and wind vectors at 850 hPa based on MJO and ENSO.

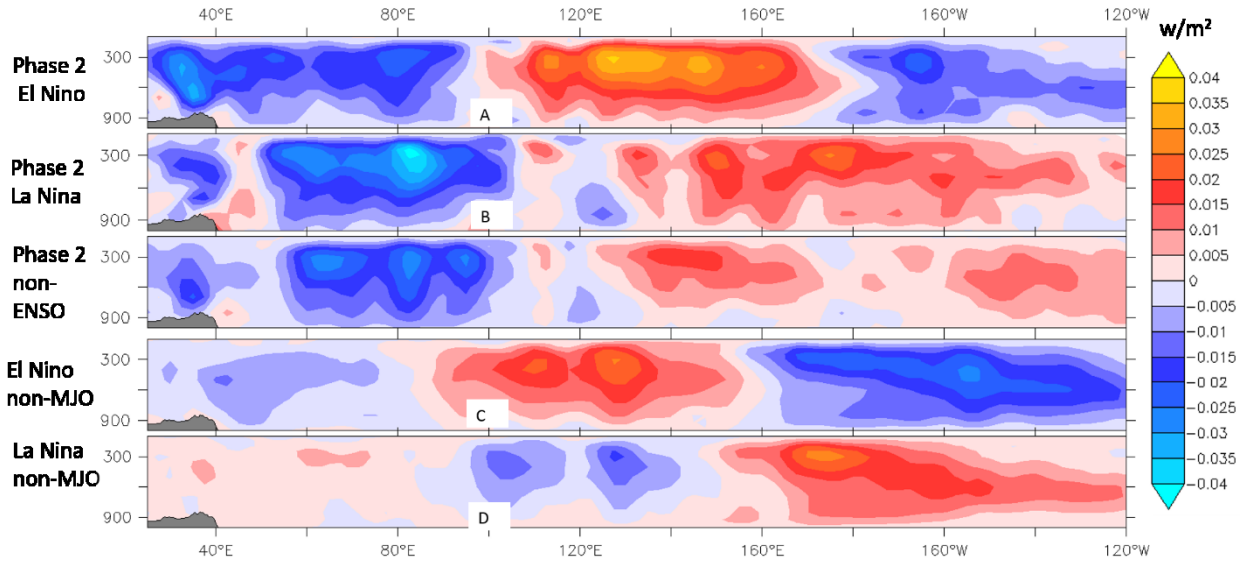

Figure 5.8. Composites of October-December vertical velocity (w/m^2) averaged from 10^{0}S to 10^{0}N based on MJO and ENSO.

REFERENCES

Abtew, W., A. M. Melesse, and T. Dessalegne, 2009: El Ni˜no Southern Oscillation link to the Blue Nile River Basin hydrology. *Hydrological Processes*, **23,** 3653-3660.

Anyah, R. O., and W. Qiu, 2012: Characteristic 20th and 21st century precipitation and temperature patterns and changes over the Greater Horn of Africa. *International Journal of Climatology*, **32,** 347-363.

Asnani, G. C., 1993: *Tropical meteorology.* GC Asnani.

——, 2005: Tropical Meteorology, vols. 1-3, Indian Inst. of Trop. *Meteorol., Pashan, India*.

Badr, H., B. Zaitchik, and A. Dezfuli, 2015: A tool for hierarchical climate regionalization. *Earth Sci Inform***,** 1-10.

Badr, H. S., B. F. Zaitchik, and A. K. Dezfuli, 2014: Hierarchical Climate Regionalization. CRAN, http://cran.r-project.org/package=HiClimR.

Barlow, M., and D. Salstein, 2006: Summertime influence of the Madden-Julian Oscillation on daily rainfall over Mexico and Central America. *Geophysical research letters*, **33**.

Barlow, M., M. Wheeler, B. Lyon, and H. Cullen, 2005: Modulation of daily precipitation over southwest Asia by the Madden-Julian oscillation. *Monthly Weather Review*, **133,** 3579-3594.

Barrett, B. S., and L. M. Leslie, 2009: Links between tropical cyclone activity and Madden-Julian Oscillation phase in the North Atlantic and northeast Pacific basins. *Monthly Weather Review*, **137,** 727-744.

Bastiaanssen, W. G., P. Karimi, L.-M. Rebelo, Z. Duan, G. Senay, L. Muthuwatte, and V. Smakhtin, 2014: Earth observation based assessment of the water production and water consumption of Nile basin agro-ecosystems. *Remote Sens.*, **6,** 10306-10334.

Behera, S., R. Krishnan, and T. Yamagata, 1999: Unusual ocean-atmosphere conditions in the tropical Indian Ocean during 1994. *Geophys. Res. Lett.*, **26,** 3001-3004.

Berhane, F., and B. Zaitchik, 2014: Modulation of Daily Precipitation over East Africa by the Madden–Julian Oscillation. *Journal of Climate*, **27,** 6016-6034.

Berhane, F., B. Zaitchik, and A. Dezfuli, 2013: Sub-seasonal analysis of precipitation variability in the Blue Nile River basin. *Journal of climate*, **27,** 325-344.

Berhane, F., B. Zaitchik, and H. Badr, 2015: The Madden-Julian Oscillation's influence on Spring Precipitation over Equatorial West Africa. *Journal of Climate*.

Beyene, T., D. P. Lettenmaier, and P. Kabat, 2010: Hydrologic impacts of climate change on the Nile River Basin: implications of the 2007 IPCC scenarios. *Climatic change*, **100,** 433-461.

Black, E., 2005a: The relationship between Indian Ocean seaâ€“surface temperature and East African rainfall. *Philosophical Transactions of the Royal Society A: Mathematical, Physical and Engineering Sciences*, **363,** 43-47.

——, 2005b: The relationship between Indian Ocean sea-surface temperature and East African rainfall. *Philosophical Transactions of the Royal Society A: Mathematical, Physical and Engineering Sciences*, **363,** 43-47.

Black, E., J. Slingo, and K. R. Sperber, 2003: An observational study of the relationship between excessively strong short rains in coastal East Africa and Indian Ocean SST. *Monthly Weather Review*, **131,** 74-94.

Block, P., and B. Rajagopalan, 2007: Interannual variability and ensemble forecast of Upper Blue Nile Basin Kiremt season precipitation. *Journal of Hydrometeorology*, **8,** 327-343.

Bowden, J. H., and F. H. M. Semazzi, 2007: Empirical analysis of intraseasonal climate variability over the Greater Horn of Africa. *Journal of Climate*, **20,** 5715-5731.

Camberlin, P., 1995: June-september rainfall in north-eastern Africa and atmospheric signals over the tropics: A zonal perspective. *International Journal of Climatology*, **15,** 773-783.

Camberlin, P., and J. G. Wairoto, 1997: Intraseasonal wind anomalies related to wet and dry spells during the "long" and "short" rainy seasons in Kenya. *Theoretical and applied climatology*, **58,** 57-69.

Camberlin, P., and N. Philippon, 2002: The East African March-May rainy season: Associated atmospheric dynamics and predictability over the 1968-97 period. *Journal of Climate*, **15,** 1002-1019.

Camberlin, P., and R. E. Okoola, 2003: The onset and cessation of the "long rains" in eastern Africa and their interannual variability. *Theoretical and applied climatology*, **75,** 43-54.

Camberlin, P., B. Fontaine, S. Louvet, P. Oettli, and P. Valimba, 2009: Climate Adjustments over Africa Accompanying the Indian Monsoon Onset. *Journal of Climate*, **23,** 2047-2064.

Carvalho, L. M. V., C. Jones, and B. Liebmann, 2004: The South Atlantic convergence zone: Intensity, form, persistence, and relationships with intraseasonal to interannual activity and extreme rainfall. *Journal of climate*, **17,** 88-108.

Cattell, R. B., 1966: The scree test for the number of factors. *Multivariate behavioral research*, **1,** 245-276.

Chen, Y., and A. D. Del Genio, 2009: Evaluation of tropical cloud regimes in observations and a general circulation model. *Climate Dynamics*, **32,** 355-369.

Conway, D., 1997: A water balance model of the Upper Blue Nile in Ethiopia. *Hydrological Sciences Journal*, **42,** 265-286.

——, 2000: The climate and hydrology of the Upper Blue Nile River. *The Geographical Journal*, **166,** 49-62.

Conway, D., and M. Hulme, 1993: Recent fluctuations in precipitation and runoff over the Nile sub-basins and their impact on main Nile discharge. *Climatic Change*, **25,** 127-151.

Conway, D., E. Allison, R. Felstead, and M. Goulden, 2005: Rainfall variability in East Africa: implications for natural resources management and livelihoods. *Philosophical Transactions of the Royal Society A: Mathematical, Physical and Engineering Sciences*, **363,** 49-54.

Cook, K. H., and E. K. Vizy, 2013: Projected Changes in East African Rainy Seasons. *Journal of Climate*.

Dee, D. P., and Coauthors, 2011: The ERA-Interim reanalysis: Configuration and performance of the data assimilation system. *Quarterly Journal of the Royal Meteorological Society*, **137,** 553-597.

Del Genio, A. D., Y. Chen, D. Kim, and M.-S. Yao, 2012: The MJO transition from shallow to deep convection in CloudSat/CALIPSO data and GISS GCM simulations. *Journal of Climate*, **25,** 3755-3770.

Dezfuli, A. K., and S. E. Nicholson, 2012: The Relationship of Rainfall Variability in Western Equatorial Africa to the Tropical Oceans and Atmospheric Circulation. Part II: The Boreal Autumn. *Journal of Climate*, **26,** 66-84.

Dinku, T., P. Ceccato, E. Grover-Kopec, M. Lemma, S. Connor, and C. Ropelewski, 2007: Validation of satellite rainfall products over East Africa's complex topography. *International Journal of Remote Sensing*, **28,** 1503-1526.

Diro, G. T., D. I. F. Grimes, and E. Black, 2011: Teleconnections between Ethiopian summer rainfall and sea surface temperature: part I-observation and modelling. *Climate dynamics*, **37,** 103-119.

Donald, A., and Coauthors, 2006: Near-global impact of the Madden-Julian Oscillation on rainfall. *Geophysical Research Letters*, **33,** L09704.

Epstein, P. R., 1999: Climate and health. *Science*, **285,** 347-348.

Eugène, K. K., G. B. T. Albert, and K. A. Michel, 2012: Analyze of climate variability and change impacts on hydro-climate parameters: case study of Côte d'Ivoire. *IJSER*, **3**.

Flohn, H., 1987: Rainfall teleconnections in northern and northeastern Africa. *Theoretical and applied climatology*, **38,** 191-197.

Funk, C., M. D. Dettinger, J. C. Michaelsen, J. P. Verdin, M. E. Brown, M. Barlow, and A. Hoell, 2008: Warming of the Indian Ocean threatens eastern and southern African food security but could be mitigated by agricultural development. *Proceedings of the National Academy of Sciences*, **105,** 11081-11086.

Funk, C., and Coauthors, 2005: Recent drought tendencies in Ethiopia and equatorial-subtropical eastern Africa. *Famine Early Warning System Network, USAID, Washington, DC*.

Funk, C. C., and Coauthors, 2014: A quasi-global precipitation time series for drought monitoring: U.S. Geological Survey Data Series 832, 4 p., http://dx.doi.org/10.3133/ds832.

Gadgil, S., 2003: The Indian monsoon and its variability. *Annu. Rev. Earth Planet. Sci.*, **31,** 429-467.

Gadgil, S., and S. P. Rao, 2000: Farming strategies for a variable climate-A Challenge. *Current science*, **78,** 1203-1215.

Gill, A. E., 1980: Some simple solutions for heat-induced tropical circulation. *Quarterly Journal of the Royal Meteorological Society*, **106,** 447-462.

Gissila, T., E. Black, D. I. F. Grimes, and J. M. Slingo, 2004: Seasonal forecasting of the Ethiopian summer rains. *International journal of climatology*, **24,** 1345-1358.

Gitau, W., 2011: Diagnosis and predictability of intraseasonal characteristics of wet and dry spells over equatorial east Africa, University of Nairobi, Kenya.

Gitau, W., P. Camberlin, L. Ogallo, and R. Okoola, 2014: Oceanic and atmospheric linkages with short rainfall season intraseasonal statistics over Equatorial Eastern Africa and their predictive potential. *International Journal of Climatology*.

Goddard, L., and N. E. Graham, 1999: Importance of the Indian Ocean for simulating rainfall anomalies over eastern and southern Africa. *Journal of Geophysical Research: Atmospheres (1984â€“2012)*, **104,** 19099-19116.

Gu, G., 2009: Intraseasonal variability in the equatorial Atlantic-West Africa during March–June. *Climate Dyn.*, **32,** 457-471.

Hastenrath, S., 2007: Circulation mechanisms of climate anomalies in East Africa and the equatorial Indian Ocean. *Dynamics of Atmospheres and Oceans*, **43,** 25-35.

Hastenrath, S., D. Polzin, and P. Camberlin, 2004: Exploring the predictability of the 'Short Rains' at the coast of East Africa. *International journal of climatology*, **24,** 1333-1343.

Hastenrath, S., D. Polzin, and C. Mutai, 2007: Diagnosing the 2005 drought in equatorial East Africa. *Journal of Climate*, **20,** 4628-4637.

Hendon, H. H., and M. L. Salby, 1994: The life cycle of the Madden-Julian oscillation. *Journal of the Atmospheric Sciences*, **51,** 2225-2225.

Herrmann, S. M., and K. I. Mohr, 2011: A continental-scale classification of rainfall seasonality regimes in Africa based on gridded precipitation and land surface temperature products. *Journal of Applied Meteorology and Climatology*, **50,** 2504-2513.

Hidayat, R., and S. Kizu, 2010: Influence of the Madden-Julian Oscillation on Indonesian rainfall variability in austral summer. *International Journal of Climatology*, **30,** 1816-1825.

Higgins, R. W., and W. Shi, 2001: Intercomparison of the principal modes of interannual and intraseasonal variability of the North American monsoon system. *Journal of climate*, **14,** 403-417.

Huffman, G. J., and D. T. Bolvin, 2013: GPCP Version 2.2 SG Combined Precipitation Data Set Documentation. Available online at: ftp://precip.gsfc.nasa.gov/pub/gpcp-v2.2/doc/V2.2_doc.pdf.

Huffman, G. J., R. F. Adler, D. T. Bolvin, E. J. Nelkin, F. Hossain, and M. Gebremichael, 2010: The TRMM multi-satellite precipitation analysis (TMPA). *Satellite rainfall applications for surface hydrology*, 3-22.

Indeje, Semazzi, and Ogallo, 2000: ENSO signals in East African Rainfall and their prediction potentials. *Int. J. Climatol. 20, 19 – 46.*

Indeje, M., and F. H. M. Semazzi, 2000: Relationships between QBO in the lower equatorial stratospheric zonal winds and East African seasonal rainfall. *Meteorology and Atmospheric Physics*, **73,** 227-244.

Jackson, B., S. E. Nicholson, and D. Klotter, 2009: Mesoscale convective systems over western equatorial Africa and their relationship to large-scale circulation. *Monthly Weather Review*, **137,** 1272-1294.

Janicot, S., and B. Sultan, 2001: Intra-seasonal modulation of convection in the West African Monsoon. *Geophysical Research Letters*, **28,** 523-526.

Janicot, S., F. Mounier, N. M. J. Hall, S. p. Leroux, B. Sultan, and G. N. Kiladis, 2009: Dynamics of the west african monsoon. Part IV: analysis of 25-90-day variability of convection and the role of the indian monsoon. *Journal of Climate*, **22,** 1541-1565.

Jeong, J.-H., B.-M. Kim, C.-H. Ho, and Y.-H. Noh, 2008: Systematic variation in wintertime precipitation in East Asia by MJO-induced extratropical vertical motion. *Journal of climate*, **21,** 788-801.

Jiang, X., D. E. Waliser, M. C. Wheeler, C. Jones, M.-I. Lee, and S. D. Schubert, 2008: Assessing the Skill of an All-Season Statistical Forecast Model for the Madden-Julian Oscillation. *Monthly Weather Review*, **136,** 1940-1956.

Johnson, N., E. Riddle, M. Stoner, S. Feldstein, D. Collins, and M. L'Heureux, 2011: Toward a Framework for Incorporating MJO and ENSO Information into CPC Probabilistic Extended Range Forecasts. Science and Technology Infusion Climate Bulletin, NOAA's National Weather Service 36th NOAA Annual Climate Diagnostics and Prediction Workshop, Fort Worth, TX,7 pp.

Jones, C., 2000: Occurrence of extreme precipitation events in California and relationships with the Madden-Julian oscillation. *Journal of climate*, **13,** 3576-3587.

Jones, C., D. E. Waliser, K. M. Lau, and W. Stern, 2004: Global occurrences of extreme precipitation and the Madden-Julian Oscillation: Observations and predictability. *Journal of climate*, **17,** 4575-4589.

Jones, C., J. Gottschalck, L. M. V. Carvalho, and W. Higgins, 2010: Influence of the Madden–Julian Oscillation on Forecasts of Extreme Precipitation in the Contiguous United States. *Monthly Weather Review*, **139,** 332-350.

Jones, C., L. M. V. Carvalho, J. Gottschalck, and W. Higgins, 2011: The Madden–Julian Oscillation and the Relative Value of Deterministic Forecasts of Extreme Precipitation in the Contiguous United States. *Journal of Climate*, **24,** 2421-2428.

Jury, M. R., 2010: Ethiopian decadal climate variability. *Theoretical and Applied Climatology*, **101,** 29-40.

Kalnay, E., and Coauthors, 1996: The NCEP/NCAR 40-year reanalysis project. *Bulletin of the American Meteorological Society*, **77,** 437-471.

Kanamitsu, M., W. Ebisuzaki, J. Woollen, S.-K. Yang, J. J. Hnilo, M. Fiorino, and G. L. Potter, 2002: Ncep-doe amip-ii reanalysis (r-2). *Bulletin of the American Meteorological Society*, **83,** 1631-1644.

Kang, I.-S., and H.-M. Kim, 2010: Assessment of MJO Predictability for Boreal Winter with Various Statistical and Dynamical Models. *Journal of Climate*, **23,** 2368-2378.

Kiladis, G. N., M. C. Wheeler, P. T. Haertel, K. H. Straub, and P. E. Roundy, 2009: Convectively coupled equatorial waves. *Rev. Geophys*, **47**.

Kiladis, G. N., and Coauthors, 2013: A comparison of OLR and circulation based indices for tracking the MJO. *Monthly Weather Review*.

Korecha, D., and A. G. Barnston, 2007: Predictability of June-September rainfall in Ethiopia. *Monthly weather review*, **135,** 628-650.

Krauer, J., 1988: *Rainfall, erosivity & isoerodent map of Ethiopia.* Vol. 15, University of Berne.

Lavender, S. L., and A. J. Matthews, 2009: Response of the West African monsoon to the Madden-Julian oscillation. *Journal of Climate*, **22,** 4097-4116.

Lawrence, D. M., and P. J. Webster, 2002: The boreal summer intraseasonal oscillation: Relationship between northward and eastward movement of convection. *Journal of the atmospheric sciences*, **59,** 1593-1606.

Leroy, A., and M. C. Wheeler, 2008: Statistical Prediction of Weekly Tropical Cyclone Activity in the Southern Hemisphere. *Monthly Weather Review*, **136,** 3637-3654.

Levin, N. E., E. J. Zipser, and T. E. Cerling, 2009: Isotopic composition of waters from Ethiopia and Kenya: Insights into moisture sources for eastern Africa. *Journal of Geophysical Research*, **114,** D23306.

Li, L., and Coauthors, 2009: Evaluation of the real-time TRMM-based multi-satellite precipitation analysis for an operational flood prediction system in Nzoia Basin, Lake Victoria, Africa. *Natural hazards*, **50,** 109-123.

Liebmann, B., and Smith, 1996: Description of a complete (interpolated) outgoing longwave radiation dataset. *Bull. Amer. Meteor. Soc.*, **77,** 1275-1277.

Lin, H., G. Brunet, and J. Derome, 2008: Forecast skill of the Madden-Julian Oscillation in two Canadian atmospheric models. *Monthly Weather Review*, **136,** 4130-4149.

Lorenz, D. J., and D. L. Hartmann, 2006: The Effect of the MJO on the North American Monsoon*. *Journal of climate*, **19,** 333-343.

Love, B. S., and A. J. Matthews, 2009: Real-time localised forecasting of the Madden-Julian Oscillation using neural network models. *Quarterly Journal of the Royal Meteorological Society*, **135,** 1471-1483.

Love, B. S., A. J. Matthews, and G. J. Janacek, 2008: Real-Time Extraction of the Madden-Julian Oscillation Using Empirical Mode Decomposition and Statistical Forecasting with a VARMA Model. *Journal of Climate*, **21,** 5318-5335.

Lyon, B., and D. G. DeWitt, 2012: A recent and abrupt decline in the East African long rains. *Geophysical Research Letters*, **39**.

Madden, R. A., and P. R. Julian, 1971a: Detection of a 40-50 day oscillation in the zonal wind in the tropical Pacific. *J. Atmos. Sci*, **28,** 702-708.

——, 1971b: Detection of a 40â€“50 day oscillation in the zonal wind in the tropical Pacific. *J. Atmos. Sci*, **28,** 702-708.

——, 1972a: Description of global-scale circulation cells in the tropics with a 40â€“50 day period. *J. Atmos. Sci*, **29,** 1109-1123.

——, 1972b: Description of global-scale circulation cells in the tropics with a 40-50 day period. *J. atmos. Sci*, **29,** 1109-1123.

——, 1994: Observations of the 40-50-day tropical oscillation-A review. *Monthly weather review*, **122,** 814-837.

Maharaj, E. A., and M. C. Wheeler, 2005: Forecasting an index of the Madden-oscillation. *International Journal of Climatology*, **25,** 1611-1618.

Maloney, E. D., and J. Shaman, 2008: Intraseasonal variability of the West African monsoon and Atlantic ITCZ. *Journal of Climate*, **21,** 2898-2918.

Matthews, A. J., 2004: Intraseasonal variability over tropical Africa during northern summer. *Journal of climate*, **17,** 2427-2440.

McHugh, M. J., 2004: Near-surface zonal flow and east african precipitation receipt during austral summer. *Journal of climate*, **17,** 4070-4079.

Mohamed, Y. A., B. Van den Hurk, H. H. G. Savenije, and W. G. M. Bastiaanssen, 2005: Hydroclimatology of the Nile: results from a regional climate model. *Hydrology and Earth System Sciences Discussions*, **2,** 319-364.

Mohino, E., S. Janicot, H. Douville, and L. Z. X. Li, 2012: Impact of the Indian part of the summer MJO on West Africa using nudged climate simulations. *Climate dynamics*, **38,** 2319-2334.

Mohino, E., B. Rodríguez-Fonseca, C. Mechoso, S. Gervois, P. Ruti, and F. Chauvin, 2011: Impacts of the Tropical Pacific/Indian Oceans on the Seasonal Cycle of the West African Monsoon. *Journal of Climate*, **24**.

Mutai, C. C., and M. N. Ward, 2000: East African rainfall and the tropical circulation/convection on intraseasonal to interannual timescales. *Journal of climate*, **13,** 3915-3939.

Mutai, C. C., M. N. Ward, and A. W. Colman, 1998: Towards the prediction of the East Africa short rains based on sea-surface temperatureâ€“atmosphere coupling. *International Journal of Climatology*, **18,** 975-997.

Nguyen, H., and J.-P. Duvel, 2008: Synoptic wave perturbations and convective systems over equatorial Africa. *Journal of Climate*, **21,** 6372-6388.

Nguyen, w. a., 2014: Tropical meteorology: Equatorial waves.

Nicholson, S. E., 1996: A review of climate dynamics and climate variability in Eastern Africa. *The limnology, climatology and paleoclimatology of the East African lakes***,** 25-56.

Nicholson, S. E., and J. Kim, 1997a: The relationship of the El NiÃ±o-southern oscillation to African rainfall. *Int. J. Climatol.*, **17,** 117-135.

——, 1997b: The relationship of the El Niño–Southern Oscillation to African rainfall. *International Journal of Climatology*, **17,** 117-135.

Nicholson, S. E., and J. P. Grist, 2001: A conceptual model for understanding rainfall variability in the West African Sahel on interannual and interdecadal timescales. *International Journal of Climatology*, **21,** 1733-1757.

Nicholson, S. E., and A. K. Dezfuli, 2013: The Relationship of Rainfall Variability in Western Equatorial Africa to the Tropical Oceans and Atmospheric Circulation. Part I: The Boreal Spring. *Journal of climate*, **26,** 45-65.

Nnamchi, H. C., and J. Li, 2011: Influence of the South Atlantic Ocean dipole on West African summer precipitation. *Journal of Climate*, **24,** 1184-1197.

North, G. R., T. L. Bell, R. F. Cahalan, and F. J. Moeng, 1982: Sampling errors in the estimation of empirical orthogonal functions. *Monthly Weather Review*, **110,** 699-706.

Odekunle, T., 2004: Rainfall and the length of the growing season in Nigeria. *Int. J. Climatol.*, **24,** 467-479.

Odekunle, T., E. Balogun, and O. Ogunkoya, 2005: On the prediction of rainfall onset and retreat dates in Nigeria. *Theor. Appl. Climatol.*, **81,** 101-112.

Okoola, R. E., 1998: Spatial evolutions of the active convective patterns across the Equatorial Eastern Africa region during northern hemisphere spring season using Outgoing Longwave Radiation records. *Meteorology and Atmospheric Physics*, **66,** 51-63.

Okoola, R. E., 1999: Midtropospheric circulation patterns associated with extreme dry and wet episodes over equatorial eastern Africa during the northern hemisphere spring. *Journal of Applied Meteorology*, **38,** 1161-1169.

Owiti, Z., L. A. Ogallo, and J. Mutemi, 2008: Linkages between the Indian Ocean Dipole and east African seasonal rainfall anomalies. *Journal of Kenya Meteorological Society Volume*, **2,** 1.

Owiti, Z. O., 2005: Use of the Indian Ocean Dipole indices as a predictor of East African rainfall anomalies.

Paegle, J. N., L. A. Byerle, and K. C. Mo, 2000: Intraseasonal modulation of South American summer precipitation. *Monthly Weather Review*, **128,** 837-850.

Pai, D. S., J. Bhate, O. P. Sreejith, and H. R. Hatwar, 2011: Impact of MJO on the intraseasonal variation of summer monsoon rainfall over India. *Climate Dynamics*, **36,** 41-55.

Platts, P. J., P. A. Omeny, and R. Marchant, 2014: AFRICLIM: high-resolution climate projections for ecological applications in Africa. *Afr. J. Ecol.*

Pohl, B., and P. Camberlin, 2006a: Influence of the Madden-Julian Oscillation on East African rainfall. I: Intraseasonal variability and regional dependency. *Quarterly Journal of the Royal Meteorological Society*, **132,** 2521-2539.

——, 2006b: Influence of the Maddenâ€“Julian Oscillation on East African rainfall: II. Marchâ€“May season extremes and interannual variability. *Quarterly Journal of the Royal Meteorological Society*, **132,** 2541-2558.

——, 2006c: Influence of the Maddenâ€“Julian Oscillation on East African rainfall. I: Intraseasonal variability and regional dependency. *Quarterly Journal of the Royal Meteorological Society*, **132,** 2521-2539.

——, 2006d: Influence of the Madden-Julian Oscillation on East African rainfall: II. March-May season extremes and interannual variability. *Quarterly Journal of the Royal Meteorological Society*, **132,** 2541-2558.

Pohl, B., Y. Richard, and N. Fauchereau, 2007: Influence of the Madden-Julian oscillation on Southern African summer rainfall. *Journal of climate*, **20,** 4227-4242.

Rashid, H., H. Hendon, M. Wheeler, and O. Alves, 2011: Prediction of the Madden-Julian oscillation with the POAMA dynamical prediction system. *Climate Dynamics*, **36,** 649-661.

Reynolds, R. W., T. M. Smith, C. Liu, D. B. Chelton, K. S. Casey, and M. G. Schlax, 2007: Daily high-resolution-blended analyses for sea surface temperature. *Journal of climate*, **20,** 5473-5496.

Ridout, J. A., and M. K. Flatau, 2011: Kelvin wave time scale propagation features of the Madden-Julian Oscillation (MJO) as measured by the Chen-MJO index. *Journal of Geophysical Research: Atmospheres*, **116,** D18102.

Saji, N. H., B. N. Goswami, P. N. Vinayachandran, and T. Yamagata, 1999: A dipole mode in the tropical Indian Ocean. *Nature*, **401,** 360-363.

Schreck, C. J., L. Shi, J. P. Kossin, and J. J. Bates, 2013: Identifying the MJO, Equatorial Waves, and Their Impacts Using 32 Years of HIRS Upper-Tropospheric Water Vapor. *Journal of Climate*, **26**.

Segele, Z. T., and P. J. Lamb, 2005: Characterization and variability of Kiremt rainy season over Ethiopia. *Meteorology and Atmospheric Physics*, **89,** 153-180.

Segele, Z. T., P. J. Lamb, and L. M. Leslie, 2009: Large-scale atmospheric circulation and global sea surface temperature associations with Horn of Africa June-September rainfall. *International Journal of Climatology*, **29,** 1075-1100.

Seleshi, Y., and G. R. Demaree, 1995: Rainfall variability in the Ethiopian and Eritrean highlands and its links with the Southern Oscillation Index. *Journal of Biogeography***,** 945-952.

Seleshi, Y., and U. Zanke, 2004: Recent changes in rainfall and rainy days in Ethiopia. *International Journal of Climatology*, **24,** 973-983.

Semazzi, F. H. M., B. Burns, N.-H. Lin, and J.-K. Schemm, 1996: A GCM study of the teleconnections between the continental climate of Africa and global sea surface temperature anomalies. *Journal of climate*, **9,** 2480-2497.

Seo, K.-H., 2009: Statistical-dynamical prediction of the Madden–Julian oscillation using NCEP Climate Forecast System (CFS). *International Journal of Climatology*, **29,** 2146-2155.

Seo, K.-H., W. Wang, J. Gottschalck, Q. Zhang, J.-K. E. Schemm, W. R. Higgins, and A. Kumar, 2009: Evaluation of MJO Forecast Skill from Several Statistical and Dynamical Forecast Models. *Journal of Climate*, **22,** 2372-2388.

Shaman, J., and E. Tziperman, 2007: Summertime ENSOâ€“North Africanâ€“Asian Jet teleconnection and implications for the Indian monsoons. *Geophysical research letters*, **34**.

Simane, B., B. F. Zaitchik, and J. D. Foltz, 2014: Agroecosystem specific climate vulnerability analysis: application of the livelihood vulnerability index to a tropical highland region. *Mitig. adapt. strategies glob. chang.***,** 1-27.

Sobel, A., and D. Kim, 2012: The MJO-Kelvin wave transition. *Geophys. Res. Lett.*, **39**.

Spinage, C., 2012: The Changing Climate of Africa Part I: Introduction and Eastern Africa. *African Ecology*, Springer Berlin Heidelberg, 57-141.

Straub, K. H., 2013: MJO initiation in the real-time multivariate MJO index. *Journal of Climate*, **26,** 1130-1151.

Straub, K. H., and G. N. Kiladis, 2003: Interactions between the boreal summer intraseasonal oscillation and higher-frequency tropical wave activity. *Mon. Wea. Rev.*, **131,** 945-960.

Straub, K. H., G. N. Kiladis, and P. E. Ciesielski, 2006: The role of equatorial waves in the onset of the South China Sea summer monsoon and the demise of El Niño during 1998. *Dyn. Atmos. Oceans*, **42,** 216-238.

Suhas, E., and B. Goswami, 2010: Loss of Significance and Multidecadal Variability of the Madden–Julian Oscillation. *Journal of Climate*, **23**.

Sultan, B., and S. Janicot, 2003: The West African Monsoon Dynamics. Part II: The ‘‘Preonset’’ and ‘‘Onset’’ of the Summer Monsoon. *Journal of climate*, **16,** 3407-3427.

Sultan, B., C. Baron, M. Dingkuhn, B. Sarr, and S. Janicot, 2005: Agricultural impacts of large-scale variability of the West African monsoon. *Agricultural and forest meteorology*, **128,** 93-110.

Tadesse, T., 1994: Summer monsoon seasonal rainfall of Ethiopia in ENSO episodic years. *Proc. WMO/TOGA Int. Conf. on Monsoon Variability and Prediction, Trieste, Italy, Int. Centre for Theoretical Physics, World Meteor.* **,** 48–55.

Terray, P., P. Delecluse, S. Labattu, and L. Terray, 2003: Sea surface temperature associations with the late Indian summer monsoon. *Climate Dynamics*, **21,** 593-618.

Ummenhofer, C. C., A. Sen Gupta, M. H. England, and C. J. C. Reason, 2009: Contributions of Indian Ocean sea surface temperatures to enhanced East African rainfall. *Journal of Climate*, **22,** 993-1013.

Ventrice, M. J., C. D. Thorncroft, and P. E. Roundy, 2011: The Madden-Julian oscillation's influence on African easterly waves and downstream tropical cyclogenesis. *Monthly Weather Review*, **139,** 2704-2722.

Ventrice, M. J., M. C. Wheeler, H. H. Hendon, C. J. Schreck, C. D. Thorncroft, and G. N. Kiladis, 2013: A Modified Multivariate Madden-Julian Oscillation Index Using Velocity Potential. *Monthly Weather Review*, **141**.

Verdin, J., C. Funk, G. Senay, and R. Choularton, 2005: Climate science and famine early warning. *Philosophical Transactions of the Royal Society B: Biological Sciences*, **360,** 2155-2168.

Vigaud, N., Y. Richard, M. Rouault, and N. Fauchereau, 2009: Moisture transport between the South Atlantic Ocean and southern Africa: relationships with summer rainfall and associated dynamics. *Climate Dyn.*, **32,** 113-123.

Viste, E., and A. Sorteberg, 2011: Moisture transport into the Ethiopian highlands. *International Journal of Climatology*, **33,** 249-263.

Vitart, F. d. r., S. Woolnough, M. A. Balmaseda, and A. M. Tompkins, 2007: Monthly Forecast of the Madden-Julian Oscillation Using a Coupled GCM. *Monthly Weather Review*, **135,** 2700-2715.

Vizy, E. K., and K. H. Cook, 2003: Connections between the summer east African and Indian rainfall regimes. *Journal of Geophysical Research: Atmospheres*, **108,** 4510.

Waliser, D., and Coauthors, 2009: MJO simulation diagnostics. *Journal of Climate*, **22**.

Waliser, D. E., K. M. Lau, W. Stern, and C. Jones, 2003: Potential Predictability of the Madden-Julian Oscillation. *Bulletin of the American Meteorological Society*, **84,** 33-50.

Walker, G. T., 1910: Correlation in seasonal variations of weather, II. *Indian Meteor. Memoir***,** 1–21.

Walker, G. T., and E. W. Bliss, 1932: World weather. *V. Mem. Roy. Meteor. Soc.*, **4,** 53-84.

Wang, B., and H. Rui, 1990: Synoptic climatology of transient tropical intraseasonal convection anomalies: 1975-1985. *Meteorology and Atmospheric Physics*, **44,** 43-61.

Webster, P. J., V. O. Magaña, T. N. Palmer, J. Shukla, R. A. Tomas, M. Yanai, and T. Yasunari, 1998: Monsoons: Processes, predictability, and the prospects for prediction. *J. Geophys. Res.: Oceans*, **103,** 14451-14510.

Wheeler, M., and G. N. Kiladis, 1999: Convectively coupled equatorial waves: Analysis of clouds and temperature in the wavenumber-frequency domain. *Journal of the Atmospheric Sciences*, **56,** 374-399.

Wheeler, M., and J. McBride, 2005: *Australian-Indonesian monsoon.* Springer.

Wheeler, M. C., and H. H. Hendon, 2004: An all-season real-time multivariate MJO index: Development of an index for monitoring and prediction. *Monthly weather review*, **132,** 1917-1932.

Wheeler, M. C., H. H. Hendon, S. Cleland, H. Meinke, and A. Donald, 2009: Impacts of the Madden-Julian oscillation on Australian rainfall and circulation.

Williams, A. P., and C. Funk, 2011: A westward extension of the warm pool leads to a westward extension of the Walker circulation, drying eastern Africa. *Climate Dynamics*, **37,** 2417-2435.

Xue, Higgins, and Kousky, 2002: Influences of the Madden Julian Oscillations on temperature and precipitation in North America during ENSO-neutral and weak ENSO winters. Proc. Workshop on Prospects for Improved Forecasts of Weather and Short-Term Climate Variability on Subseasonal (2 Week to 2 Month) Time Scales, Mitchellville, MD, NASA Goddard Space Flight Center, 4 pp. .

Zhang, C., 2005: Madden-Julian Oscillation. *Reviews of Geophysics*, **43,** RG2003.

Zhang, L., B. Wang, and Q. Zeng, 2009: Impact of the Madden-Julian oscillation on summer rainfall in southeast China. *Journal of climate*, **22,** 201-216.

Zorita, E., and F. F. Tilya, 2002: Rainfall variability in Northern Tanzania in the March-May season (long rains) and its links to large-scale climate forcing. *Climate Research*, **20,** 31-40.

CURRICULUM VITAE

Fisseha Berhane

Education

Johns Hopkins University, Baltimore, MD
Ph.D. Candidate, Earth and Planetary Sciences, 2015
Thesis: Intraseasonal precipitation variability over tropical Africa
Advisor: Benjamin F. Zaitchik
M.A., Earth and Planetary Sciences May 2013
University of Connecticut
M.S., Natural Resources and the Environment, May 2011
Thesis: Model based assessment of potential impacts of climate change on the flow of the main headwaters of the Nile River: Equatorial Lakes Region and Blue Nile Basins
Advisor: Richard Anyah
Mekelle University, Ethiopia
B.Sc., Civil Engineering, June 2006

Research Positions

Graduate Research Assistant, Department of Earth and Planetary Science, Johns Hopkins University, Baltimore, Maryland. August 2011 – 2015
Graduate Research Assistant, Department of Natural Resources and the Environment, University of Connecticut, Storrs, CT 2009 – May 2011

Awards

Research Assistantship, Department of Earth and Planetary Sciences, Johns Hopkins University, Baltimore, Maryland 2012-2015
Morton K. Blaustein Fellowship, Department of Earth and Planetary Sciences, Johns Hopkins University, Baltimore, Maryland 2011-2012
Research Assistantship, Department of Natural of Resources and the Environment, University of Connecticut, Storrs, CT 2009-2011

Teaching Experience

Teaching assistant (TA), Department of Earth and Planetary Science, The Johns Hopkins University, Baltimore, Maryland. Spring 2013
Assistant Lecturer, Department of Civil Engineering, Mekelle University, Ethiopia 2006-2009

Peer-Reviewed publications

Berhane F and BF Zaitchik: An MJO-mediated mechanism to explain ENSO and IOD impacts on East African short rains. in prep.

Berhane F, BF Zaitchik and HS Badr, 2015: The Madden-Julian Oscillation's influence on Spring Precipitation over Equatorial West Africa. J. Climate. doi: http://dx.doi.org/10.1175/JCLI-D-14-00510.1.

Berhane F and BF Zaitchik, 2014: Modulation of Daily Precipitation over East Africa by the Madden–Julian Oscillation. J. Climate, 27(15): 6016-6034. doi: http://dx.doi.org/10.1175/JCLI-D-13-00693.1.

Berhane F, BF Zaitchik and A Dezfuli, 2013: Sub-seasonal analysis of precipitation variability in the Blue Nile River basin. J. Climate, 27(1): 325-344. doi: http://dx.doi.org/10.1175/JCLI-D-13-00094.1.

Selected Presentations

Berhane F and BF Zaitchik, 2015: The influence of the MJO on Spring Equatorial West African convection. 95th AMS Annual Meeting 2015, Sixth Conference on Weather, Climate, and the New Energy Economy, Phoenix, AZ.

Berhane F and BF Zaitchik, 2014: Intraseasonal variability of the impacts of the Madden-Julian Oscillation on East African long and short rains. 94th AMS Annual Meeting 2014, Second Symposium on Prediction of the Madden-Julian Oscillation: Impacts on Weather and Climate Extremes, Atlanta, GA.

Berhane F and BF Zaitchik, 2014: Intraseasonal variability of the impacts of the Madden-Julian Oscillation in the Gulf of Guinea. 94th AMS Annual Meeting 2014, Fifth Conference on Weather, Climate, and the New Energy Economy, Atlanta, GA.

Berhane F, BF Zaitchik and A Dezfuli, 2013: Evolution of intraseasonal precipitation variability in the Blue Nile River basin. 93rd AMS Annual Meeting 2013, 25th Conference on Climate Variability and Change, Austin, Texas, USA.

Berhane F, 2013: Modulation of daily rainfall over Africa by the Madden-Julian oscillation. 5th annual Atmosphere-Ocean Science Days seminar, Department of Earth and Planetary Sciences, Johns Hopkins University, Baltimore, Maryland

Berhane F, 2013: Intraseasonal variability of the modulation of daily rainfall over Africa by the Madden-Julian oscillation. Atmosphere-Ocean Seminar. Department of Earth and Planetary Sciences, Johns Hopkins University, Baltimore, Maryland

Berhane F, 2013: Modulation of daily rainfall over Africa by the Madden-Julian oscillation. Journal Club, Department of Earth and Planetary Sciences, Johns Hopkins University, Baltimore, Maryland

Berhane F, 2012: Intraseasonal variability of precipitation in the Blue Nile River Basin. Climate Dynamics of Tropical Africa: Present Understanding and Future Directions, Department of Earth and Planetary Sciences, Johns Hopkins University, Baltimore, Maryland, USA.

Berhane F, 2012: Rainfall anomalies in the Blue Nile basin and their teleconnections with the Indian Summer Monsoon. Journal Club, Department of Earth and Planetary Sciences, Johns Hopkins University, Baltimore, Maryland

Berhane F, 2012: Evolution of drivers and mechanisms of precipitation variability in the Blue Nile River Basin. Eastern Nile Technical Regional Office- Nile Basin Initiative. Addis Ababa, August 2012.

Berhane F, 2012: Model based assessment of potential impacts of climate change on the flow of the Blue Nile Basin. Eastern Nile Technical Regional Office- Nile Basin Initiative. Addis Ababa, August 2012.

Berhane F, Anyah R.O., 2010: Hydrological Response to Climate Change over the Blue Nile Basin Distributed hydrological modeling based on surrogate climate change scenarios. American Geophysical Union Fall Meeting 20140, San Francisco, California, USA.

Professional Memberships

Member of American Meteorological Society
Member of American Geophysical Union